Vibration Impact on Cycling Performance

Eloy Vázquez Fernández

Understanding power loss due to vibration and the parameters that influence it

Vibration Impact on Cycling Performance

by

Eloy Vázquez Fernández

to obtain the degree of Master of Science in Mechanical Engineering
at the Delft University of Technology,
to be defended publicly on Thursday July 17, 2025 at 13:30 (CEST).

Student number:	6083129	
Project duration:	December 2024 – July 2025	
Thesis committee:	Dr. J. K. Moore,	TU Delft, supervisor
	Dr. J. M. Papadopoulos,	External advisor
	Prof. Dr. Ir. R. Happee,	TU Delft
	Dr. G. Papaioannou,	TU Delft

An electronic version of this thesis is available at `http://repository.tudelft.nl/`.

TU Delft

Preface

It's already been almost two years since I moved to the Netherlands with the goal of pursuing this master's degree at the prestigious TU Delft. Coming here was a challenge I was willing to take, facing the language barrier, living abroad, and as they say, stepping out of my comfort zone. Well, let me tell you, that might have been true for the first few weeks, but not for long. And it's not because of some amazing adaptability of mine, but because of the incredible people who made this new place feel like home, while still having the huge support from back home. Without all of that, I definitely wouldn't be where I am today.

I want to thank all the friends I've met over these two years for the good times, the memories, the laughs, and the beautiful moments we shared. Lars, Zoe, Laura, Stef, and a long list of others I can't fully name here, but you know who you are. I don't know when I'll see you all again, but I'm sure this thesis won't be the last time.

During this last academic year, I started working at the Bicycle Lab at the university to complete my internship, and now my thesis, without knowing that this space would become so much more than just a research group. It became a safe and fun space where I could learn, feel supported and share many great moments that made this journey so much easier. The amazing people I met here were part of my daily motivation, along with the much needed coffees we shared. Special thanks to Anna, Simon, Neville, Bart, Benjamín and Jules for the time, help and laughs, both inside and outside the Bike Lab.

I also want to thank Jason. He was the first person I ever heard about from TU Delft and he helped motivate me to come here. Now, after a year of working with you, I can only thank you for your support and supervision throughout this whole project. Even though I was probably annoying with all my questions, meeting requests and doubts, you still managed to provide incredible help. It was also thanks to your encouragement that I reached out to the well known bicycle engineer Jim Papadopoulos. Thank you, Jim, for the generous support you provided during a big part of this project, and for the great brainstorming sessions, thoughts and knowledge you shared with me.

Of course, I also have to mention Fundación Barrié, who supported me during my second year of the master's through their fellowship program for the 2024–2025 academic year. Thank you to all the members for the trust you placed in me and for the opportunity you gave me.

And last, but most importantly, I want to thank my family and my girlfriend Raquel for their constant support from afar. Being so far from home but still feeling so loved and supported is, without a doubt, what has helped me achieve all the good things that are coming my way. Especially, I want to thank my parents for their never ending encouragement, for pushing me to reach my goals and pursue my dreams, even when it meant putting my interests above theirs. You always go above and beyond to help me and be there. You are truly unique. Por ello, gracias Papá y Mamá.

Eloy Vázquez Fernández
Delft, July 2025

Abstract

This project aims to provide insights and a better understanding of power losses in cycling, with a particular focus on professional road cycling and the vibration losses experienced during rough road stages such as Paris–Roubaix. While aerodynamic drag and pure rolling resistance are well-documented, vibrational losses, caused by the excitation of the bicycle-rider system over uneven roads, are often overlooked or inadequately modeled. This thesis investigates vibration-induced losses up to speeds of 30 km/h using a controlled coast-down experiment over a simulated cobblestone surface, isolating their contribution from aerodynamic and classical rolling resistance forces.

The results show that vibration losses can reach up to 350 W and account for as much as 60% of total power losses under certain conditions. A clear quadratic trend with respect to speed was identified, challenging the conventional assumption that such losses can be included in the speed-independent rolling resistance force term. Posture and tire pressure were also found to significantly influence these losses: riding out of the saddle consistently reduced vibration losses, while higher tire pressures led to greater total power loss due to increased vibrational dissipation. In contrast, rider behaviour, defined by varying levels of muscle contraction, did not yield consistent trends under the current experimental results.

To describe and better understand these dynamics, a simple empirical model was proposed, incorporating a quadratic dependence on speed, a linear dependence on pressure and a posture-dependent scaling factor. While intentionally limited in complexity, the model fits the observed data well and captures key interactions between the main influencing variables. These findings support the need to model vibration losses as a separate, speed-dependent component of total resistance. They also offer a useful starting point for future research focused on refining resistance models and enhancing energy efficiency in cycling.

Statement on Use of AI

During the preparation of this work, the author used ChatGPT-4o to support grammar correction, improve written expression and enhance the efficiency and clarity of data processing scripts. The tool was used strictly to improve the quality of code and analysis outputs, not to generate or interpret results. All content generated with its support was reviewed and edited by the author, who takes full responsibility for the final version of the text and content of the publication.

Contents

1 Introduction **1**
1.1 Energy balance in cycling . . . 1
1.2 Human power absorption . . . 3
1.3 Road as the source of vibrations and power loss . . . 5
1.3.1 Rolling mechanics . . . 5
1.3.2 Roughness and vibration source . . . 5

2 Methods **9**
2.1 Experimental plan . . . 9
2.1.1 Test set-up . . . 9
2.1.2 Conditions tested . . . 10
2.1.3 Modeling and generation of road excitations . . . 11
2.2 Bicycle instrumentation . . . 14
2.2.1 Inertial Measurement Units . . . 14
2.2.2 Power pedals . . . 15
2.2.3 Speed sensor . . . 15
2.3 Data processing . . . 15
2.4 Parameters and model fitting . . . 17
2.4.1 Speed and pressure relation . . . 17
2.4.2 Model proposal . . . 17

3 Results **19**
3.1 Reference tests . . . 19
3.2 Vibration losses per condition . . . 20
3.2.1 Comparison of rider conditions . . . 21
3.3 Vibration losses contribution to the general power losses . . . 23
3.3.1 Posture and behaviour influence . . . 23
3.3.2 Pressure effect . . . 23
3.3.3 Speed effect . . . 25
3.4 Fitting and model results . . . 25
3.4.1 Speed dependence . . . 25
3.4.2 Pressure dependence . . . 26
3.4.3 Model fit . . . 26

4 Discussion **29**
4.1 Aerodynamics and rolling resistance estimation . . . 30
4.2 Vibration losses results . . . 30
4.2.1 Behaviour effect . . . 30
4.2.2 Posture effect . . . 31
4.2.3 Tire pressure effect . . . 31
4.2.4 Speed effect . . . 31
4.3 Model fit . . . 32
4.3.1 Speed dependence . . . 32
4.3.2 Pressure dependence . . . 32
4.3.3 Vibration losses model proposed . . . 32
4.4 Limitations . . . 33
4.5 Future work . . . 34

5 Conclusion **35**

A IMU mounts - CAD Design **41**
A.1 Handlebar mount . . . 41
A.2 Seatpost mount . . . 43
A.3 Wheel mount . . . 45

B Bicycle Parameters **47**

C Road Characterization **49**
C.1 Photogrammetry: road scanning. . . . 49
C.2 Roughness index calculation . . . 51
C.2.1 Artificial Profile Design Based on Pseudo-BRI Matching . . . 52
C.3 Plank spacing configuration options . . . 54

D Road Database **55**
D.1 Cobbles Section . . . 55
D.2 Brick road . . . 56

E Preliminary Tests **59**
E.1 Resonance . . . 59
E.2 Transient . . . 61
E.2.1 Single shock . . . 62
E.2.2 Transient over repetitive disturbances. . . . 64

F Detailed results **67**
F.1 Reference session . . . 67
F.2 Vibration results . . . 70
F.2.1 Posture comparison . . . 80

G Additional Graphs **81**

1 Introduction

Professional sports are often defined by marginal gains. As a result, both industries and countries are investing heavily in the pursuit of higher performance in competitions and the development of technologies that enhance both performance and athlete safety. This work is broadly encompassed within the field of Sports Engineering.

Elite sports have been shown to increase participation in amateur and recreational versions of those sports [1, 2]. Increased participation can lead to better physical and mental health [1]. In the case of cycling, promoting the sport also indirectly promotes and encourage its use for commuting, reducing reliance on private vehicles, lowering pollution and traffic congestion, and contributing to healthier lifestyles and sustainable urban development [3, 4, 5]. This illustrates the relevance of investing in sports research and innovation not only to improve elite performance but also to generate a positive impact in society.

This thesis focuses on road cycling. In this discipline, competition results are determined by the fastest rider over the stage. To achieve this, professional racing teams and federations invest significant effort not only in training the rider but also in finding the fastest possible bicycle setup. This includes selecting the best possible configuration using sponsor-provided equipment, and in some cases, developing custom components based on technical expertise in the field. All of these efforts aim to improve the performance of the rider–bicycle system on the road, which can be described in terms of energy efficiency and more effective power use, ultimately leading to faster race times than the competitors [6].

The purpose of this thesis is to gain a better understanding of energy losses during cycling, with the goal of applying that knowledge to enhance performance.

1.1. Energy balance in cycling

Cyclists encounter various forces that contribute to energy losses, collectively referred to as 'tractive resistances' [7, 8]. These resistances are often classified in different ways, but are generally described in terms of aerodynamic drag, rolling resistance, frictional forces, braking forces, gravitational forces and inertial forces [9]. The contribution of each component depends on factors such as velocity, road slope, surface characteristics, and material properties, among others.

Energy losses in cycling are typically assessed in terms of power, as it directly represents the input required to overcome these resistances. Since power is a scalar quantity, it simplifies the evaluation by aggregating energy losses from all directions and body segments into a single, comprehensive value [10, 11, 12].

Understanding and minimizing these forces is a primary focus in bicycle-related technical literature [13]. Among these, the primary energy losses in cycling result from aerodynamic drag, gravitational forces and rolling resistance [13, 14]. While aerodynamics and gravitational forces are well-studied and documented [15, 16, 17], rolling resistance in human powered vehicles presents unique challenges. Unlike in automobiles, where most of the mass is concentrated in the vehicle itself, the cyclist's body mass significantly affects vertical loads and vibration-related energy losses. Despite its relevance, these losses are often overlooked, as rolling resistance is typically modeled as in Equation 1.1,

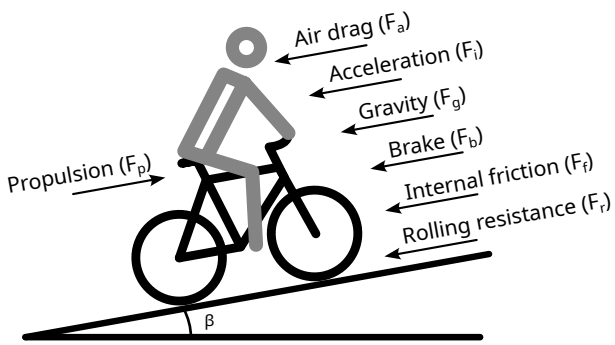

Figure 1.1: Forces acting on a moving bicycle as described by Fenre 2021 [9]

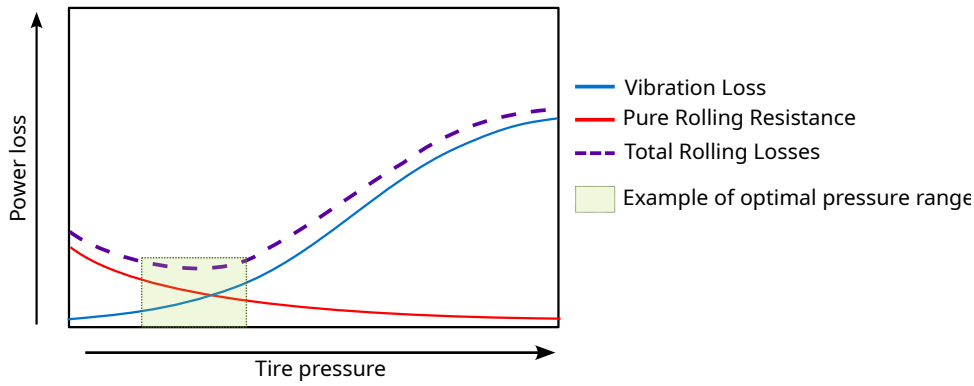

Figure 1.2: An hypothetical model suggested by SRAM Corporation on how vibration loss and tire rolling resistance combine to define an optimum tire pressure for a given surface roughness and tire characteristics. [21]

where the resistive force of the rolling resistance (F_r) is considered solely a function of normal force and a constant rolling resistance coefficient (C_{rr}):

$$F_r = m \cdot g \cdot C_{rr} \tag{1.1}$$

However, this classical approach often fails to capture energy losses caused by road-induced vibrations interacting with the cyclist's body and bicycle, due to an inaccurate or incomplete definition of C_{rr}. Rolling resistance is defined as the opposing force resulting from the interaction between the vehicle and the road surface [18]. This includes not only tire-related losses, such as hysteresis from tire deformation and frictional losses from the tire-road interaction, which are what typically is used to define and measure C_{rr}, but also what Wilson et al. [13] describe as 'bump resistance', referring to energy losses from vibrations that are primarily absorbed by the rider's body and also by the bicycle. These additional losses also contribute to the effective rolling resistance coefficient.

In the automotive industry, research on vibrations generated by rolling over road surfaces primarily focuses on passenger comfort and health risks. In cycling, vibrations are frequently reported as one of the main sources of riding discomfort [19]. However, their impact on energy efficiency has largely been overlooked [10, 20].

This thesis aims to address that gap by investigating vibration-induced energy losses and their implications for cycling propulsion efficiency. Within the context of rolling resistance, a distinction is made between pure rolling resistance, defined as losses resulting from tire properties and the interaction with the road, and total rolling losses, which also include additional energy losses caused by road-induced vibrations to the bicycle and rider. These additional losses are here referred to as vibration losses.

Regarding the interaction between vibration losses and pure rolling losses, SRAM Corporation [21] proposes a hypothesis, shown in Figure 1.2, that suggests a 'sweet spot' in which a specific tire pressure minimizes total rolling losses. While pure rolling resistance has been well-studied and much of the

automotive literature is applicable to bicycles, vibration losses have received no theoretical attention and require further exploration [22].

Existing studies often examine material properties or vibration responses of bicycle frames without a rider [23], but there is limited research focused on the transmission of road-induced vibrations to the cyclist [24].

For high performance in elite cycling, where small improvements can significantly affect race outcomes, vibration-induced energy losses not only impact performance but also have implications for health, fatigue and injury risk derived from the transmitted vibrations and therefore require attention [10, 25].

The objective of this study is to develop a method to quantify vibration losses and demonstrate their impact on cycling performance under different conditions. To make the results widely understandable and to support future studies, the findings will be presented in a graphical format, allowing vibration losses to be estimated based on parameters such as travel speed, tire pressure or rider posture.

1.2. Human power absorption

In the context of energy losses due to road-induced vibrations in cycling, the human rider plays a dominant role over the bicycle. As the rider's body constitutes the majority of the system's mass, it significantly influences the dynamic response to vibrations. Consequently, power absorption by the human body becomes the main contributor to energy loss. For this reason, additional attention is dedicated to analyzing the human component of power absorption.

The study of body vibrations in humans has a long history, with foundational research dating back to the 1960s by authors such as Lee, Pradko and Suggs [26, 27, 28]. These investigations often analyze the biodynamic response of the human body, which describes how the body interacts with and reacts to externally applied vibrations. In the case of this thesis, vibrations are transmitted through the bicycle into the rider's body and propagated throughout its structure. Due to the body's elastic nature, these vibrations lead to distortions and deformations that generate internal reaction forces as the body attempts to restore its original shape and position [27]. This transmitted motion is influenced by the inertia, damping and elasticity of muscle tissues and the skeletal structure [26]. As a result, the transmission of vibrations to different anatomical parts and internal organs depends not only on the external input but also on the mechanical properties of the tissues [26]. These properties vary with time, posture and between individuals, making the biodynamic response highly complex [29].

The overall behavior of the human body can be represented using mechanical analogs, typically represented by lumped-parameter models that use masses, springs and dampers to capture the system's dynamic characteristics [29]. Mechanical systems dissipate power due to non-conservative forces, primarily through damping, which reduces vibrational energy over time.

To illustrate this, consider a single impulse excitation applied to the human body. This energy induces deformation in the elastic structure of the body, leading to a temporary change in shape. In response, internal restoring forces act to return the body to its original state. The applied energy is then divided into two components:

- Stored elastic energy, which sustains the oscillatory motion.
- Dissipated energy, which is lost due to internal damping.

Vibrations continue until all the initial energy is dissipated through internal damping. The rate of this dissipation over time is what is defined as 'absorbed power' [27].

Many parameters influence absorbed power and the biodynamic response. Starting with the characteristics of the input excitation, the two primary factors are frequency and magnitude. Frequency is defined as the number of oscillatory cycles completed per unit of time. Its influence is significant because the human body and its parts behave as mass-spring-damper systems with inherent resonance characteristics. When excited at specific frequencies, these systems exhibit resonance phenomena [30]. As a result, absorbed power peaks at around 5 Hz, which aligns with the body's natural resonance frequency [12, 31, 32].

Regarding magnitude, absorbed power has been shown to increase approximately in proportion to the square of the vibration acceleration [32, 33]. This means that if a rider experiences double the acceleration, the associated energy loss would be roughly four times greater, highlighting the importance

of understanding and mitigating vibration effects. These characteristics are inherent to the road, which acts as the main source of vibrations and are influenced by the travel speed on the surface.

Focusing now on human-related parameters, several studies have identified factors that influence the biodynamic response. Some of these can be deliberately controlled, such as muscle contraction level or the rider's adaptability to vibration input. Others, such as physiological factors like body dimensions, fat-to-muscle ratio, or body weight, cannot be adjusted through pre-race setup or altered during the race.

Posture is one of the most significant factors affecting the biodynamic response. Parameters such as seat height, footrest position, hand placement, seat dimensions and seat inclination are commonly studied to assess their impact [34]. Posture also determines how the rider's body mass is distributed across the five contact points with the bicycle: both foot-pegs, the hands on the handlebar and the seat. This weight distribution influences how vibrations are transmitted and how much power is absorbed. Greater total body weight has been associated with increased absorbed power [12], which can be explained mechanically, as moving a greater mass requires more energy.

Another relevant factor is muscle activation, which is closely related to posture. Unlike posture, which involves structural configuration, muscle activation refers to the tension and stiffness of the muscles. A relaxed posture, for example, involves less abdominal muscles contraction, resulting in lower body stiffness and increased damping [12].

Power is defined as the product of force and velocity at the point of application, expressed as $P(t) = F(t) \cdot v(t)$. Since both force and velocity are vector quantities, power is inherently directional, resulting in a complex power value. The real component represents dissipated energy, while the imaginary component corresponds to cyclically stored and released elastic energy [32]. Over time, the elastic component averages out to zero, while the dissipated energy accumulates, defining the total absorbed power, typically measured in watts (W). The physical formulation is given in Equation 1.2.

$$P_{abs} = \frac{1}{T}\int_0^T F(t) \cdot v(t)dt \tag{1.2}$$

To determine the power dissipated in the human body, the contributing quantities in Equation 1.2, force (F) and velocity (v), must be measured at the interfaces where power loss occurs.

By measuring this on seated subjects, Pradko [27] established the foundation for the absorbed power method and developed iso-power curves as functions of vibration magnitude and frequency. His experiments reported values of up to 920 W of power dissipation in the human body, highlighting the potential magnitude of these losses.

Specific case in bicycles

In the field of cycling, some studies have measured the absorbed power by the human body due to vibrations while riding. To achieve this, bicycles were instrumented with custom setups. First, force transducers were used to measure the interaction forces at the rider–bicycle contact points. Most commonly, only the seat–buttocks and handlebar–hands interfaces are considered, as the pedals contribute less to vibration-related power loss in a seated posture. Additionally, measuring forces at the pedals is complicated by the challenge of isolating vibration-induced forces from those generated by pedaling [30]. Second, the velocity at which these forces are applied must also be recorded. For this, accelerometers are mounted at the contact points and the measurements are integrated to obtain velocity data. Lépine [35, 36], Pelland-Leblanc [37, 38] and Vanwalleghem [39, 30] have developed such custom instrumentation setups to study the relationship between absorbed power, rider comfort and safety.

Using this method, Vanwalleghem [30] recorded 43.9 W of power absorbed by the human body during real road test on cobblestones, already a notable value that underscores the significance of vibration-related losses. According to Pelland-Leblanc [37], this method is robust and remains relatively unaffected by minor changes in rider position, making it suitable for a variety of cycling conditions. However, this approach only captures the power absorbed by the human body at the contact points and not the total system losses. For instance, energy may also be absorbed by the tires as they deform over surface irregularities, by the frame as it filters accelerations, or through relative motion between different parts of the rider's body and the bicycle, as in the saddle. These contributions are not accounted for in interface-based measurements. A more complete assessment of vibration losses is therefore necessary to estimate their full impact.

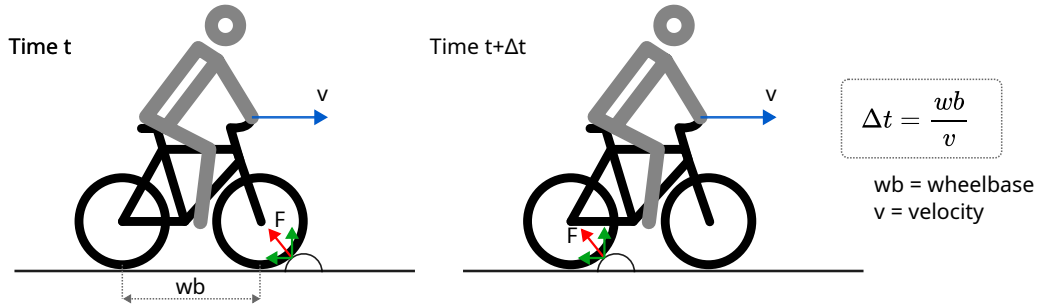

Figure 1.3: Time shift experienced in the bicycle when encountering a bump.

Attempts to address this gap have been made, though not always with sufficient detail regarding experimental conditions or procedures and in some cases, the findings have not been peer-reviewed. For example, Heine [40] reported power differences of up to 290 W when riding at 25 km/h over rumble strips, highlighting the potential magnitude of vibration-related losses in real-world scenarios. However, key information such as the dimensions and spacing of the rumble strips, the roughness of the surface, or the rider's weight or posture is not provided. Consequently, the findings may require cautious interpretation. Notably, the publication reports statistically significant differences across all tested conditions. However, some of the presented values, such as those comparing different pressures, appear identical in the graphs. This inconsistency suggests the possibility of typographical errors or highlights the need for greater clarity, which may affect the perceived reliability of the conclusions.

1.3. Road as the source of vibrations and power loss

1.3.1. Rolling mechanics

It is well known that bumps encountered on the road while cycling result in a noticeable loss of forward speed [13]. This occurs due to several factors, including the need for the bicycle to ascend and follow the road profile rather than maintaining a purely horizontal trajectory. As a result, part of the rider's energy is diverted, not only toward forward propulsion but also toward generating vertical motion and vibrations induced by the uneven terrain.

If the bicycle-rider system is simplified as a mass supported by a spring and damper, then a non-smooth surface causes the spring to compress and extend, following the road profile due to the contact point model. This leads to vertical accelerations and the damper in this analogy dissipates energy, perceived by the rider as resistance to motion [22]. However, this basic model does not fully capture the complexity of the real system, where the bicycle and rider move somewhat independently. The human body, with its many joints and muscles, responds in a much more complex manner and the road profile is not perfectly tracked.

As previously mentioned, when encountering a bump, the bicycle not only moves vertically but also loses horizontal velocity. This indicates that when cycling over uneven surfaces, the bicycle experiences excitation in both the vertical and horizontal directions [30]. Furthermore, during straight-line riding, the excitation experienced by the front wheel is mirrored by the rear wheel after a time delay. Figure 1.3 illustrates this time shift, along with the reaction forces generated as the bicycle moves over a bump.

The rolling mechanics of a bicycle over a surface profile are also influenced by the fact that the wheel acts as a filter. Wheels naturally help smooth out road irregularities, reducing the displacement transmitted by medium-wavelength surface features. As shown in Figure 1.4, the rolling action of the wheel, due to its finite radius, modifies how vertical displacements from the terrain are read and transmitted to the rider, acting as a low-pass filter.

1.3.2. Roughness and vibration source

The road surface is the primary source of vibration and thus a critical factor in determining power losses related to it. Irregularities in the road profile act as a continuous series of bumps, generating both the amplitude and frequency of the vibration input based on the traveling speed and the profile's wavelength spectrum.

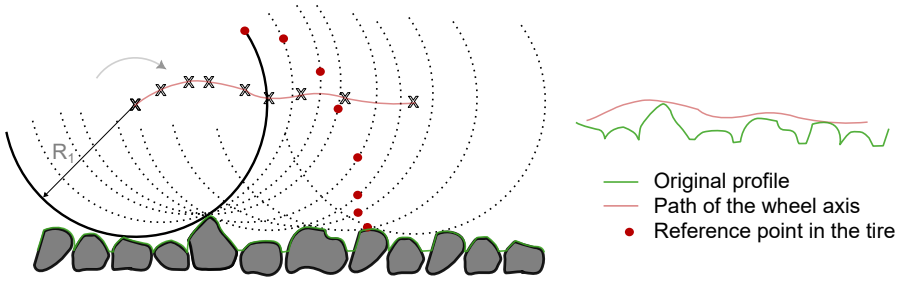

Figure 1.4: Filtering effect of the wheel on the profile input into the system.

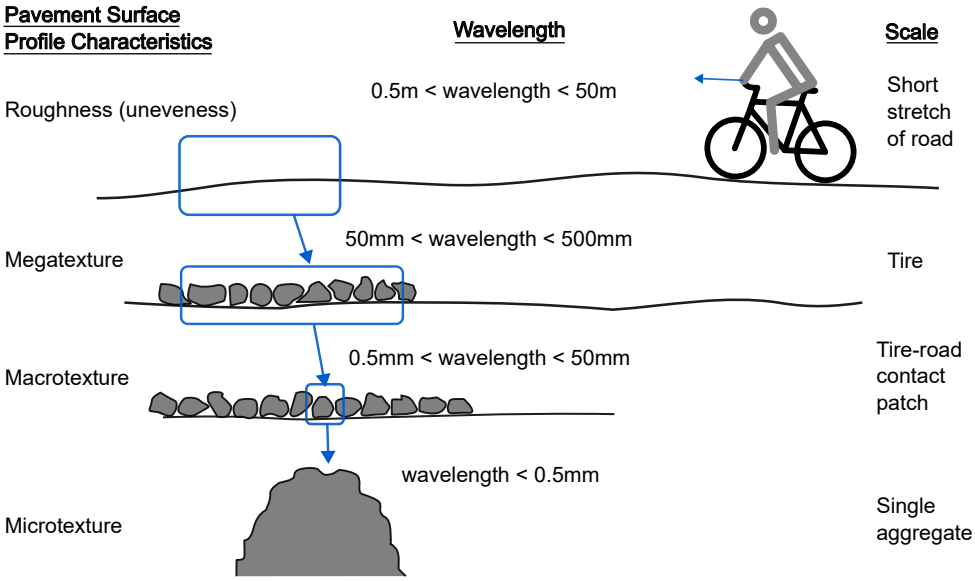

Figure 1.5: Road texture and wavelength as defined by Thigpen 2015 [41]

This frequency content arises from the layered complexity of real-world surfaces. As illustrated in Figure 1.5, road features can be classified into four main scale levels: roughness, megatexture, macrotexture and microtexture. The interplay between the wavelength and height of these surface features creates the full vibration spectrum experienced by the rider as the bicycle moves over the terrain. Each road has a unique profile defined by its combination of features and to describe it accurately, one would need to compute its frequency spectrum, including amplitude and phase. This analysis reveals the composition of the road in terms of wavelength, or frequency, when traveling speed is considered (frequency = wavelength · speed). However, in practice, a Power Spectral Density (PSD), which accounts only for the amplitude at every frequency, is commonly used to describe road profiles in terms of roughness [42], an example can be seen in Figure 1.6 taken from Evans [43]. This means that to replicate the roughness of a specific road and thus generate similar excitations on a bicycle, one must at least match the PSD. This would require recreating a profile that includes an infinite combination of frequencies, an impractical task. Therefore, an alternative method was used in this project to reproduce the road of interest.

To simplify the management and analysis of large-scale road data, the International Roughness Index (IRI) was introduced in 1986 by the World Bank. It allows roads to be classified based on surface roughness [44, 42]. As defined in Equation 1.3, the IRI is the accumulated relative motion between the sprung mass (z_s) and unsprung mass (z_u) of the quarter-car model shown in Figure 1.7, normalized by the travel distance L. This index is typically expressed in units of slope (e.g., m/km) [44].

It is important to acknowledge the limitations of the IRI, or any roughness index defined in a similar manner, in fully characterizing road roughness. As illustrated in Figure 1.6, different longitudinal profiles can yield the same IRI value while exhibiting distinctly different power spectral densities (PSDs). This demonstrates that while an index like IRI can indicate how rough a surface is, the PSD reveals

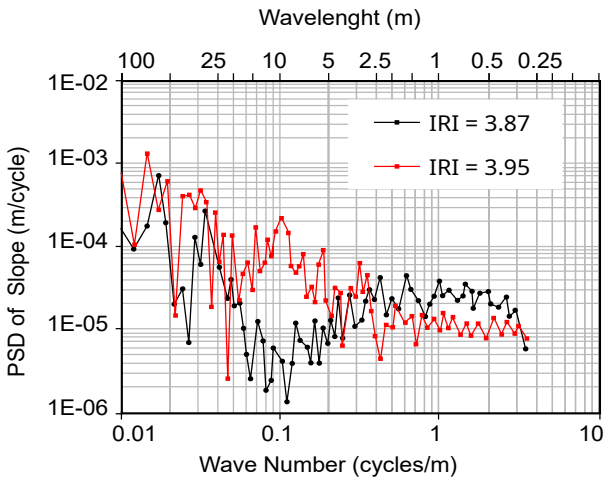

Figure 1.6: Comparison of two different road profiles (red and black) based on their Power Spectral Density (PSD), despite having the same International Roughness Index (IRI). Adapted from [43].

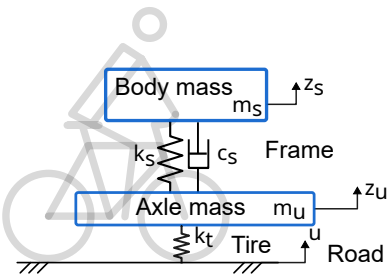

Figure 1.7: Quarter car model, applied to the bicycle as described by Tomiyama 2024 [45]. Body mass includes the cyclist.

why and how that roughness manifests across different spatial frequencies. In other words, roads with identical IRI values may produce significantly different vibration responses due to their underlying spectral characteristics.

$$IRI = \frac{1}{L}\int_0^T \mid (\dot{z}_s - \dot{z}_u) \mid dt \tag{1.3}$$

Moreover, the IRI is based on a quarter-car model representing a passenger car traveling at 80 km/h, which makes it less suitable for assessing road roughness in a cycling context. Additionally, with its defined parameters, the IRI is mainly sensitive to roughness-level wavelengths as shown in Figure 1.5. To address these limitations, Tomiyama [45] proposed the Bicycle Roughness Index (BRI), a custom metric based on a quarter-car model tailored to bicycles, but defined using the same formulation as in Equation 1.3. The BRI model incorporates different parameters for mass, spring and damping, and simulates motion at 15 km/h, a common cycling speed. These parameter adjustments make the model sensitive to smaller wavelengths, particularly those in the ‘megatexture’ range, which have shown to be most relevant for human-powered vehicles (HPVs) [45].

With this bicycle-specific roughness index (BRI), the road of interest can be characterized and an artificial profile can be generated to match this value. In this way, the system’s amplitude response can be realistically reproduced, enabling simplified but meaningful replication of real-road conditions.

To quantify and better understand these often overlooked vibration losses, this project investigates them using a controlled coast-down test over a simulated cobblestone surface. The artificial profile was designed to reproduce the Bicycle Roughness Index (BRI) of a selected section across the full range of tested speeds. Vibrational losses were studied across key variables known to influence ride dynamics: rider posture, rider behaviour (defined as the level of muscular tension) and bicycle tire pressure. Each of these conditions was tested at multiple speeds ranging from 10 to 30 km/h. Power loss was computed from the change in kinetic energy over a fixed stretch, while aerodynamic and classical

rolling resistance losses were estimated from dedicated reference experiments. The results provide a detailed characterization of vibration-induced losses and their dependence on rider and bicycle parameters, with the goal of improving future modeling approaches and performance optimization in cycling. Based on these findings, a curve-fitting analysis was conducted to evaluate whether the relationship between vibration losses and speed or pressure is better represented by a linear or quadratic function. This led to the proposal of a simplified model which, while preliminary, may offer a useful first approximation for describing vibration-induced power losses.

2

Methods

2.1. Experimental plan

During cycling, various forces act on the system, such as aerodynamic drag, rolling resistance and gravitational forces related to slope, each contributing to power losses. These forces represent the major components of energy expenditure in cycling. To accurately study the effect of a specific loss mechanism, such as vibration-induced power loss, it is desirable to conduct experiments in a controlled environment. This helps mitigate confounding factors such as wind direction and speed, road evenness and surface homogeneity, and secondary environmental conditions like temperature.

2.1.1. Test set-up

The experimental procedure for assessing vibration power losses due to road roughness is based on the well-established coast-down method [46, 18, 47].

The test involves measuring vehicle speed evolution to deduct the resistive forces acting on the system. To perform a trial, the rider approaches the test section and enters it at a predetermined target speed. Upon crossing the first checkpoint, the rider must cease pedaling, allowing the bicycle to coast freely along the straight, controlled path until reaching the end checkpoint, where braking or maneuvering may resume.

The start and end of the test section are marked by thin slats placed on the ground. As the bicycle rolls over them, they generate distinct vibrations detectable by the onboard accelerometers, allowing precise segmentation of each trial during post-processing. Within the test stretch, five wooden planks are placed at specific spacings determined by the target speed of the test. These planks and spacings are designed to replicate the dynamic response caused by road-induced excitations, as further described in Section 2.1.3. The number of bumps was selected to ensure that the speed loss across the stretch remains small, minimizing bias when calculating the average power loss relative to the average speed across the stretch. The validity of using five planks, ensuring that transient effects do not influence the measurements, is supported by preliminary tests, detailed in Appendix E.

A buffer zone of three meters is included before the first and after the last bump. This distance is sufficient for the system to settle and for vibrations to dissipate before exiting or encountering the next obstacle, this was confirmed through preliminary testing, see Appendix E. As a backup, video recordings from two phones were used to track the rider's entry and exit speeds, with ground markers placed one meter after the start and before the end of the test section. These recordings provide a visual reference in case of data loss from the velocity sensor. A schematic of the full experimental setup is shown in Figure 2.1.

Using the coast-down method, the effect of road unevenness on rolling resistance can be evaluated over a sufficiently long stretch [18]. This enables the estimation of energy losses due to vibration-induced excitation of the bicycle–rider system. The experiments are carried out indoors to eliminate disturbances from wind and slope variations, thus increasing the accuracy of the measurement [47].

To determine the tractive resistances for the various test conditions, energy loss is assessed by calculating the difference in kinetic energy at the beginning and end of the controlled stretch. Since the rider contributes no additional power during coasting, this energy difference directly reflects the

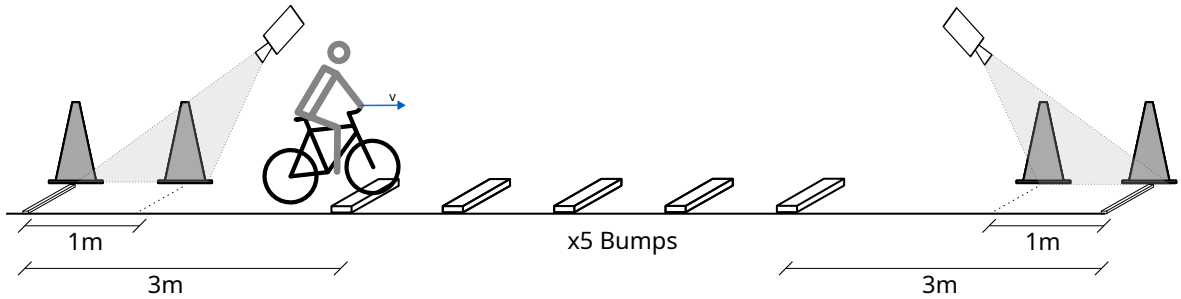

Figure 2.1: Experimental set-up.

mechanical energy losses. Given that the stretch is flat, the potential energy remains constant and any change in kinetic energy corresponds entirely to system dissipation.

The kinetic energy is computed using the velocity measured by the IMU on the rear wheel. The velocity at the entry and exit of the stretch is used in Equation 2.1, where m is the combined mass of the rider (100kg) and the bicycle (8.05kg), and v is the velocity in meters per second:

$$K = \frac{1}{2} \cdot m \cdot v^2 \tag{2.1}$$

Dividing the energy loss, calculated as the difference in kinetic energy over the stretch, by the time taken to traverse it yields the average power dissipated, which is then associated with the trial's average speed. This method captures the total power loss due to all resistive forces acting during the coast-down, which, under the test conditions (no slope and no pedaling input), are limited to aerodynamic drag (P_{aero}) and rolling resistance (P_{rr}). The objective of this study is to isolate the portion of rolling resistance specifically attributable to vibration-induced losses. To do so, the classical rolling resistance component, modeled using the coefficient C_{rr}, is separated from an additional term, VL, representing the vibration losses. This decomposition is expressed in Equation 2.2, which is derived from Newton's second law for longitudinal motion.

$$P_{loss} = P_{aero} + P_{rr} = \frac{1}{2}\rho C_d A v^3 + mgC_{rr}v + VL \tag{2.2}$$

To isolate the vibration losses (VL), a reference experiment was conducted using the same procedure but without obstacles. This simple coast-down trial over 25 meters provided baseline data for estimating the aerodynamic and rolling losses. Using these results, the drag area C_dA and rolling resistance coefficient C_{rr} were fitted.

The coefficients were tailored to each experimental condition. The rider's posture affects the drag area (C_dA), while tire pressure affects the contact patch between the tire and the road, influencing the rolling resistance coefficient (C_{rr}). Both coefficients are assumed independent of speed in the tested range, which is consistent with previous literature [46, 47]. Once fitted, the aerodynamic drag and rolling resistance coefficients allowed classical resistance components to be subtracted from the total measured losses, isolating the vibration-related power losses as Equation 2.3 shows. It is important to note that vibration losses are not directly measured; instead, they are estimated as the residual power loss after accounting for the fitted aerodynamic and rolling resistance components, P_{aero} and P_{PureRR} respectively, from the total power loss measured P_{total}. In this way, what is technically obtained are the incremental losses attributed to the artificial road-induced vibrations, introduced by the simulated cobblestone profile.

$$VL = P_{total} - P_{aero} - P_{PureRR} \tag{2.3}$$

2.1.2. Conditions tested

As outlined in the introduction, vibration losses are influenced by multiple parameters. This study focuses on a subset of those, described below, to assess their effects on vibration-related power loss. Each parameter was tested across a range of speeds from 10 to 30 km/h, with 5 km/h increments, and a crossed experimental design was implemented to evaluate both individual and interaction effects between certain conditions:

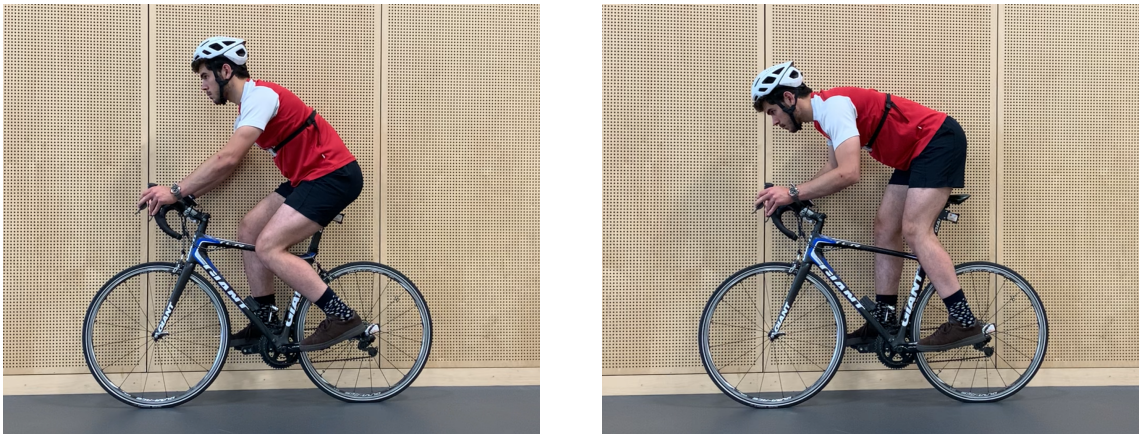

(a) Seated (b) Off the saddle

Figure 2.2: Riding postures tested.

- **Tire pressure**
  Tire pressure is one of the most accessible adjustable parameters that influences the passive dynamics of the bicycle, particularly the spring-damper characteristics of the wheel–tire system. This experiment investigates the extent to which lower pressures reduce vibration transmission and thereby decrease power losses on rough surfaces. Pressures ranging from 3.5 to 5.5 bar were tested in 0.5 bar increments, applied equally to both tires. Values were chosen within the tire manufacturer's safe operating range and to avoid rim impacts from excessive deformation.

- **Rider posture**
  The posture adopted by the cyclist can significantly influence vibration losses. During racing, riders often switch to an 'out of the saddle' or 'off the saddle' posture during climbs or sprints. This affects both the aerodynamics and the distribution of mass across the contact points. In this posture, only the hands and feet remain in contact with the bicycle, changing the load and affecting the biodynamic response. Two postures were evaluated: 'Seated' and 'Off the saddle', as shown in Figure 2.2.

- **Rider behaviour (muscle contraction)**
  Muscle activation is another factor influencing biodynamic response that can be modified by the rider. To investigate its role, the rider adopted three distinct behaviours during the tests:

  - **Normal behaviour (NB)**: natural, unmodified riding behaviour.
  - **Relaxed behaviour (RB)**: intentionally loosening muscles and reducing grip, allowing more freedom for the bicycle to respond to road vibrations.
  - **Stiff behaviour (SB)**: deliberate maximal co-contraction of muscles to simulate a rigid body position.

  These behaviours were tested only in the seated posture to evaluate the influence of rider stiffness on vibration transmission and absorbed power.

This broad combination of conditions allows a detailed analysis of how vibration losses vary with mechanical settings and rider dynamics. To ensure consistency, all experiments were conducted in the same indoor venue, with the rider wearing the same clothing across sessions to preserve aerodynamic and rolling resistance parameters as fitted in the reference tests.

2.1.3. Modeling and generation of road excitations

To study vibration losses caused by road-induced excitations in a controlled environment, the primary challenge is to realistically replicate the excitations experienced by the bicycle–rider system on real roads. As discussed in the introduction, the most accurate way to recreate these conditions would be

m_s (kg)	m_u (kg)	k_s (kN/m)	k_t (kN/m)	c_s (Ns/m)
27	17	194	123.2	233

Table 2.1: Quarter-car model parameters for the Bicycle Roughness Index computation.

to replicate the actual road surface or, at minimum, a surface with the same Power Spectrum Density (PSD). However, due to the complexity of replicating a full PSD, this project instead uses surfaces that match the roughness index of real roads. Specifically, the Bicycle Roughness Index (BRI), as described by Tomiyama [45], is used.

Mathematical model description

The BRI is computed from a longitudinal road profile using a quarter-car model, defined by the parameters listed in Table 2.1 and illustrated in Figure 1.7. The model's output y, representing the relative distance between the sprung and unsprung mass, is accumulated over the length of the profile and normalized by that length, resulting in a roughness index expressed in units of slope, similarly what shown in Equation 1.3. This response is derived from the state-space formulation of the model, described as follows:

$$\dot{x}(t) = Ax(t) + Bu(t) \tag{2.4}$$

$$y(t) = Cx(t) \tag{2.5}$$

Where the x represents the state vector ($[z_s, \dot{z}_s, z_u, \dot{z}_u]^T$) and u the vertical input coming from the road, i.e. the road height profile, all depicted in Figure 1.7. The dot over the character represents the time derivative and the T the transposed matrix. Time t is related with the longitudinal distance L by the forward simulated speed v. The matrices A, B, C called as the dynamic, control and sensor matrices are defined as follows:

$$A = \begin{bmatrix} 0 & 1 & 0 & 0 \\ -\frac{k_s}{m_s} & -\frac{c_s}{m_s} & \frac{k_s}{m_s} & \frac{c_s}{m_s} \\ 0 & 0 & 0 & 1 \\ \frac{k_s}{m_u} & \frac{c_s}{m_u} & -\frac{k_s+k_t}{m_u} & -\frac{c_s}{m_u} \end{bmatrix} \tag{2.6}$$

$$B = \left[0, 0, 0, k_t/m_u\right]^T \tag{2.7}$$

$$C = \left[1, 0, -1, 0\right] \tag{2.8}$$

This model is evaluated for a given road surface, which acts as a input to the system ($u(t)$). This input is dependent not only on the road surface, but the speed at which the model is interacting with the longitudinal profile considered. For the Bicycle Roughness Index, the computing speed is 15 km/h.

Since the Bicycle Roughness Index (BRI) is a recent development, there is currently no available database of surface values. To address this, a simple, accessible, and sufficiently accurate method was developed to characterize various surfaces and estimate their BRI values. This was accomplished using photogrammetry to capture and reconstruct 3D surface profiles. A series of photographs were taken following a specific pattern and processed through photogrammetry software to generate a detailed mesh of the road surface. The resulting mesh was then scaled, filtered, and repaired to ensure maximum accuracy possible. Once processed, the mesh was exported as a point cloud and input into a Python script that generated multiple longitudinal cross-sections. These sections served as road input profiles for the quarter-car model used to compute the BRI. To account for variability, the roughness index was computed across multiple approach angles and the average value was taken as the representative BRI for each surface. A more detailed explanation of this process is provided in Appendix C. Using this methodology, a selection of representative road surfaces was characterized, resulting in a small database of road types and their associated BRI values. This helps contextualize the BRI in relation to perceived road roughness. The surfaces and their corresponding BRI values are presented in Appendix D.

For this project, the roughest surface in the database, a cobblestone section, was selected to investigate the potential impact of vibration losses. This surface has a BRI value of 257.1, indicating a high

(a) Real road.

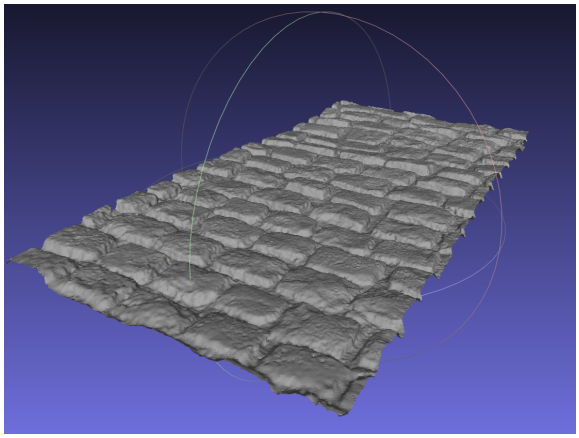

(b) 3D scanned surface.

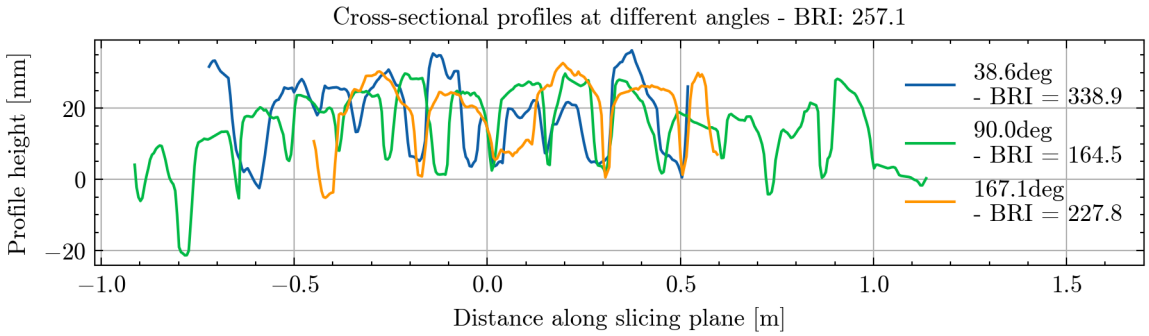

(c) Sample of cross-sectional cuts.

Figure 2.3: Section of road used to simulate on the experiments.

level of roughness compared to the other characterized surfaces. Figure 2.3 provides a visual representation of the cobblestones, along with the 3D-scanned surface and three example cross-sectional cuts used for analysis. Further details on this surface and its characterization are provided in Appendix D.1.

Recognizing the limitations of roughness indices, expressed during the introduction, the test surface was constructed based on this scanned surface by using an artificial profile made of evenly spaced wooden planks to produce controlled excitations. This single-frequency input profile was chosen for its simplicity, but special attention was given to account for the fact that such a profile only excites a single frequency, determined by the travel speed divided by the spacing between planks. To improve the fidelity of the simulated excitation, the BRI was recalculated at the target testing speeds instead of using the default 15 km/h, resulting in a 'Pseudo-BRI'. This adjustment ensures that the dominant excitation frequency of the artificial profile aligns more closely with the speed-specific dynamics of the rider–bicycle system. Consequently, the vibration response more accurately reflects the vertical displacements experienced by the rider at each test speed, enhancing the realism of the simulation.

Artificial profile design

To generate the vibrations required for the tests, only rectangular wooden planks were used to construct the artificial surface. The dimensions and arrangement of these planks along the bicycle path were designed to replicate the excitation characteristics of the real road surface. The resulting response of the quarter–car model to this artificial profile was compared against the pseudo-BRI response of the scanned cobblestone surface at each test speed. Plank dimensions were fixed at 90 mm in width and 20 mm in height and the spacing between them was optimized to best match the dynamic response of the reference surface.

A range of spacing configurations were simulated, and those producing pseudo-BRI values closest to that of the real cobblestone section were selected. Additional constraints were applied to avoid spacings that aligned with the bicycle's wheelbase of 0.99 m or generated excitation frequencies near the 5 Hz resonance of the human body [12, 31, 32]. Appendix C.3 presents the different spacing

Speed (km/h)	Road Pseudo-BRI	Artificial Pseudo-BRI	Spacing (m)	Excitation frequency (Hz)
10	341.6	341.7	0.73	3.81
15	257.1	255.5	1.69	2.46
20	196.6	203.1	0.73	7.61
25	117.4	115.8	0.62	11.20
30	125.6	126.5	0.69	12.08

Table 2.2: Spacing needed for the selected plank dimensions to match the selected road Pseudo-BRI, defined with the BRI model but computed at a specific speed rather than the standard 15 km/h.

configurations considered to match the target Pseudo-BRI values. The final artificial road configurations selected for testing are summarized in Table 2.2.

2.2. Bicycle instrumentation

To study vibrations and the associated power losses on the bicycle in response to ground excitations, the test bicycle was instrumented with sensors to record relevant data. The bicycle used for this project was a 2012 Giant TCR Advanced (Giant Manufacturing Co. Ltd., Taichung, Taiwan), with a carbon fiber frame. It was fitted with Shimano Dura-Ace C24 622×15C aluminum rims (Shimano Inc., Osaka, Japan) and Vittoria Randonneur 700×28C tires (Vittoria S.p.A., Brembate, Italy). Multiple sensors and data acquisition devices were mounted on the bicycle during testing. While not all of the recorded data was used in the results presented in this project, the full dataset has been retained and is available for future analysis.

2.2.1. Inertial Measurement Units

Linear accelerations and angular velocities along three axes were measured using wearable Consensys Shimmer3 IMUs (Shimmer Sensing, Dublin, Ireland). The sensors were connected to a Consensys Base 6U.01 dock and updated to firmware version LogAndStream v0.11.0. Data acquisition was managed using ConsensysBASIC v0.4.4-64bit on a Dell Precision Tower 5810 running Microsoft Windows 10.

To securely attach the sensors to the bicycle frame, custom supports were designed and 3D printed using PLA material. These supports ensured a firm clamp at each sensor location. Technical drawings of the supports are included in Appendix A. To validate the integrity of these mounts, a dedicated preliminary test was conducted to ensure that the sensor measurements were not biased by mount dynamics. The natural frequencies of the mounts were identified to rule out any potential interference with the frequency range relevant to the study of the vibrations on the whole body vibration. Details of this validation are provided in Appendix E.

Three IMUs were mounted on the bicycle, with an additional unit placed on the rider's chest, as close as possible to the sternum. The positions of the sensors on the bicycle are shown in Figure 2.4, and a more precise location relative to the frame is detailed in Appendix B, along with relevant bicycle parameters and dimensions.

1. **Rear Wheel:** An IMU was mounted on the wheel hub, aligned such that its Z-axis coincided with the wheel's rotation axis. This setup allowed for the estimation of the bicycle's travel speed using:

$$v = \omega_z \cdot r \tag{2.9}$$

   where ω_z is the angular speed of the wheel and r is its radius, which, considering the mounted rim and tire, was 0.34 m.

2. **Handlebar stem:** Another IMU was attached to the stem connecting the fork axis to the handlebar. This location provided the closest possible mounting point to where the rider grips the handlebar. The purpose of this sensor was to measure accelerations transmitted through the hands.

3. **Seatpost:** A third IMU was mounted on the seatpost using a custom 3D-printed part. The objective, similar to the handlebar setup, was to measure accelerations transmitted to the rider through the saddle. The chosen mounting point was the closest rigid connection to the buttocks.

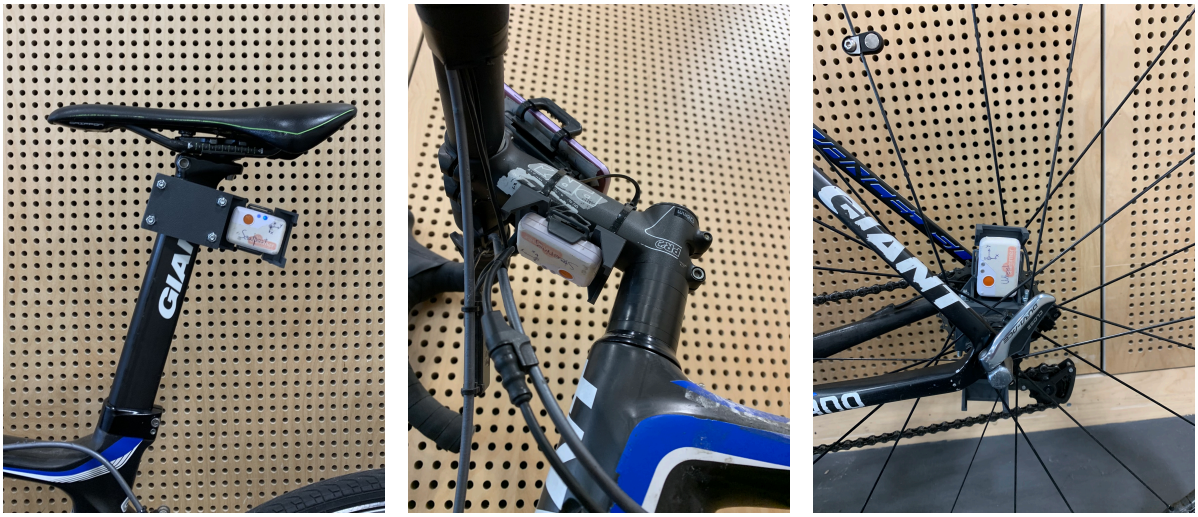

(a) Seatpost (b) Handlebar (c) Wheel

Figure 2.4: Sensors placed on the bicycle.

4. **Sternum:** The final IMU was strapped to the rider's sternum using an elastic band. This sensor was included to log data relevant for calculating transmissibility from the contact points to the rider's upper body.

The target sampling frequency for all IMUs was initially set to 2048 Hz during preliminary tests (see Appendix E) but was later reduced to 1024 Hz for the main experiments. The full-scale range was configured to ± 16 g for the accelerometer (using the 'WR: wide range' setting in the Consensys Shimmer software) and $\pm 2000\ ^{\circ}\,\mathrm{s}^{-1}$ for the gyroscope.

2.2.2. Power pedals

The power input exerted by the rider was recorded using Favero Assioma Duo power pedals (Favero Electronics Srl, Arcade, Italy). These pedals log both pedaling power and cadence. The data were collected using a Nokia 3.4 smartphone (Nokia Corporation, Espoo, Finland), mounted on the handlebar and running the SuperCycle app (Osborn Technologies, Inc., Minnesota, USA). This setup provided real-time feedback to the rider and logged the data for possible later analysis.

2.2.3. Speed sensor

To provide real-time feedback on longitudinal speed, a Giant RideSense 2.0 sensor (Giant Manufacturing Co. Ltd., Taichung, Taiwan) was used. This sensor transmitted speed data via Bluetooth to the same smartphone, where it was displayed and logged through the SuperCycle app alongside power data. This setup enabled the rider to monitor live speed and accurately approach the test section at the intended target velocity.

2.3. Data processing

For data analysis, Python 3.13.1 was used along with the following software packages: Matplotlib 3.9.3, NumPy 2.2.0, Pandas 2.2.3, and SciPy 1.14.1. Additionally, figure formatting throughout the project follows the 'SciencePlots' style package for Python [48].

Throughout the project, a *session* is defined as a continuous data collection period in which multiple conditions and speeds were tested. Each session is divided into *conditions*, each corresponding to a unique combination of parameters being evaluated (tire pressure, posture, rider behaviour, and target speed). Each condition was repeated multiple times, and these repetitions are referred to as *trials*.

All relevant data from the experiments was collected and stored, including: videos (capturing a general view, as well as the start and end of the test stretch), power data logged via the handlebar-mounted smartphone (including power, cadence, and speed), and all IMU measurements (accelerometer and gyroscope data from the four mounting locations described earlier). Ultimately, neither the

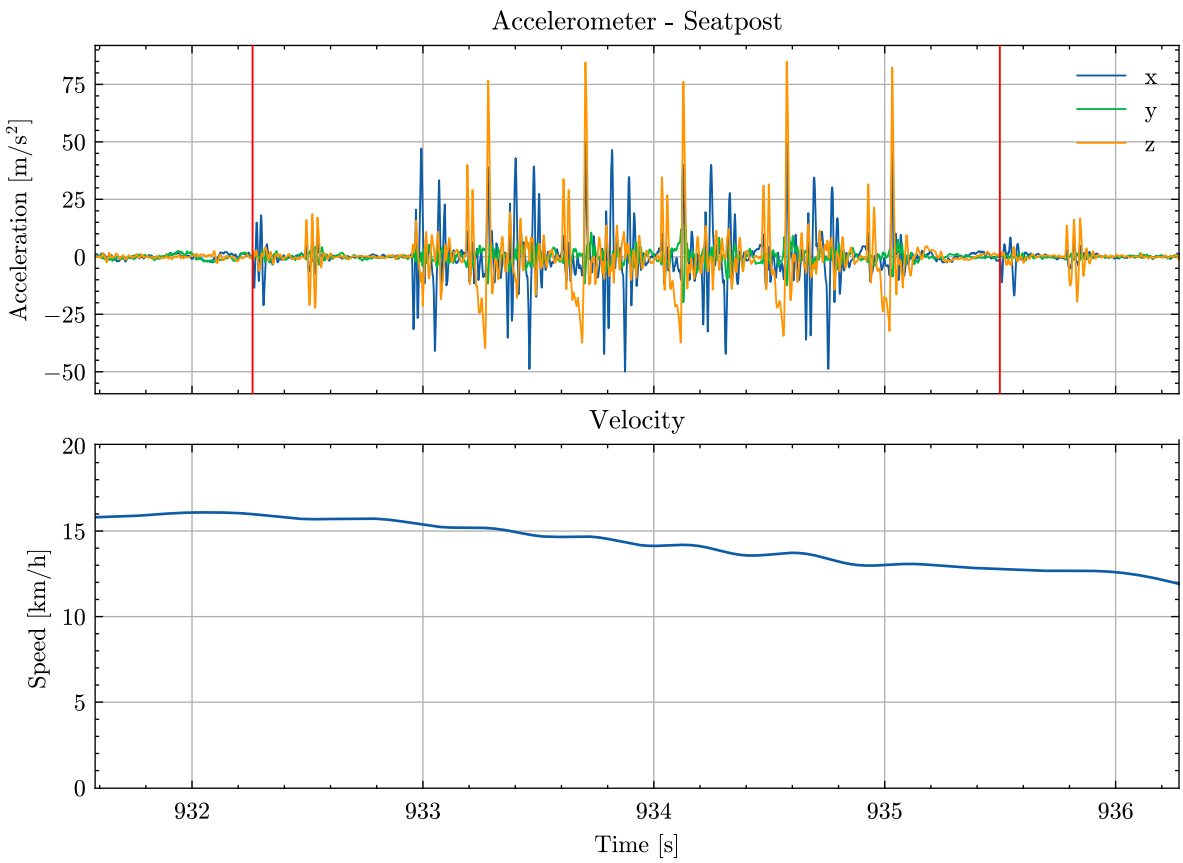

Figure 2.5: Definition of trial windows based on seatpost acceleration signals, identifying the moments the bicycle passes over the starting and ending thin slats.

video recordings nor the smartphone and IMU-based accelerometer data were used in the final analysis of the results presented in this work. However, these datasets remain available and can be utilized for future analyses.

Each IMU generated a comma-separated values (CSV) file per session, containing time series data: linear acceleration and angular velocity along the IMU's three axes, along with Unix epoch timestamps. Trial segmentation was performed manually by identifying the moments when the bicycle entered and exited the controlled section. This was done using the vertical acceleration signal from the seatpost IMU, which registered clear spikes as the bike passed over the small slats marking the start and end of the stretch. An example of this segmentation process is shown in Figure 2.5.

To condition the data, appropriate filtering was applied depending on the sensor and the signal of interest. For the wheel IMU, the relevant data is the angular velocity about the wheel axis, used to derive forward speed. Since only the low-frequency component of this signal is relevant (i.e., gradual speed loss over time), a 2nd order Butterworth low-pass filter with a cutoff frequency of 2.5 Hz was applied. In contrast, for the accelerometer data from the handlebar, seatpost, and sternum IMUs, filtering was applied according to ISO 2631-1 [49], as it provides the standard framework for analyzing and assessing accelerations transmitted to the whole human body, which best matches the characteristics of cycling-induced excitations. Specifically, a zero-lag 2nd order Butterworth low-pass filter with a cutoff frequency of 120 Hz was used, based on the standard's upper frequency limit of 80 Hz and the recommended safety margin of 1.5.

The data was processed on a per-session basis as follows:

1. Compute the vehicle's travel speed from the angular velocity of the rear wheel using the known wheel radius of 0.34 m.

2. Rotate the accelerometer data from each IMU from its body-fixed sensor coordinates to the bicycle's body-fixed frame. This involved projecting the accelerations into the standard SAE body

axes [50]: longitudinal (x), lateral (y), and vertical (z). The mounting ensured approximate alignment of one sensor axis with the pitch axis of the bicycle.

3. Apply filtering to the sensor data depending on the intended use.
4. Remove the influence of gravity from the acceleration data using a second order Butterworth high-pass filter with a cutoff frequency of 1 Hz [51].
5. Manually segment each trial based on peaks detected by the seatpost accelerometer, identifying impacts from the initial and final slats of the test section.
6. Assign condition metadata (target speed, posture, rider behaviour, tire pressure) to each segmented trial.
7. Calculate the energy loss for each trial and derive the corresponding average power loss.

This process yielded 434 identified trials for analysis. After applying quality filters, such as requiring that the entry speed fall within 10% of the target speed, a total of 334 trials were considered valid. From which 71 trials were used to fit the rolling resistance and aerodynamic drag coefficients. All session-specific metadata, including paths to the raw data files, is documented in a dedicated `Sessions_data` file.

2.4. Parameters and model fitting

2.4.1. Speed and pressure relation

Based on preliminary analysis of the collected data during the experiment, vibration losses appeared to vary with speed and tire pressure. To further investigate and characterize these dependencies, a curve fitting procedure was incorporated into the methodology. Given that both speed and tire pressure are continuous variables, linear and quadratic regression models were selected to assess the nature of their relationship with vibration losses. The following equations were used:

$$\text{Vibration Losses}_{\text{linear}} = a_1 x + b \tag{2.10}$$

$$\text{Vibration Losses}_{\text{quad}} = a_2 x^2 + b \tag{2.11}$$

where x represents either speed or tire pressure, a_1 and a_2 are the fitted coefficients, and b is the intercept.

In both parameter fitting procedures, constraints were applied to ensure physically meaningful results. Specifically, all fitted curves were required to yield positive power losses by enforcing positive coefficients. For the speed dependency, an additional constraint was imposed: both the linear and quadratic fits were forced to pass through the origin, i.e., the intercept term was set to zero ($b = 0$), ensuring that no vibration losses occur at zero speed. In contrast, for the pressure dependency, no such constraint was applied beyond the requirement of positive coefficients.

To evaluate the quality of the fitted models, the coefficient of determination (R^2) was used. The R^2 value, also known as the coefficient of determination, indicates the degree to which the model explains the observed variation in the dependent variable, vibration losses, relative to the mean of the data [52]. In this context, it quantifies how well the changes in pressure or speed account for the changes in vibration losses. An R^2 value closer to 1 suggests that the model explains a greater proportion of the variation in the data.

2.4.2. Model proposal

Following a data-driven approach, the results from the previous curve fits were assessed to inform the development of a predictive model for vibration losses. This proposed model incorporates the three main factors found to significantly influence vibration-induced power loss: rider posture, tire pressure and velocity. The rider behaviour parameter was excluded from the model due to the absence of a consistent trend in the experimental data.

The fitted model is defined as follows:

$$VL = K(a \cdot Press \cdot v^2) \tag{2.12}$$

In this model, the vibration losses VL are assumed to be linearly dependent on the tire pressure $Press$ and quadratically dependent on the velocity v. The coefficient K represents a posture-specific scaling factor, with separate values fitted for the 'seated' and 'off the saddle' postures, denoted as K_{seated} and $K_{offsaddle}$ respectively. The coefficient a is a global scaling parameter fitted across all data.

While this model introduces a simplified representation of the contributing factors, it provides a first approximation to understand how vibration losses evolve across the tested parameter space. Its limitations and potential improvements will be discussed in a later section.

To evaluate the effectiveness of the model, its fit to the experimental data is assessed using the coefficient of determination (R^2), which reflects how well the model captures the variance in observed vibration losses and reflects its ability to approximate the underlying trends in the trials.

3

Results

This chapter presents the outcomes of the experiments described in the previous sections. However, it is important to acknowledge a practical limitation encountered during the session involving the highest target speeds (25 and 30 km/h), related to both reaching the required speed and braking safely after the test stretch.

During this session, tests at 30 km/h were successfully completed for the 3.5 bar tire pressure condition. However, for safety reasons, the number of tested conditions at these higher speeds was reduced to include only the 'Seated' posture and 'Normal' behaviour. This decision ensured better control of the bicycle and avoided potential safety risks. Consequently, the analysis at 30 km/h is limited to the normal and seated rider condition. Additionally, the IMU mounted on the rider's sternum failed to record data during this session, preventing future transmissibility analysis for the 25 and 30 km/h trials.

All trial results used to generate the plots in this chapter are detailed in Appendix F, including both individual trial data and aggregated results per tested condition.

3.1. Reference tests

As described in the methodology, a dedicated session was conducted to estimate the called 'reference losses', which include the aerodynamic drag and classical rolling resistance. These are quantified by the product of the drag coefficient and frontal area (C_dA), also called drag area, and the rolling resistance coefficient (C_{rr}), respectively. A total of 71 coast-down trials were performed on a flat, obstacle-free 25 m stretch, covering the full range of speeds and configurations that influence these coefficients. It is assumed that C_{rr} varies only with tire pressure, while C_dA is affected by rider posture.

By fitting the observed power loss from these trials to the power model (Equation 2.2), and considering that vibration losses were absent during these runs, estimates for the aerodynamic (C_dA) and

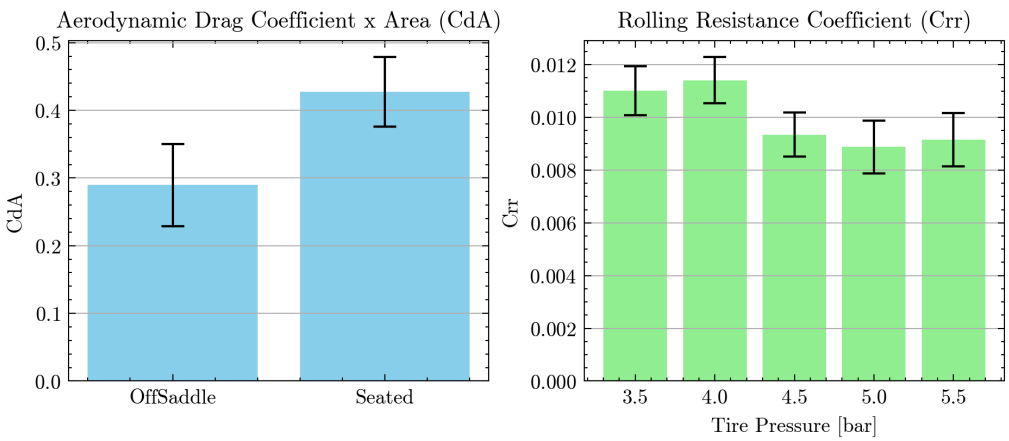

Figure 3.1: Fitted values of C_dA by posture and C_{rr} by tire pressure, obtained from reference coast-down trials.

Posture	C_dA	C_dA std	C_dA std (%)	trials count
OffSaddle	0.28978	0.06081	20.98383	26
Seated	0.42737	0.05166	12.08799	45

Table 3.1: Aerodynamic coefficient fitted per posture tested.

Tire Pressure [bar]	C_{rr}	C_{rr} std	C_{rr} std (%)	trials count
3.5	0.01101	0.00093	8.48862	18
4.0	0.01141	0.00088	7.73178	18
4.5	0.00934	0.00084	9.00781	17
5.0	0.00888	0.00100	11.30606	9
5.5	0.00916	0.00101	11.08058	9

Table 3.2: Rolling resistance coefficient fitted per tire pressure tested.

rolling resistance (C_{rr}) coefficients were obtained.

The resulting values from the fits are summarized in Tables 3.1 and 3.2, and illustrated in Figure 3.1. The individual trial data used for these fits can be found in Appendix F. The results indicate that the 'seated' posture yields a higher aerodynamic resistance coefficient than the 'off the saddle' posture. For rolling resistance, a decreasing trend in C_{rr} is observed with an increasing tire pressure.

3.2. Vibration losses per condition

To provide a comprehensive visualization of the vibration losses across different conditions, a three-dimensional representation was generated using a cubic interpolation to generate smooth and realistic trends across the parameter space, see Appendix G. In these graphs, vibration losses are indexed by two continuous parameters: speed and tire pressure, after discounting the rolling resistance and aerodynamic power as described in Section 2.1.1, using the fitted values shown in Figure 3.1.

In the case of the normal behaviour in the seated posture, the tests allowed results to be shown

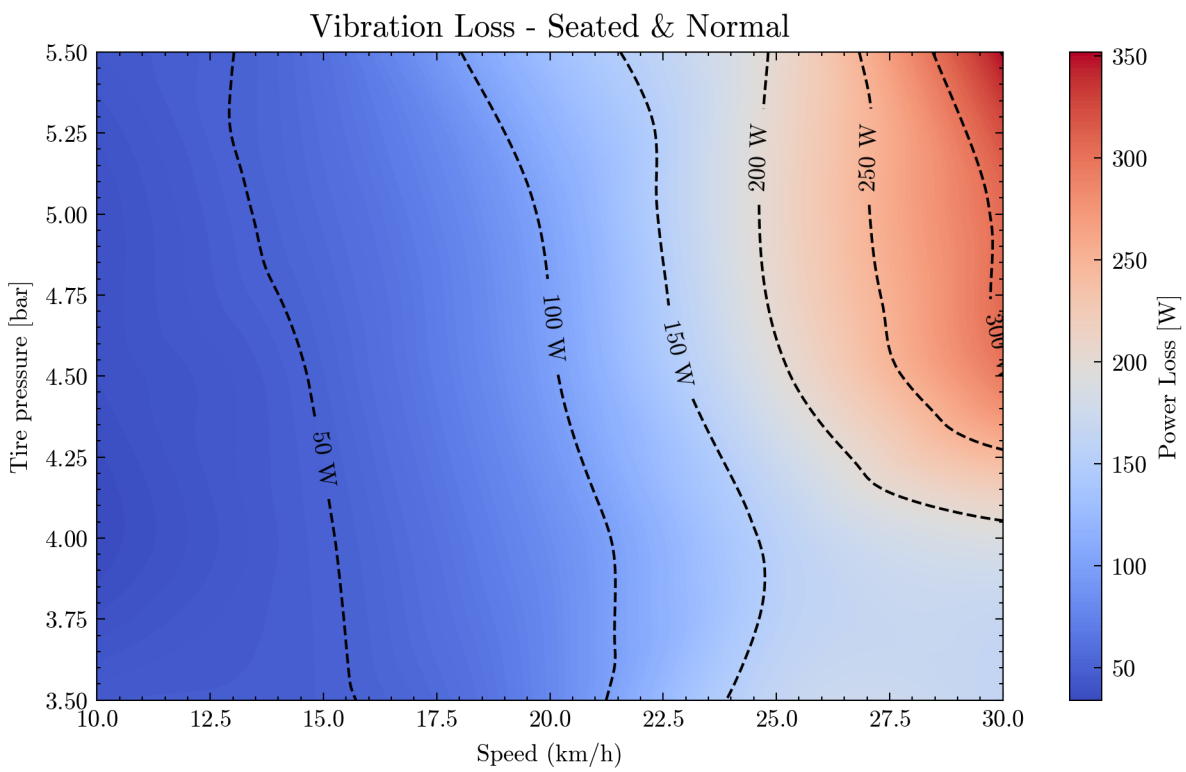

Figure 3.2: Power losses for the natural seated posture and behaviour of the rider.

up to 30 km/h. Figure 3.2 shows the vibration losses found for this condition using 75 trials to create the interpolation space. It can be seen that, in general, higher speed and higher tire pressure result in greater power loss due to vibrations, reaching a maximum value of 351 W when riding over the surface at 30 km/h with a tire pressure of 5.5 bar.

In these figures, a color gradient is used to illustrate the evolution of power loss, and iso-power lines have been added to support interpretation and identification of vibration loss magnitudes across the parameter space.

It can be observed that at lower speeds, vibration losses increase more gradually with pressure than they do at higher speeds. For instance, the 50 W iso-line appears at around 16 km/h for 3.5 bar, and around 13 km/h for 5.5 bar, showing a 3 km/h difference over a 2 bar pressure change. Meanwhile, for the 200 W line, it appears at 25 km/h for 5.0 bar but does not appear before the maximum tested speed of 30 km/h for pressures below 4.0 bar, indicating a 5 km/h shift for just a 1 bar difference.

3.2.1. Comparison of rider conditions

The same plotting procedure was applied across all conditions, enabling direct comparisons between different rider behaviours and postures. To ensure consistency and reliability, the comparison was limited to a maximum speed of 25 km/h, the highest speed for which complete and valid datasets were available across all tested conditions. Consequently, Figures 3.3a and 3.3b display results only up to 25 km/h, using a common color-map scale for consistency. Table 3.3 lists the number of trials used to generate the interpolation space for each condition. Note that the ‘Seated - Normal’ condition includes data up to 30 km/h (75 trials), although the comparison plots are cropped at 25 km/h, higher-speed data remains included in the interpolation for improved accuracy.

Behaviour comparison

Figure 3.3a compares the effect of rider behaviour (muscle contraction level) on vibration losses under the seated posture. Across all behaviours, the general trend holds: higher tire pressures lead to increased vibration losses, especially at higher speeds.

The relaxed behaviour condition exhibits the lowest vibration losses at lower speeds, with the 40 W iso-line appearing at approximately 15 km/h and losses not exceeding 170 W across the tested parameter space. In contrast, the stiff behaviour starts with the 40 W line already at around 12 km/h, but with maximum values reaching only about 140 W, indicating a more compressed power loss range.

The normal behaviour condition shows the highest losses in this comparison. The 40 W iso-line again appears at about 12 km/h, but the losses extend beyond 200 W, marking it as the most dissipative of the three behaviours tested.

For both the stiff and normal behaviours, a local minimum in vibration losses appears around 4.0 bar tire pressure. This is visible as an outward shift in the iso-power lines near this pressure, where the same power levels occur at relatively higher speeds. In the relaxed behaviour, a similar outward shift is observed, but it seems to appear at lower pressures outside the parameter space.

Posture comparison

Figure 3.3b shows the comparison between the two riding postures: ‘Seated’ and ‘Off the Saddle’. In the off the saddle condition, lower vibration losses are observed across the entire parameter space. For example, the 20 W iso-line appears at low speeds, even extending to 15 km/h at 4.0 bar pressure, whereas in the seated condition, the 40 W line is the lowest visible iso-line.

While both postures follow the same general trend of increased vibration losses with higher speed and tire pressure, the absolute magnitudes differ. The seated posture reaches a maximum value of approximately 200 W, while the off the saddle posture peaks around 140 W. In both cases, iso-power lines appear to shift toward higher speeds at pressures near 4.0 bar.

Condition (Posture-Behaviour)	Count
OffSaddle - Normal	60
Seated - Normal	75
Seated - Relaxed	60
Seated - Stiff	66

Table 3.3: Number of trials used to generate the parameter space for each tested condition.

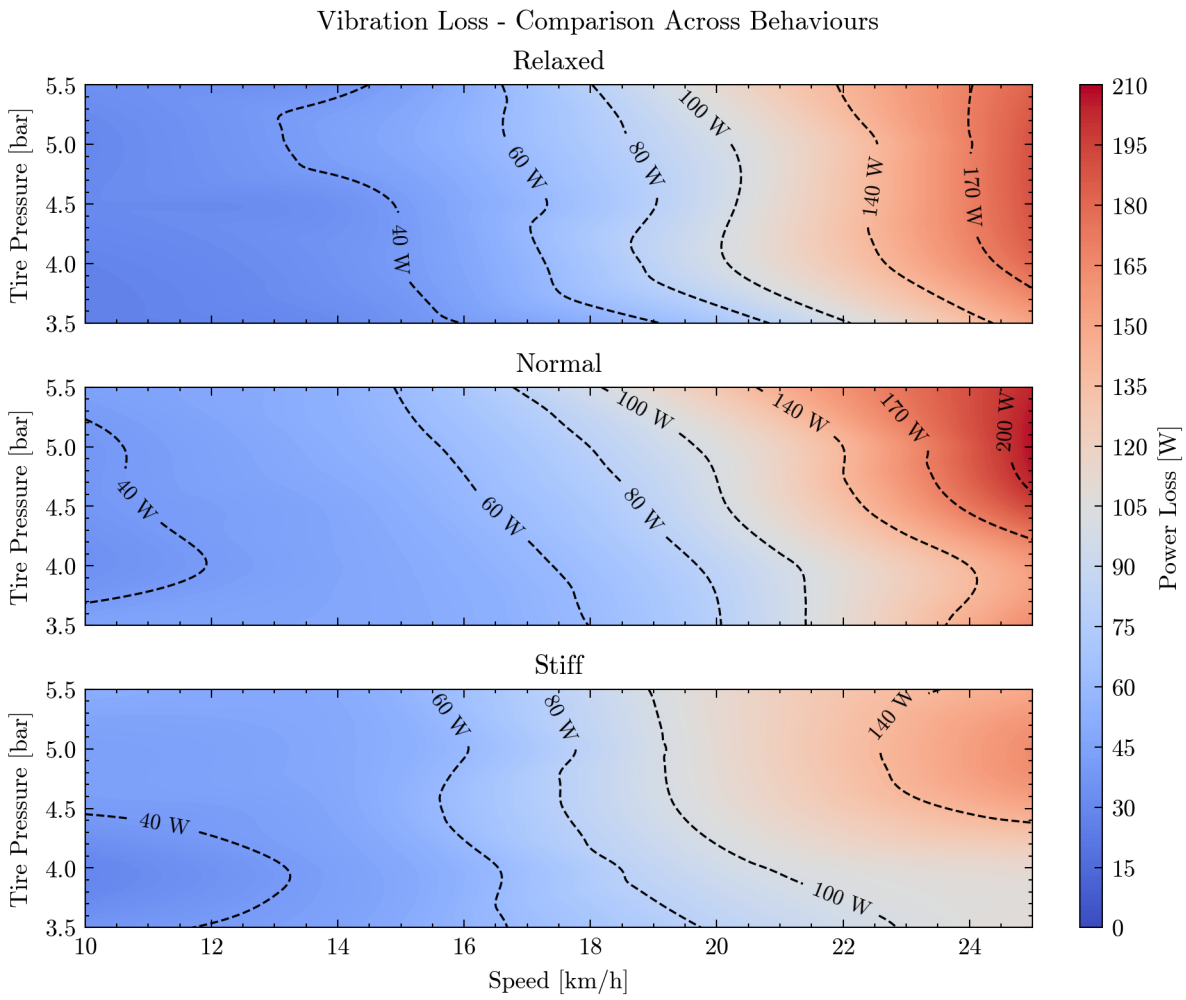

(a) Behaviours comparison.

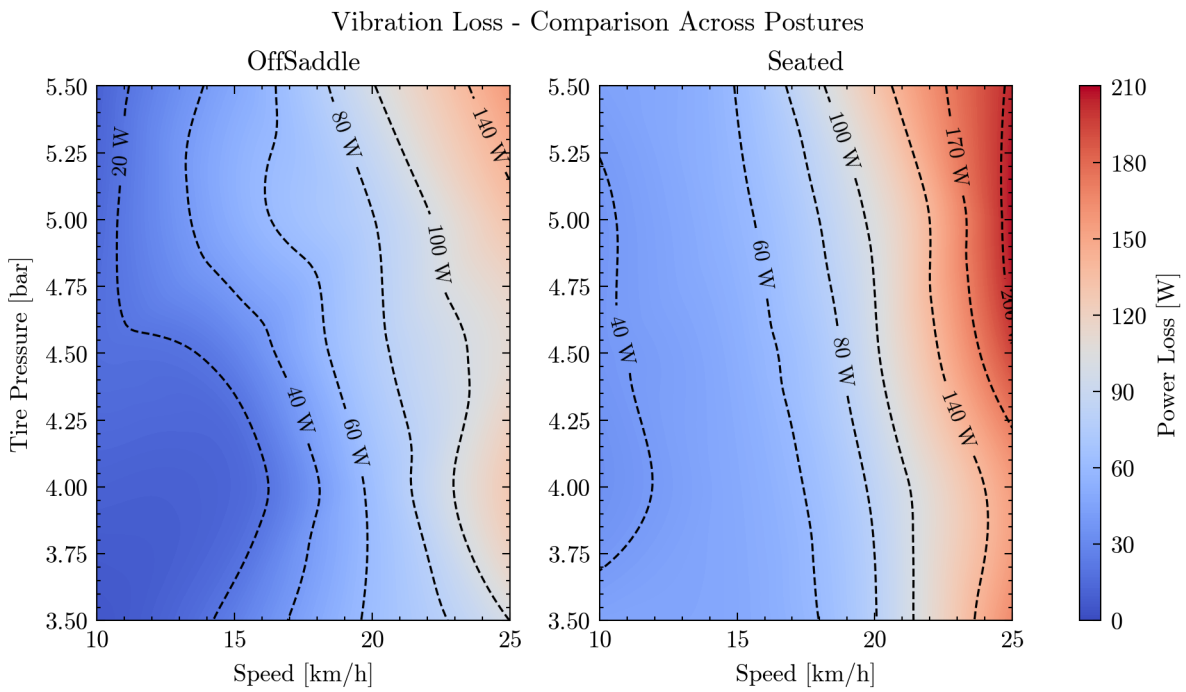

(b) Postures comparison.

Figure 3.3: Comparison of the vibration losses, depending on the rider conditions.

3.3. Vibration losses contribution to the general power losses

Figure 3.5 displays the composition of total power loss into its three primary components: aerodynamic losses, pure rolling resistance and vibration losses. This figure provides a more detailed overview of the data used to generate the parameter spaces presented earlier and it facilitates a condition by condition comparison across parameters such as tire pressure and speed. Note that the subplots use different vertical axis scales to improve visual clarity. Additionally, due to testing constraints at 30 km/h, only the 'Seated/Normal' condition includes data at that speed, all other plots are limited to 25 km/h.

3.3.1. Posture and behaviour influence

Comparing the posture in Figure 3.5, the 'Off the saddle' posture consistently exhibits lower power losses than the 'Seated' posture across all tested pressures and speeds. For example, at 10 km/h and 3.5 bar, vibration losses are approximately 6 W in the 'Off the saddle' case compared to 45 W in the 'Seated' case. At 25 km/h and 5.5 bar, these losses increase to 157 W and 203 W, respectively. This posture also influences the total losses due to differing aerodynamic resistance values found.

Regarding the behaviour, the relaxed condition shows slightly lower vibration losses than the normal or stiff behaviours at low speeds. At higher speeds, such as 25 km/h, the stiff behaviour results in the lowest vibration losses, around 150 W, while both the relaxed and normal behaviours approach 200 W. At 20 km/h, all three behaviours yield similar values, with vibration losses converging around 100 W across the different tire pressures.

Additional plots comparing behaviours and postures across speeds can be found in Appendix G, in Figures G.2 and G.3.

3.3.2. Pressure effect

The effect of tire pressure on vibration losses is also shown in Figure 3.5, where a consistent trend is observed across all rider conditions and speeds: vibration losses increase with higher tire pressures. This effect becomes more pronounced at higher speeds. For instance, under the normal behaviour and seated posture condition, vibration losses at 30 km/h increase from 164 W at 3.5 bar to 351 W at 5.5 bar. At a lower speed of 15 km/h, the range is notably smaller, increasing from 48 W to 60 W over the same pressure interval. A more direct comparison across speeds is presented in Figure G.4 in Appendix G.

To further illustrate the influence of pressure on the relative contribution of vibration losses, Figure 3.4 displays the composition of power losses into aerodynamic, rolling resistance and vibration components for the normal behaviour and seated posture at 30 km/h. As tire pressure increases, the

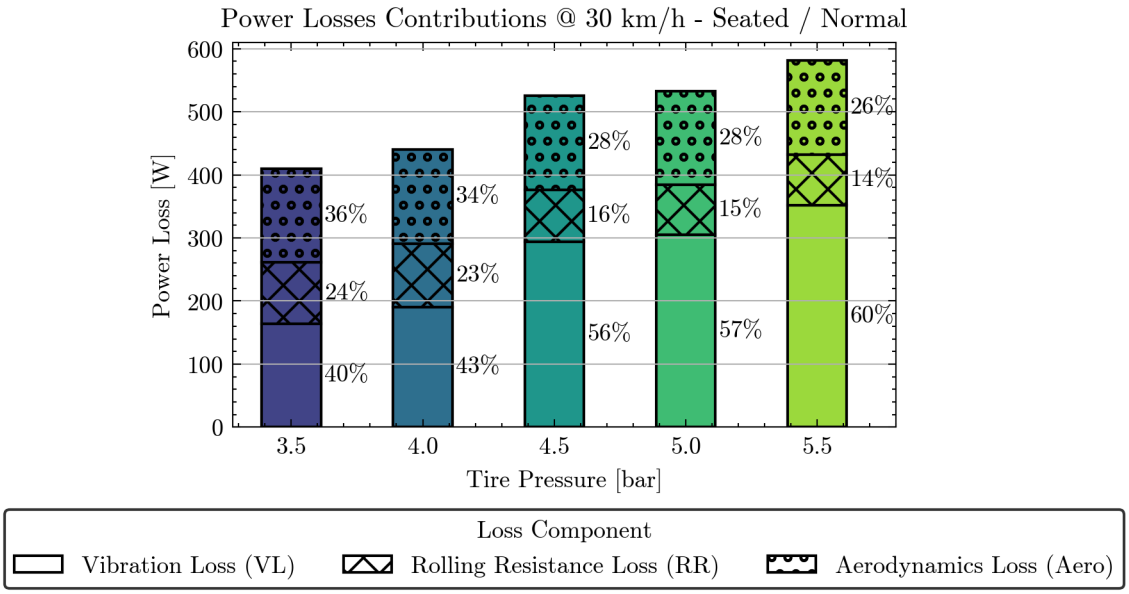

Figure 3.4: Power loss contribution per component for the 30 km/h test across different tire pressures.

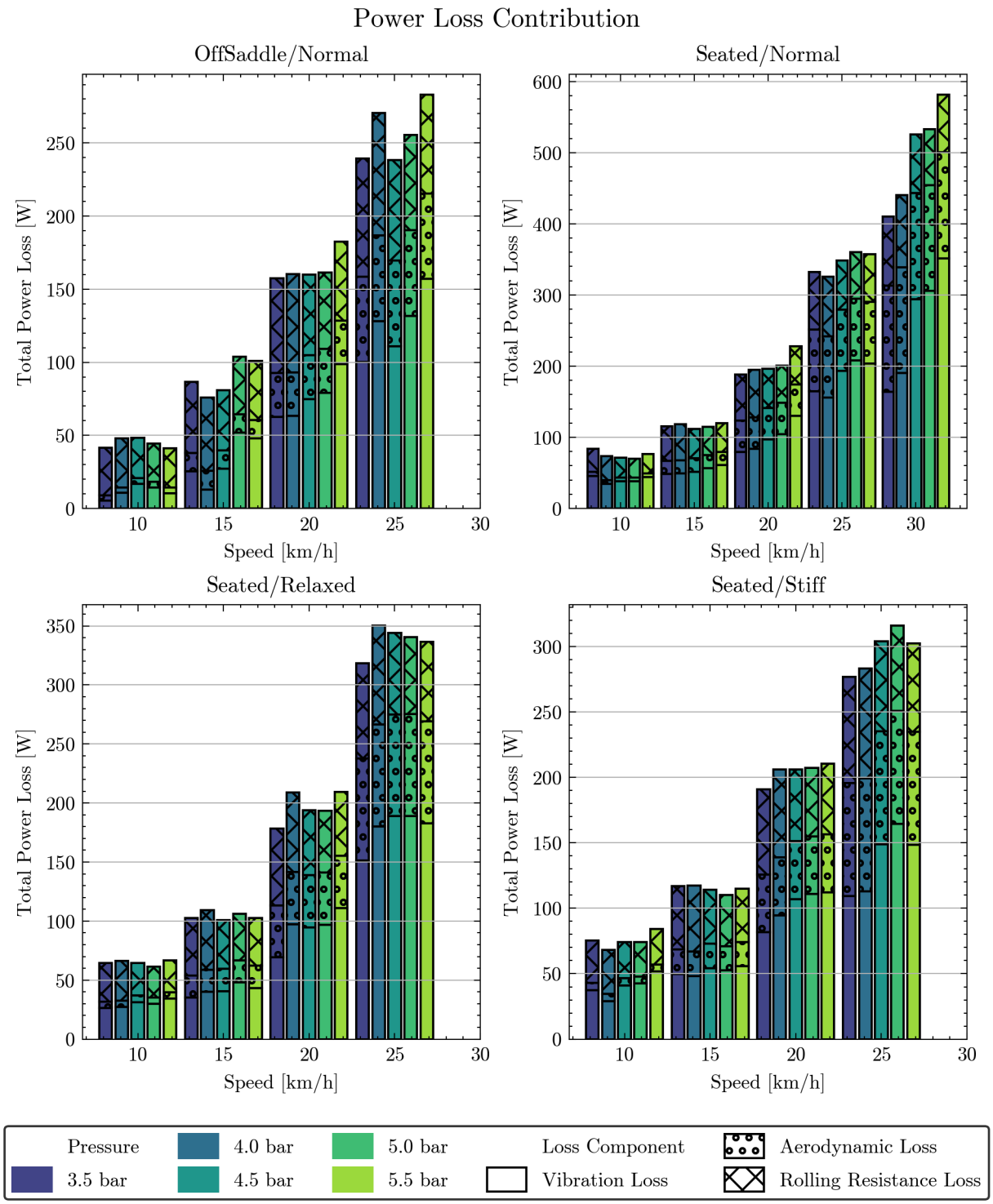

Figure 3.5: Contribution of each power loss component (aerodynamic, rolling resistance and vibration losses) across all posture–behaviour combinations. **Note:** Each subplot uses an individual vertical scale to enhance readability.

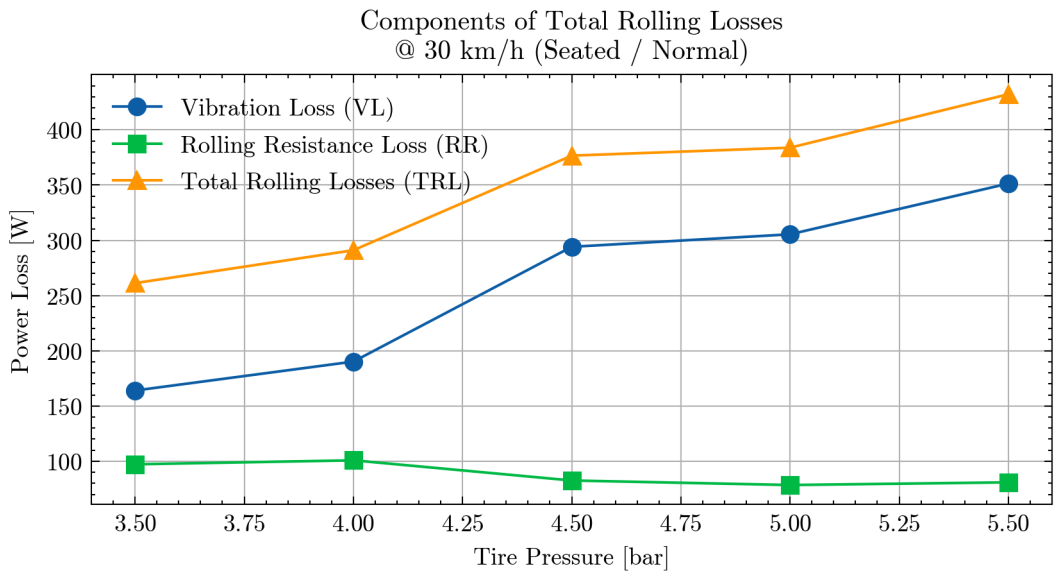

Figure 3.6: Decomposition of total rolling losses into rolling resistance and vibration losses at 30 km/h.

vibration losses contribute a larger share of the total, while rolling resistance losses (based on the previously fitted C_{rr} values) decrease. This trade-off can be observed across all tested speeds, with detailed contributions available in Figure G.6 in Appendix G.

Numerical values for the power loss components across all conditions are provided in Table F.5 in Appendix F. Vibration losses were found to account for between 12.75% (10 km/h, 3.5 bar, off the saddle posture) and 61.38% (10 km/h, 5.5 bar, seated with stiff behaviour) of the total measured power loss.

To facilitate comparison with the hypothesis proposed by SRAM (see Figure 1.2), Figure 3.6 presents the decomposition of total rolling losses into their two components: classical rolling resistance and vibration losses, for the 30 km/h condition. The results here show an increasing trend in vibration losses with pressure, while classical rolling resistance decreases. Equivalent plots for other speeds are provided in Figure G.7 in Appendix G.

3.3.3. Speed effect

Figure 3.5 displays the evolution of total and component power losses with speed per condition. As shown, increasing speed results in higher overall losses, including a notable rise in vibration-induced power losses. This trend is consistent across all rider conditions (i.e. posture, behaviour) and tire pressure. For example, for the seated and normal condition with a tire pressure of 5.5 bar, the vibration losses increase from 43.9 W at 10 km/h to 351.4 W at 30 km/h. A more detailed visualization of speed effects across conditions is provided in Figure G.5 in Appendix G.

3.4. Fitting and model results

3.4.1. Speed dependence

To illustrate the relationship between vibration losses and speed, Figure 3.7 shows the measured vibration losses for all trials conducted at 5.5 bar with normal behaviour, comparing the seated and off the saddle postures. The data points are plotted against the corresponding average trial speeds, and both linear and quadratic regression models, described in Section 2.4, were applied. A visual inspection reveals a closer alignment of the data with the quadratic model.

Equivalent fits for other tire pressures are provided in Figures G.8 and G.9 in Appendix G. Summary statistics for all fits are presented in Table 3.4, listing the coefficient of determination (R^2) for each model. Across all conditions, the quadratic model consistently achieved higher R^2 values. Additionally, for both regression types, increasing tire pressure was associated with steeper fitted curves.

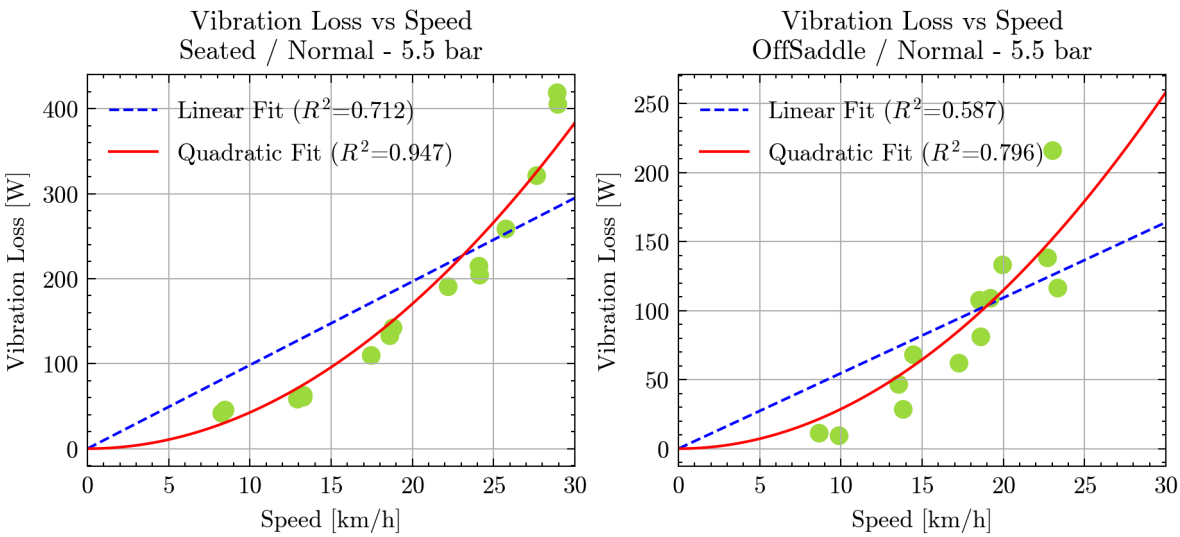

(a) Seated posture.

(b) Off the saddle posture.

Figure 3.7: Curve fitting of vibration losses as a function of speed at 5.5 bar under normal behaviour, for both seated and off the saddle postures.

3.4.2. Pressure dependence

The same fitting procedure was applied to assess the relationship between vibration losses and tire pressure for each target speed tested in the experiment. Figure 3.8 illustrates both linear and quadratic fits for the pressure dependence at 30 km/h, under the normal behaviour and seated posture condition. The differences between the two fits are minimal within the pressure range considered in this study.

Summary metrics for the pressure-based fits are also reported in Table 3.4, where the coefficient of determination (R^2) is used to evaluate model performance. The results show that both linear and quadratic models perform comparably across the tested conditions, with only minor differences in R^2. Furthermore, an increase in speed consistently results in steeper slopes for both fitting approaches.

3.4.3. Model fit

Fitting the trial data to the model described in Equation 2.12 yields the coefficients shown in Table 3.5. For ease of application, the speed is expressed in *km/h* and the pressure in *bar*. The model with these

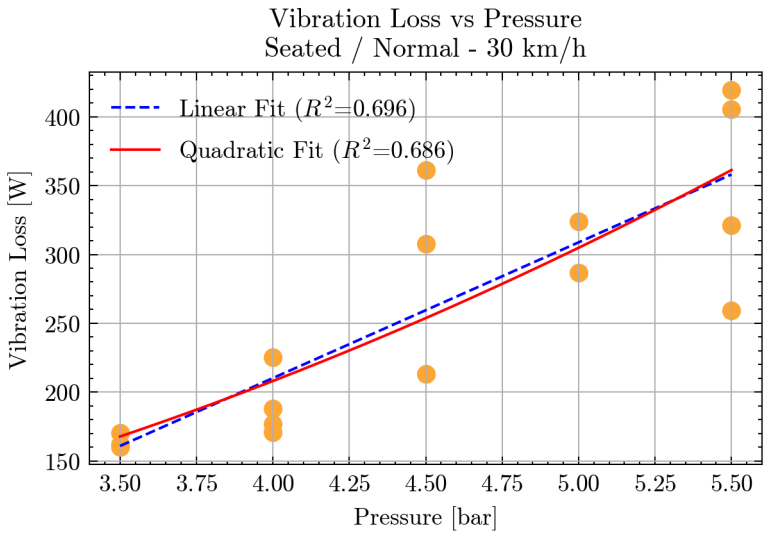

Figure 3.8: Curve fitting of vibration losses as a function of pressure at 30 km/h under normal behaviour and seated posture.

Posture	Pressure [bar]	Linear Fit	R^2 Linear	Quadratic Fit	R^2 Quadratic
			Speed relation		
Seated	3.5	$5.768x$	0.811	$0.247x^2$	0.805
	4.0	$6.016x$	0.831	$0.252x^2$	0.945
	4.5	$8.343x$	0.684	$0.361x^2$	0.872
	5.0	$8.401x$	0.760	$0.382x^2$	0.978
	5.5	$9.833x$	0.712	$0.426x^2$	0.947
Off saddle	3.5	$3.264x$	0.561	$0.155x^2$	0.698
	4.0	$3.666x$	0.413	$0.197x^2$	0.602
	4.5	$4.106x$	0.344	$0.209x^2$	0.427
	5.0	$4.563x$	0.559	$0.235x^2$	0.702
	5.5	$5.463x$	0.587	$0.287x^2$	0.796
			Pressure relation		
Seated	10	0.000x + 40.433	0.000	$0.000x^2$ + 40.433	0.000
	15	6.479x + 24.289	0.502	$0.728x^2$ + 38.322	0.514
	20	25.588x - 15.488	0.809	$2.848x^2$ + 40.414	0.829
	25	25.452x + 70.962	0.567	$2.822x^2$ + 126.843	0.560
	30	98.643x - 184.428	0.696	$10.756x^2$ + 35.952	0.686
OffSaddle	10	3.768x - 5.627	0.195	$0.394x^2$ + 3.105	0.168
	15	15.909x - 37.193	0.412	$1.788x^2$ - 2.810	0.421
	20	18.832x - 8.700	0.212	$2.093x^2$ + 32.519	0.218
	25	24.590x + 13.927	0.099	$2.774x^2$ + 66.959	0.102

Table 3.4: Fit summary per pressure for vibration loss vs speed for the normal behaviour and seated posture.

a $[Wh^2km^{-2}bar^{-1}]$	K_{seated}	$K_{offsaddle}$	R^2
0.250	0.298	0.193	0.883

Table 3.5: Fitted coefficients for the model $VL = K(a \cdot \text{Press} \cdot v^2)$, where speed is in *km/h* and pressure in *bar*. Also included the coefficient of determination R^2.

coefficients yields a coefficient of determination of $R^2 = 0.883$.

The model output is visualized for the 5.5 bar trials under normal behaviour in Figure 3.9, covering both seated and off-the-saddle postures. Extended plots for other pressures are available in Figures G.10 and G.11 in Appendix G.

To evaluate how well the model captures the trends observed in the full parameter space, its output is compared to the cubic-interpolated surface shown earlier in Figure 3.3b. The power differences between the interpolated surface and the fitted model are presented in Figure 3.10, which reveals a slight tendency of the model to overestimate power losses compared to the cubically interpolated estimation.

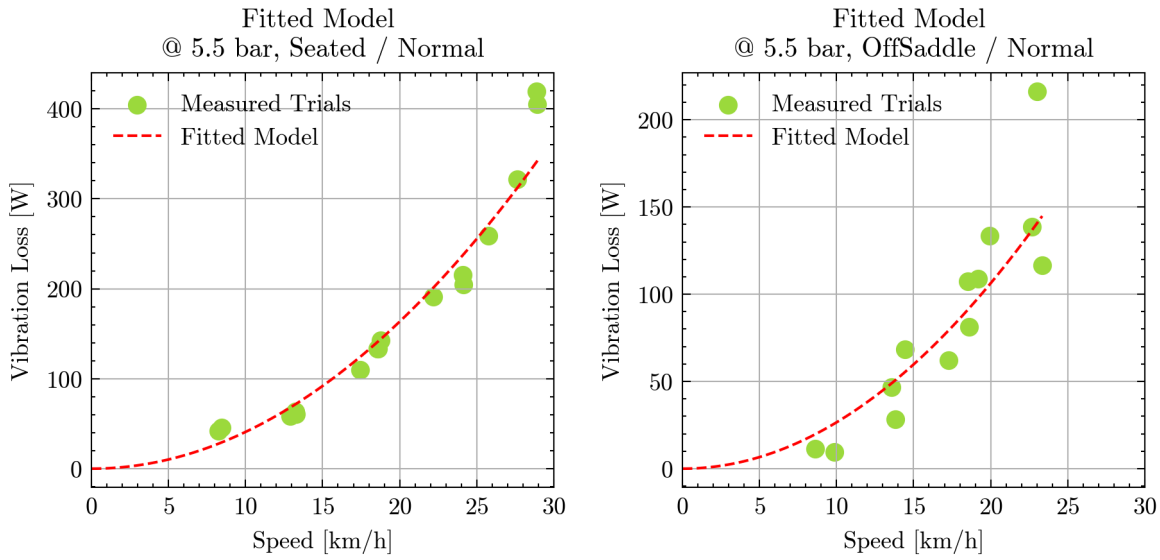

(a) Seated posture.

(b) Off the saddle posture.

Figure 3.9: Fitted model of vibration losses for trials at 5.5 bar under normal behaviour, incorporating both seated and off the saddle postures.

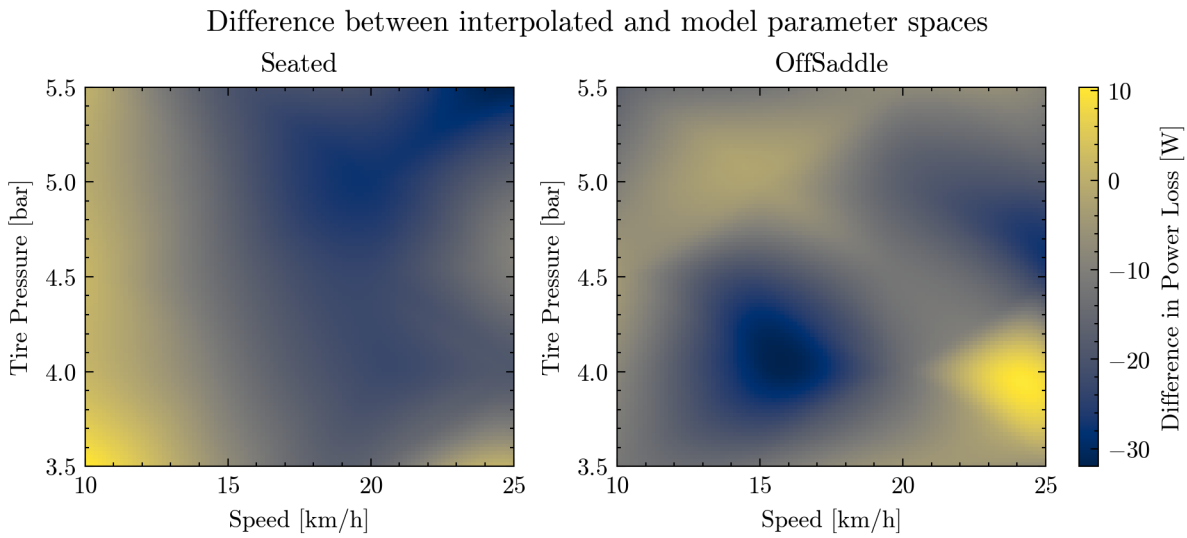

Figure 3.10: Power differences between the interpolated surface and the fitted model.

4 Discussion

With the experiment described and the results presented, a set of power loss measurements has been obtained for a simulated rough road condition, specifically resembling a cobblestone surface. Vibration losses were estimated by subtracting the aerodynamic and rolling resistance losses, determined from reference coast-down tests, from the total measured power loss. These vibration losses were analysed across various test parameters: speed, tire pressure, rider behaviour and posture.

It is important to note that the trends and conclusions discussed are based on average values per test condition. Linear and quadratic regression fits, along with the coefficient of determination (R^2), were used to explore and describe the relationships between vibration losses, speed and pressure. However, these analyses are primarily descriptive. No formal statistical testing was conducted to assess the significance of differences across rider posture or behaviour. A more rigorous statistical approach would be required to confirm the robustness of these trends.

The results show that vibration-induced power losses range from approximately 5 W to 350 W, accounting for up to 60% of the total power losses observed in some trials. This highlights the significant contribution of vibration losses under rough road conditions.

Compared to previous literature, these results offer a more controlled and detailed evaluation of vibration-related losses. For instance, Heine [40] reported vibration losses up to 290 W at 25 km/h. However, the lack of details of the procedure in that study, combined with images suggesting a lighter rider, raises questions about the accuracy and comparability of the reported values. In this project, for similar conditions, seated posture and normal behaviour, the measured vibration losses at 25 km/h reach up to 210 W, depending on tire pressure. Given that the rider used in this study weighed 100 kg, compared to what appears to be a significantly lighter rider in Heine's work, higher power absorption would be expected here due to the influence of body mass on energy dissipation [12].

The testing surfaces also differ: the current study used wooden planks with 20 mm height, likely producing stronger excitations than the unspecified rumble strips used by Heine. Furthermore, differences in bicycle characteristics, such as frame type, tire model or suspension, may have significantly influenced vibration transmission and energy loss, making direct comparison between studies problematic.

In the context of human-body vibration absorption, Pradko [27] recorded up to 920 W of absorbed power in isolated laboratory settings. The maximum 351 W observed in this study falls well within plausible values. However, it is not possible to determine the expected power absorbed by the human body from these results, as the displacement amplitude, used to relate losses to frequency, is not clearly defined. It is unclear whether it refers to peak to peak amplitude, half of that, or another metric [13].

More directly comparable to this project are the results from Vanwalleghem [30], who reported 44 W of vibration losses while riding over cobblestones at 15 km/h. Under the same conditions (normal behaviour, seated posture, and 15 km/h), this project measured up to 130 W of vibration losses. Several factors may explain this difference. First, the current study accounts for losses not only in the human body but also in bicycle components and road interaction. Second, the rider in this study weighed 100 kg versus 75 kg in Vanwalleghem's, affecting the system's overall power dissipation. Finally, although both studies used cobblestone surfaces, differences in the actual surface roughness may have

played a role, although such a comparison cannot be confirmed without more detailed information from Vanwalleghem's work.

4.1. Aerodynamics and rolling resistance estimation

From the coast-down tests performed without any obstacles, the aerodynamic and rolling resistance coefficients were fitted for each of the conditions that influence them. Regarding the aerodynamic results obtained, the 'off the saddle' posture resulted in a lower value compared to the seated posture. The improved aerodynamics in this position can be attributed to two main factors. As seen in Figure 2.2, the off the saddle posture aligns the upper body more closely with the direction of airflow, becoming nearly horizontal. This also reduces the frontal area from the full torso to primarily the shoulders. Together, these two effects lead to a reduced drag area, which is captured in the fitted value for C_dA, incorporating both the drag coefficient (C_d) and the frontal area (A). The C_dA value obtained for the seated posture, approximately 0.42, lies within the range of 0.40-0.56 reported in the literature, such as in Tengattini [47], validating the result.

For the rolling resistance coefficient (C_{rr}), the expected trend was a decrease with increasing tire pressure. This is due to the reduction in contact patch area and the associated rubber deformation at higher pressures. While this trend was generally observed, the fitted coefficient for 4.0 bar appears to be non-representative of the overall trend. Including a larger dataset in the fitting process could help better capture this trend more accurately and adjust any inconsistencies in the result. In terms of magnitude, the fitted C_{rr} values around 0.010 are slightly higher than typical values, which usually range from 0.0046 to 0.0066 according to Tengattini [47]. This deviation is likely due to the test surface, as the sports hall floor used in the experiment is not a rigid, non-deformable pavement but instead includes a soft rubber layer. If the surface deforms under the bicycle's contact patch, it is reasonable to expect higher rolling resistance values, as suggested by Fenre [4].

4.2. Vibration losses results

4.2.1. Behaviour effect

The comparison of rider behaviour does not yield sufficiently consistent results to draw definitive conclusions. However, the evolution of vibration losses across speeds reveals some notable patterns. At lower speeds, vibration losses follow a consistent order: relaxed behaviour shows the lowest losses, followed by normal, and then stiff behaviour. This suggests that increased muscle contraction and tighter coupling between the rider and bicycle may lead to greater vibration energy transfer at low speeds. However, at 20 km/h, this pattern becomes less clear. The values for different behaviours begin to overlap and no consistent trend emerges across tire pressures. Interestingly, the tendency observed at low speeds appears to reverse at higher speeds (25–30 km/h), where the stiff behaviour presents the lowest vibration losses and the relaxed behaviour the highest.

This phenomenon could be explained by changes in the rider's biodynamic properties as behaviour is altered. Specifically, increasing muscle tension increases body stiffness, which in turn raises the resonant frequency of the system [34, 12]. Given that the human body's resonant frequency is typically around 5 Hz [12, 31, 32], this shift may bring the body's resonance closer to the excitation frequencies encountered at higher speeds, around 12 Hz at 25 and 30 km/h. Such resonance alignment could influence the power absorbed due to vibrations. However, this remains speculative, as the actual resonance frequency of the specific rider is unknown. A detailed biodynamic study of the rider would be necessary to confirm whether the resonance shift indeed coincides with the excitation frequency.

Additional considerations include the metabolic cost of each behaviour. Muscle contraction requires energy, and if overall energy efficiency is to be assessed, this physiological cost must also be accounted for. To evaluate this aspect, measurements of oxygen consumption (V_{O_2}) could be incorporated in future studies to quantify metabolic effort under different riding behaviours. Moreover, rider behaviour was controlled subjectively in this study, making the results difficult to generalize. In particular, while the stiff behaviour did not entirely restrict vibration transmission, the relaxed behaviour provided more freedom for the bicycle to move independently. For more accurate comparisons between behavioural extremes, future assessments should include electromyography (EMG) to monitor muscle activity, and tests should ideally be performed using cleats pedals to more closely replicate professional cycling conditions and connection to the bicycle.

4.2.2. Posture effect

Rider posture is shown to significantly influence power losses during cycling. The off the saddle posture consistently results in lower overall power losses, determined by two contributing factors. First, as discussed previously, this posture reduces aerodynamic drag due to the alignment of the rider's upper body with the airflow and a reduced frontal area. This aerodynamic improvement becomes particularly advantageous at higher speeds. Second, vibration losses in the off the saddle posture are markedly lower, ranging from 8.3% to 88.4% less than those observed in the seated posture when compared across equivalent pressure and speed conditions. For the complete set of comparisons, see Table F.6 in Appendix F. However, this apparent efficiency comes with trade-offs. The off the saddle posture offers reduced control over the bicycle, as reflected in increased lateral-direction vibration amplitudes recorded in the trials. In contrast, lateral vibrations were minimal during the seated posture trials. The reduced control also contributed to lower repeatability in the off the saddle tests, evident from the higher standard deviations in the results, which in turn reduces the reliability of the data for this posture.

Although the off the saddle posture appears more efficient in terms of power loss, the physiological demands and potential for fatigue must also be considered. This posture shifts nearly all body weight onto the legs and arms, which act as the primary load bearing and vibration transmitting interfaces. Over prolonged periods, this can lead to muscle fatigue, particularly in the arms and hands, and may cause discomfort or even pain when riding over very rough surfaces.

4.2.3. Tire pressure effect

From Figure 3.5, a subtle but consistent trend of increasing vibration losses with increasing tire pressure can be observed. This trend aligns with the hypothesis previously outlined by SRAM, illustrated in Figure 1.2. To enable a more direct comparison, equivalent graphs were generated for each tested speed. Figure 3.6 presents the results at 30 km/h, and the remaining speeds are included in Appendix G (see Figure G.7).

The results partially validate the hypothesis. For pressures higher than the theoretical optimum, rolling resistance losses decrease while vibration losses increase with a steeper slope. However, the left side of the hypothesized curve, representing very low tire pressures, was not clearly seen in this project. Pressures below 3.5 bar were intentionally avoided due to safety concerns, specifically the risk of hitting the rim with the obstacles, especially at high speeds. According to the SRAM hypothesis, further lowering pressure should continue to reduce vibration losses, but no lower limit is indicated. Without an assessment of these potentially damaging conditions, this part of the hypothesis remains unverified.

Interestingly, this pressure-dependent trend in vibration losses appears to vary with speed. At lower velocities, tire pressure value has lower influence on vibration losses. In contrast, at higher speeds, the same pressure increases result in substantially steeper rises in vibration losses. This shift in sensitivity will be further explored through the curve fitting results presented in Section 4.3.

It is also worth emphasizing the overall impact of tire pressure on total power loss. While increasing pressure reduces the rolling resistance coefficient (C_{rr}), and thus the associated losses, vibration losses increase with pressure. At lower speeds, this trade-off appears balanced; however, at higher speeds, the increased contribution of vibration losses outweighs the reduced rolling resistance, resulting in higher total losses. This is evident in Figure 3.5. For instance, at 30 km/h, increasing the tire pressure from 3.5 to 5.5 bar leads to vibration losses contributing between 40% and 60% of the total power loss, as shown in Figure 3.4. These findings highlight the critical role of tire pressure in optimizing efficiency, particularly at higher velocities.

4.2.4. Speed effect

As previously mentioned, vibration losses increase significantly with speed. Figure 3.5 demonstrates how these losses escalate rapidly across all posture and behaviour combinations. When analyzing vibration power loss as a function of speed, the trend suggests a nonlinear but quadratic relationship. This observation implies that vibration losses cannot be grouped under the traditional definition of rolling resistance, which is typically modeled as linearly dependent on speed. Consequently, Equation 1.1, which represents the rolling resistance force, should be revised to include a velocity dependent component. This supports the fundamental assumption made in this project, that total rolling losses can be split into two distinct terms. One captured by the classical formulation mgC_{rr} and another defined by the vibration-induced losses $VL(v)$. This second component is not only speed-dependent but also

influenced by rider posture, behaviour and tire pressure.

This observation motivated fitting vibration losses first as a function of speed and then as a function of tire pressure, aiming to develop a more representative predictive model.

4.3. Model fit

4.3.1. Speed dependence

When fitting the linear and quadratic models, one notable aspect is the behavior of the off the saddle posture. As mentioned earlier, this condition introduces greater variability in the data, resulting in less repeatable outcomes under identical trial settings. This increased scatter is evident in Figure 3.7b and becomes even more clear across pressures in Figure G.9. Despite this variability, the fitting results presented in Table 3.4 consistently indicate a better match for the quadratic model compared to the linear one for both postures. This supports the earlier hypothesis that vibration losses are not adequately captured by the classical rolling resistance power loss model, which assumes a linear dependency on speed. These findings highlight the need to consider vibration losses as a separate and significant source of energy dissipation in cycling dynamics.

Additionally, the fitted curves show increasing steepness with higher tire pressures, supporting the observation that pressure becomes more influential in vibration losses at higher speeds.

4.3.2. Pressure dependence

Similar to the speed fits, the off the saddle posture with greater variability in the data, resulted in more scattered results to fit. The fitting outcomes for pressure were less conclusive. As shown in Table 3.4, the comparison between the linear and quadratic models does not indicate a clear preference, both yield very similar coefficients of determination (R^2). Additionally, the overall R^2 values are considerably lower than those observed in the speed fits, suggesting that the models were less effective in capturing the influence of tire pressure on vibration losses.

One contributing factor to the reduced accuracy of the pressure fits may be that the trials were grouped by target speeds (e.g., 10, 15 or 20 km/h), rather than the actual average speeds achieved, which varied slightly from the targets. Given the found importance of speed in determining vibration losses, this grouping likely introduced variability that impacted the quality of the fits.

However, one consistent trend remains: the steepness of the fitted curves increases with speed. This supports the earlier visual observation that the influence of tire pressure on vibration losses becomes more pronounced at higher speeds.

4.3.3. Vibration losses model proposed

As a first attempt to generalize the findings of this study, a model is proposed to describe vibration losses based on the main influencing parameters identified during this project: speed, tire pressure and rider posture. This model is intended as a preliminary approximation, useful for interpretation but not definitive or universally applicable.

From the individual parameter fits, several important trends emerged. First, it became evident that vibration losses are not influenced by speed and pressure independently, but rather show a coupled relationship. This is reflected in the change of steepness of the fitted curves, where increasing pressure in the speed fits, or increasing speed in the pressure fits, both result in steeper slopes. This coupling led to taking the decision to incorporate both variables into a combined model.

Second, the order of dependency was assessed by the regression analysis. While the relationship between vibration losses and speed was consistently better captured by a quadratic fit, pressure did not show a clear distinction between linear and quadratic fits. Therefore, in order to simplify the model, pressure was included as a linear term.

Third, rider posture showed a noticeable effect on the magnitude of vibration losses, with the off the saddle condition consistently reducing losses. Although no formal statistical test was performed, this trend was consistent enough to justify a posture-dependent scaling factor in the model.

Bringing these considerations together, the proposed model, described in Equation 2.12, aims to capture the most relevant influences on vibration losses observed in this study. It assumes a quadratic dependence on speed, linear dependence on pressure and a posture scaling term.

Despite its simplicity, the model achieves a good overall fit, as shown in Figure 3.9, with a coefficient of determination (R^2) of 0.883. This is a strong result, especially considering the inherent variability

introduced by human-in-the-loop measurements [53].

Figure 3.10 presents the difference between the vibration losses interpolated cubically from the experimental data and those estimated by the model. While deviations up to 30 W are observed, these must be interpreted in context: the cubic interpolation represents a higher-order fit to the data, capturing local fluctuations by relying on the immediate surroundings of each point. In contrast, the proposed model offers a generalized surface that describes broader trends across the entire parameter space. As shown in Figure 3.3, the interpolation reveals potential local minima in vibration losses around 4.0 bar, behavior that the linear pressure term in the model cannot reproduce. This highlights one limitation of the current model, as it fails to capture a possible optimal pressure.

The differences seen between the model and the interpolated results can be partly explained by the simplicity of the proposed model. More complex models are better at adjusting to the details of the data and can capture local effects, such as the possible optimal pressure zone suggested by the interpolation. However, adding complexity also increases the risk of overfitting and can make the model less useful for other situations. In this project, the model was kept simple on purpose to keep it easy to understand the contributions found and to apply across different conditions. This trade-off is consistent with the idea behind Akaike's work, which notes that focusing only on how well a model fits the data often leads to choosing overly complex models [54]. For future studies, especially when the goal is to find and confirm patterns like pressure optima or other nonlinear effects, using a more formal model selection method like the Akaike Information Criterion (AIC) is recommended.

4.4. Limitations

The present project and experimental setup involves several limitations that may influence the results obtained. The most relevant are outlined below:

- **Passive rider assumption:** The results assume a passive human rider. In real cycling scenarios, the rider continuously transmits power through pedalling, involving repetitive lower-limb motion that may affect how vibrations are absorbed by the human body.
- **Limited testing speed:** Due to the indoor setting of the experiment, the available space restricted the attainable speeds. Acceleration and braking zones had to be kept short, limiting tests to lower speeds than those typically observed in races such as Paris–Roubaix, where cobblestone sections are ridden at considerably higher velocities.
- **Posture and behaviour repeatability:** The accuracy of the results is sensitive to the rider's consistency in posture and behaviour across trials. Since these are manually adopted and not instrumented, variability between repetitions affects the precision of comparisons.
- **Artificial excitation profile:** The artificial surface used in the tests excites primarily one frequency, whereas real-world road profiles excite a broad frequency spectrum. Although using the Bicycle Roughness Index (BRI) to match the excitation was useful for isolating specific effects and served well as a first approach, it limits the representativeness of the experimental surface, especially given the BRI's sensitivity to the approach angle of the profile.
- **Short coast-down stretch:** The coast-down method restricts the length of the obstacle-filled section. Increasing the number of obstacles could improve the resolution of the measurements, but it would also increase the speed loss during the trial, potentially introducing bias due to the non-linear relationship between speed and vibration losses.
- **Manual segmentation of trials:** Trial start and end times were defined manually based on peaks in the seatpost accelerometer signal. A more accurate approach using sensors would improve the consistency and precision of the data segmentation.
- **Non-professional rider and equipment:** The rider used in the tests was not a professional, and the bicycle setup and components did not reflect those typically used in high-level racing. Therefore, the results may not be directly transferable to elite cycling scenarios.

While the proposed model offers a useful framework to interpret the trends observed in this specific experimental setup, it is not intended as a general formulation for vibration losses in cycling. Several limitations have already been discussed throughout the text and are summarised here for clarity:

- **Simplified pressure dependency:** The model assumes a linear relationship between tire pressure and vibration losses, which does not capture potential non-linear trends, such as the local optimum around 4.0 bar, observed in the interpolated data.
- **Model simplicity:** The model was intentionally kept simple to allow for easier interpretation and application. However, it does not account for variations in rider mass, bicycle setup or road profile, all of which are expected to influence vibration losses.
- **Undefined applicability limits:** The model's range of applicability is not well defined. At very low pressures, tire deformation may become excessive and lead to contact between the rim and the obstacles, altering the vibration loss behaviour. At very high speeds, the rider may lose continuous ground contact and may reduce vibration losses. These conditions fall outside the assumptions of the current formulation and should be considered when applying the model.

4.5. Future work

Following the completion of this project and the insights gained throughout both the experimental and analytical processes, several promising directions for future work have been identified:

- **Improved road surface recreation:** While the road scanning method using photogrammetry has proven effective, the translation of road profiles into artificial excitations with the roughness index matching method remains limited in its ability to replicate real-world spectra. Future designs should incorporate variations in spacing, height, width, and shape of the obstacles to better approximate the power spectral density (PSD) of real road surfaces.
- **Assessment of additional road surfaces:** Expanding the results to include a broader range of road types, such as brick roads or tiles road. This would provide deeper insights into how vibration losses vary under diverse real-world conditions.
- **Redesign of the test setup for constant-speed measurements:** Replacing the coast-down method with a controlled constant-speed setup, such as a rigid-slat treadmill with mounted obstacles, would increase accuracy and data volume. This would eliminate the error introduced by the aerodynamic drag estimation and allow direct study of vibration-related losses under steady conditions. Furthermore, the treadmill surface could eventually be replaced with 3D reproduced sections of scanned road profiles.
- **Exploration of additional influencing parameters:** Variables such as rider body weight, gender and fat-to-muscle ratio influence the human biodynamic response to vibration and merit further investigation. Similarly, bicycle-specific parameters, like tire width, tire type (e.g., gravel or road), or suspension components, should be tested to evaluate their effectiveness in mitigating vibration losses. The role of rider skill and adaptability could also be assessed to determine whether training can reduce vibrational energy losses.
- **Refinement of the vibration loss model:** Building on the initial model proposed in this study, future work should aim to develop a more comprehensive and generalizable formulation. This could include additional parameters such as rider mass, bicycle setup, and detailed road roughness descriptors (e.g., Bicycle Roughness Index, BRI), while also incorporating nonlinear interactions and establishing clear boundaries for model applicability.
- **Further analysis of the recorded dataset:** The inertial data collected from sensors at the contact points and on the rider's body allows for further study. This could include transmissibility analysis, deeper characterization of vibration propagation through the cyclist, or assessments related to rider health and prolonged exposure to vibration.
- **Validation of the method as a low-cost, accessible tool:** Since the final power loss estimates relied primarily on wheel gyroscope data and accelerometer-based stretch segmentation, both of which are available in smartphones, this opens the door for making available to all the vibration loss assessment. Future efforts could test and validate a simplified smartphone-based methodology to make such analyses more accessible to cycling enthusiasts.

5 Conclusion

Energy optimization is a key concern in elite sports, particularly in professional cycling, where reducing power losses directly translates into improved performance. While aerodynamic drag and classical rolling resistance are widely studied, other important contributors, such as vibration-induced power losses, are often overlooked.

Vibrational losses arise from the excitations transmitted through the bicycle and rider when riding over rough surfaces. These losses are commonly lumped together with rolling resistance due to their shared origin: road texture and profile. However, treating them as a single term limits a deeper understanding of vibration-specific phenomena and the variables that influence them. This project aimed to isolate and quantify vibration losses by employing a coast-down method under controlled conditions.

To explore the effect of different parameters on vibration power loss, a test matrix was designed around four key variables: speed, tire pressure, rider posture and rider behaviour. These conditions were systematically crossed and tested over a simulated cobblestone surface to quantify and assess their impact on vibrational losses and their relative contribution to total energy loss.

The results show that vibration-induced losses can be substantial, reaching up to 350 W in some configurations and representing as much as 60% of the total power losses. In most tested conditions, these losses outweighed the aerodynamic and classical rolling resistance contributions individually, highlighting their critical importance in cycling dynamics.

A key finding of this study is that vibration losses cannot be adequately captured by the traditional rolling resistance term, which is typically modeled as linearly dependent on speed. The data revealed a considerably better fit to a quadratic relationship between speed and vibration losses, confirming the hypothesis that a separate, speed-dependent treatment of vibration losses is required. This reinforces the need to reconsider how rolling losses are modeled in order to include the vibration effect.

Tire pressure also showed a strong influence, particularly at higher speeds, where increased pressure led to steeper increases in vibration losses. Rider posture further modulated the outcome: riding off the saddle consistently reduced vibration losses but introduced greater variability in the data.

As an initial step toward a more robust representation of these dynamics, a simple empirical model was proposed. This model assumes a linear dependency on tire pressure, a quadratic dependency on speed, and includes a posture-dependent scaling factor. Despite its simplicity, the model achieved a good fit to the experimental data ($R^2 = 0.883$), offering a valuable approximation of how these variables interact to produce vibration losses. However, its limitations, such as not accounting for different setups or riders, suggest that more advanced modeling approaches should be pursued in future work.

Overall, this study aims to serve both as a motivation and a foundation for deeper investigation into vibration losses in cycling. The results clearly show that these losses are not negligible and that their exclusion from resistance modeling frameworks limits the accuracy of performance predictions. Future work should seek to refine vibration loss models, explore additional influencing parameters, and ultimately integrate these insights into more comprehensive energy optimization strategies.

The take-home message is clear: vibration losses are not negligible and their exclusion from accurate modeling frameworks limits our understanding of energy optimization in cycling. Continued investigation into their mechanisms and mitigation strategies holds promise for performance improvement and technological innovation in the sport.

Bibliography

[1] F. Mutter and T. Pawlowski, “Role models in sports – Can success in professional sports increase the demand for amateur sport participation?” *Sport Management Review*, vol. 17, no. 3, pp. 324–336, Jul. 2014.

[2] ——, “The Causal Effect of Professional Sports on Amateur Sport Participation - An Instrumental Variable Approach,” *International Journal of Sport Finance*, vol. 9, no. 2, pp. 172–188, May 2014.

[3] E. Heinen, B. van Wee, and K. Maat, “Commuting by bicycle: An overview of the literature,” *Transport Reviews*, vol. 30, no. 1, pp. 59–96, Jan. 2010.

[4] M. D. Fenre and A. Klein-Paste, “Bicycle rolling resistance under winter conditions,” *Cold Regions Science and Technology*, vol. 187, p. 103282, Jul. 2021.

[5] E. Fishman, P. Schepers, and C. B. M. Kamphuis, “Dutch cycling: Quantifying the health and related economic benefits,” *American Journal of Public Health*, vol. 105, no. 8, pp. e13–e15, Aug. 2015.

[6] E. Van Der Kruk, F. Van Der Helm, H. Veeger, and A. Schwab, “Power in sports: A literature review on the application, assumptions, and terminology of mechanical power in sport research,” *Journal of Biomechanics*, vol. 79, pp. 1–14, Oct. 2018.

[7] A. C. Lim, E. P. Homestead, A. G. Edwards, T. C. Carver, R. Kram, and W. C. Byrnes, “Measuring changes in aerodynamic/rolling resistances by cycle-mounted power meters,” *Medicine & Science in Sports & Exercise*, vol. 43, no. 5, p. 853, May 2011.

[8] P. E. di Prampero, G. Cortili, P. Mognoni, and F. Saibene, “Equation of motion of a cyclist,” *Journal of Applied Physiology*, vol. 47, no. 1, pp. 201–206, Jul. 1979.

[9] M. D. Fenre and A. Klein-Paste, “Rolling resistance measurements on cycleways using an instrumented bicycle,” *Journal of Cold Regions Engineering*, vol. 35, no. 2, p. 04021001, Jun. 2021.

[10] X. Xie, “Absorbed power as a measure of whole body vehicular vibration exposure,” Master’s thesis, Concordia University, Montreal, Quebec, Canada, Jun. 2001.

[11] S. Rodean and M. Arghir, “Absorbed power as a method to evaluate the health risk of seated occupants exposed to vertical vibration,” *PAMM*, vol. 9, no. 1, pp. 145–146, 2009.

[12] R. Lundström, P. Holmlund, and L. Lindberg, “Absorption of energy during vertical whole-body vibration exposure,” *Journal of Biomechanics*, vol. 31, no. 4, pp. 317–326, Apr. 1998.

[13] D. G. Wilson, T. Schmidt, and J. Papadopoulos, *Bicycling Science*, fourth edition ed. Cambridge, Massachusetts ; London, England: The MIT Press, 2020.

[14] E. W. Faria, D. L. Parker, and I. E. Faria, “The science of cycling: Factors affecting performance – Part 2,” *Sports Medicine*, vol. 35, no. 4, pp. 313–337, Apr. 2005.

[15] T. Nonweiler, “The air resistance of racing cyclists,” *College of Aeronautics, Cranfield*, Oct. 1956.

[16] D. I. Greenwell, N. J. Wood, E. K. L. Bridge, and R. J. Addy, “Aerodynamic characteristics of low-drag bicycle wheels,” *The Aeronautical Journal*, vol. 99, no. 983, pp. 109–120, Mar. 1995.

[17] C. R. Kyle, “Energy and aerodynamics in bicycling,” *Clinics in Sports Medicine*, vol. 13, no. 1, pp. 39–73, Jan. 1994.

[18] R. Karlsson, U. Hammarström, H. Sörensen, and O. Eriksson, *Road Surface Influence on Rolling Resistance: Coastdown Measurements for a Car and an HGV*. Statens väg-och transportforskningsinstitut, 2011.

[19] A. Doria, E. Marconi, L. Munoz, A. Polanco, and D. Suarez, "An experimental-numerical method for the prediction of on-road comfort of city bicycles," *Vehicle System Dynamics*, vol. 59, no. 9, pp. 1376–1396, Sep. 2021.

[20] P. É. Boileau, X. Wu, and S. Rakheja, "Definition of a range of idealized values to characterize seated body biodynamic response under vertical vibration," *Journal of Sound and Vibration*, vol. 215, no. 4, pp. 841–862, Aug. 1998.

[21] SRAM, "Total System Efficiency™: Making You Faster," SRAM, Technical Document, 2024.

[22] M. M. Turner, "Cycling on rough roads: A model for resistance and vibration," *Vehicle System Dynamics*, vol. 62, no. 10, pp. 2729–2749, Oct. 2024.

[23] J. Thibault and Y. Champoux, "Rider influence on modal properties of bicycle frames," *Canadian Acoustics*, vol. 28, no. 3, pp. 44–45, Sep. 2000.

[24] C. Hölzel, F. Höchtl, and V. Senner, "Cycling comfort on different road surfaces," *Procedia Engineering*, vol. 34, pp. 479–484, 2012.

[25] M. J. Griffin, *Handbook of Human Vibration*. Academic Press, Dec. 2012.

[26] R. A. Lee and F. Pradko, "Analytical analysis of human vibration," *SAE Transactions*, vol. 77, pp. 346–370, 1968.

[27] F. Pradko, R. A. Lee, F. Pradko, and R. A. Lee, "Vibration comfort criteria," in *1966 Automotive Engineering Congress and Exposition*. SAE International, Feb. 1966.

[28] C. W. Suggs, C. F. Abrams, and L. F. Stikeleather, "Application of a damped spring-mass human vibration simulator in vibration testing of vehicle seats," *Ergonomics*, vol. 12, no. 1, pp. 79–90, Jan. 1969.

[29] C.-C. Liang and C.-F. Chiang, "A study on biodynamic models of seated human subjects exposed to vertical vibration," *International Journal of Industrial Ergonomics*, vol. 36, no. 10, pp. 869–890, Oct. 2006.

[30] J. Vanwalleghem, I. De Baere, M. Loccufier, and W. Van Paepegem, "Sensor design for outdoor racing bicycle field testing for human vibration comfort evaluation," *Measurement Science and Technology*, vol. 24, no. 9, p. 095002, Sep. 2013.

[31] R. R. Coermann, "The mechanical impedance of the human body in sitting and standing position at low frequencies," *Human Factors: The Journal of the Human Factors and Ergonomics Society*, vol. 4, no. 5, pp. 227–253, Oct. 1962.

[32] N. Mansfield and M. Griffin, "Effect of magnitude of vertical whole-body vibration on absorbed poewwr for the seated human body," *Journal of Sound and Vibration*, vol. 215, no. 4, pp. 813–825, Aug. 1998.

[33] N. Nawayseh and M. J. Griffin, "Power absorbed during whole-body vertical vibration: Effects of sitting posture, backrest, and footrest," *Journal of Sound and Vibration*, vol. 329, no. 14, pp. 2928–2938, Jul. 2010.

[34] W. Wang, S. Rakheja, and P. É. Boileau, "Effects of sitting postures on biodynamic response of seated occupants under vertical vibration," *International Journal of Industrial Ergonomics*, vol. 34, no. 4, pp. 289–306, Oct. 2004.

[35] J. Lépine, Y. Champoux, and J.-M. Drouet, "Road bike comfort: On the measurement of vibrations induced to cyclist," *Sports Engineering*, vol. 17, no. 2, pp. 113–122, Jun. 2014.

[36] ——, “A laboratory excitation technique to test road bike vibration transmission,” *Experimental Techniques*, vol. 40, no. 1, pp. 227–234, Feb. 2016.

[37] J.-P. Pelland-Leblanc, J. Lépine, Y. Champoux, and J.-M. Drouet, “Using power as a metric to quantify vibration transmitted to the cyclist,” *Procedia Engineering*, vol. 72, pp. 392–397, 2014.

[38] ——, “Effect of structural damping on vibrations transmitted to road cyclists,” in *Conference Proceedings of the Society for Experimental Mechanics Series*, vol. 7, 2014, pp. 283–290.

[39] J. Vanwalleghem, F. Mortier, I. De Baere, M. Loccufier, and W. Van Paepegem, “Design of an instrumented bicycle for the evaluation of bicycle dynamics and its relation with the cyclist’s comfort,” *Procedia Engineering*, vol. 34, pp. 485–490, Jan. 2012.

[40] J. Heine, “The Missing Link: Suspension Losses,” https://www.renehersecycles.com/the-missing-link-suspension-losses/, 2009.

[41] C. G. Thigpen, H. Li, S. L. Handy, and J. Harvey, “Modeling the impact of pavement roughness on bicycle ride quality,” *Transportation Research Record: Journal of the Transportation Research Board*, vol. 2520, no. 1, pp. 67–77, Jan. 2015.

[42] P. Andren, “Power spectral density approximations of longitudinal road profiles,” *International Journal of Vehicle Design*, vol. 40, no. 1-3, pp. 2–14, Jan. 2006.

[43] R. Evans, “Identifying Waveband Roughness in Highway Pavements using Power Spectral Density Analysis,” May 2015.

[44] M. W. Sayers, “On the calculation of International Roughness Index from longitudinal road profile,” *Transportation Research Record*, no. 1501, 1995.

[45] K. Tomiyama, K. Takahasi, K. Tachibana, T. Akeda, and T. Hagiwara, “A concept of surface roughness index for cycle path: Bicycle Ride Index (BRI),” in *Proceedings of the 10th International Conference on Maintenance and Rehabilitation of Pavements*, P. Pereira and J. Pais, Eds. Cham: Springer Nature Switzerland, 2024, pp. 67–76.

[46] R. B. Candau, F. Grappe, M. Ménard, B. Barbier, G. Y. Millet, M. D. Hoffman, A. R. Belli, and J. D. Rouillon, “Simplified deceleration method for assessment of resistive forces in cycling,” *Medicine & Science in Sports & Exercise*, vol. 31, no. 10, p. 1441, Oct. 1999.

[47] S. Tengattini and A. Bigazzi, “Validation of an outdoor coast-down test to measure bicycle resistance parameters,” *Journal of Transportation Engineering, Part A: Systems*, vol. 144, no. 7, p. 04018031, Jul. 2018.

[48] J. D. Garrett, “Garrettj403/SciencePlots,” Sep. 2021.

[49] “ISO 2631-1: Mechanical vibration and shock — Evaluation of human exposure to whole-body vibration - Part 1: General requierements,” https://www.iso.org/standard/7612.html, 1997.

[50] Society of Automotive Engineers, “Vehicle Dynamics Terminology,” SAE, Tech. Rep. J670, 2008.

[51] J. K. Moore, J. Koshy Cherian, B. Andersson, O. Lee, and A. Ranheim, “Modeling and Implementation of a Reaction Wheel Stabilization System for Low Speed Balance of a Cargo Bicycle,” *The Evolving Scholar*, 2023.

[52] M. Sarstedt and E. Mooi, “Regression Analysis,” in *A Concise Guide to Market Research: The Process, Data, and Methods Using IBM SPSS Statistics*, M. Sarstedt and E. Mooi, Eds. Berlin, Heidelberg: Springer, 2019, pp. 209–256.

[53] A. Gupta, T. S. Stead, and L. Ganti, “Determining a Meaningful R-squared Value in Clinical Medicine,” *Academic Medicine & Surgery*, Oct. 2024.

[54] H. Akaike, “Akaike’s Information Criterion,” in *International Encyclopedia of Statistical Science*. Springer, Berlin, Heidelberg, 2025, pp. 41–42.

[55] M. Prosser-Contreras, E. Atencio, F. Muñoz La Rivera, and R. F. Herrera, “Use of Unmanned Aerial Vehicles (UAVs) and Photogrammetry to Obtain the International Roughness Index (IRI) on Roads,” *Applied Sciences*, vol. 10, no. 24, p. 8788, Jan. 2020.

[56] Z. Svatý, P. Vrtal, R. Shults, T. Kohout, L. Nouzovský, T. Blodek, and K. Kocián, “Photogrammetric approach to detect road pavement friction,” *PLOS ONE*, vol. 20, no. 2, p. e0318188, Feb. 2025.

[57] C. Griwodz, S. Gasparini, L. Calvet, P. Gurdjos, F. Castan, B. Maujean, G. De Lillo, and Y. Lanthony, “AliceVision Meshroom: An open-source 3D reconstruction pipeline,” in *Proceedings of the 12th ACM Multimedia Systems Conference*, ser. MMSys ’21. New York, NY, USA: Association for Computing Machinery, Sep. 2021, pp. 241–247.

[58] P. Cignoni, M. Callieri, M. Corsini, M. Dellepiane, F. Ganovelli, and G. Ranzuglia, *MeshLab: an Open-Source Mesh Processing Tool*. The Eurographics Association, 2008.

[59] D. G. Alciatore and M. B. Histand, *Introduction to Mechatronics and Measurement Systems*, 4th ed., ser. Connect, Learn, Succeed. New York: McGraw-Hill, 2012.

A

IMU mounts - CAD Design

A.1. Handlebar mount

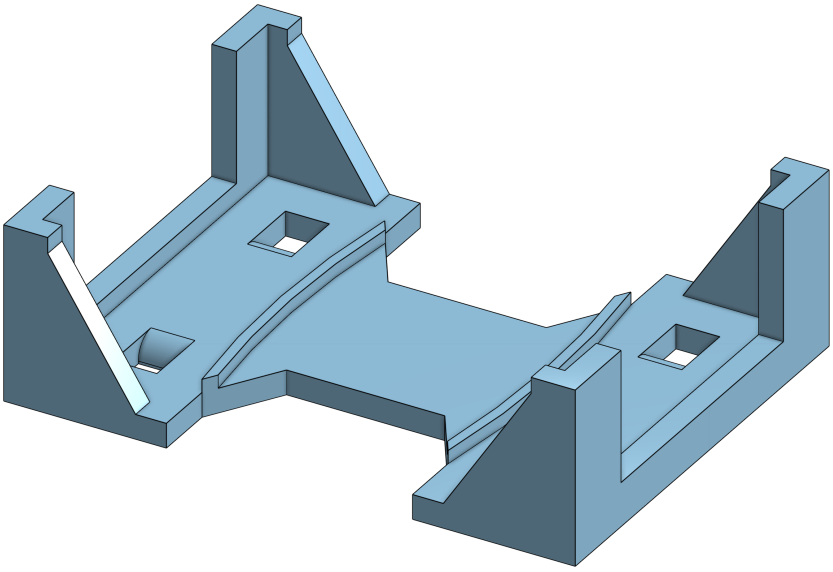

Figure A.1: Isometric view of the mount designed to hold the IMU on the handlebar.

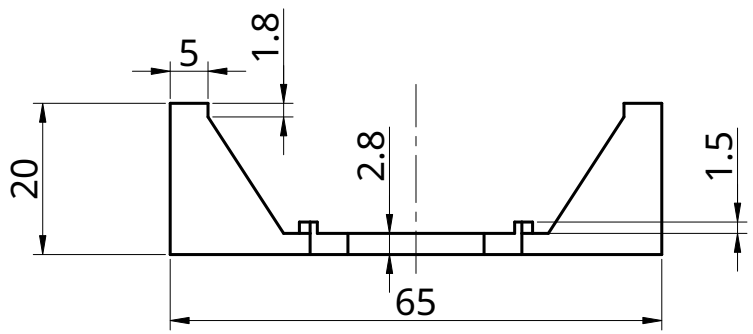

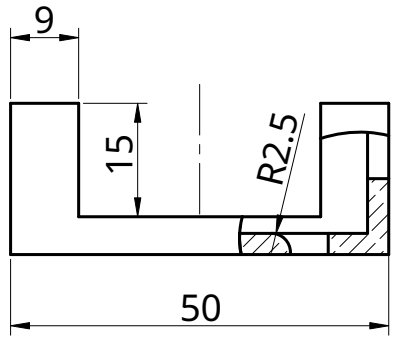

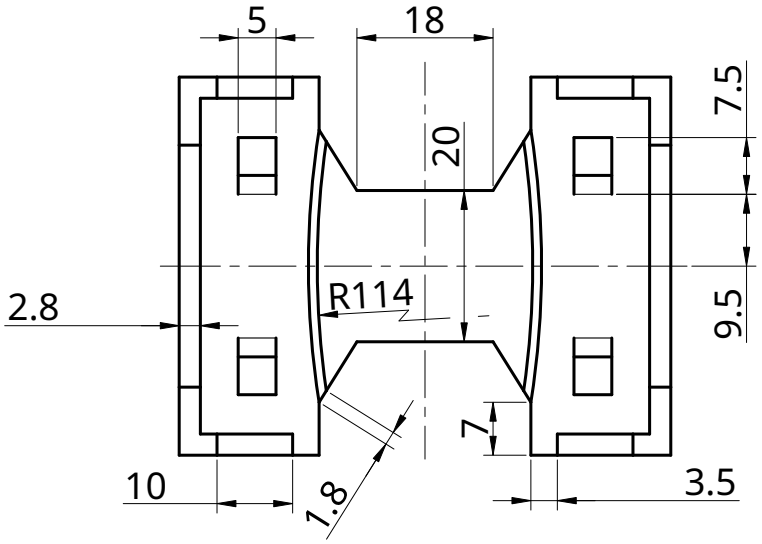

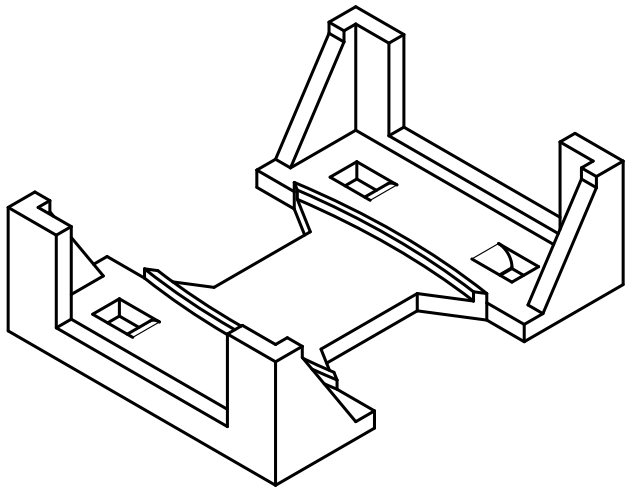

UNLESS OTHERWISE SPECIFIED, DIMENSIONS ARE IN MILLIMETERS		NAME	SIGNATURE	DATE
	DRAWN	ELOY VAZQUEZ		2025-05-30
	CHECKED			
	APPROVED			

FIRST ANGLE PROJECTION

MATERIAL

FINISH

TITLE

Handlebar stem mount

SIZE A4

DWG NO.

REV.

SCALE 1:1

WEIGHT

SHEET 1 of 1

A.2. Seatpost mount

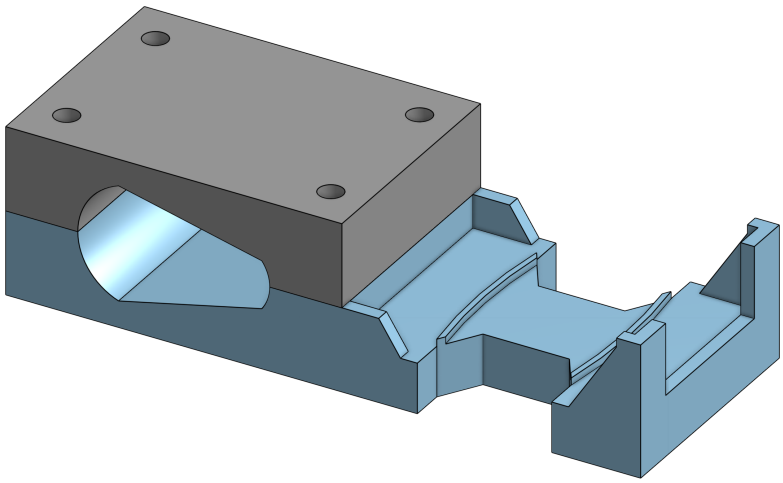

Figure A.2: Isometric view of the mount designed to hold the IMU on the seatpost.

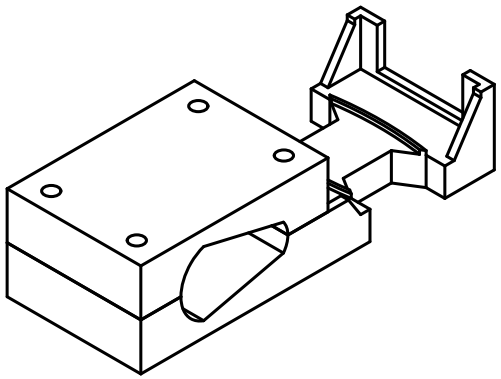

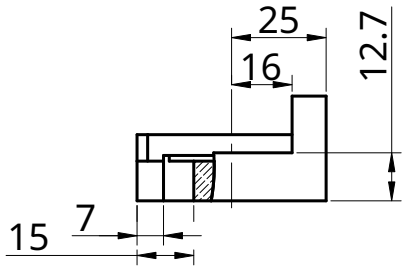

Part A

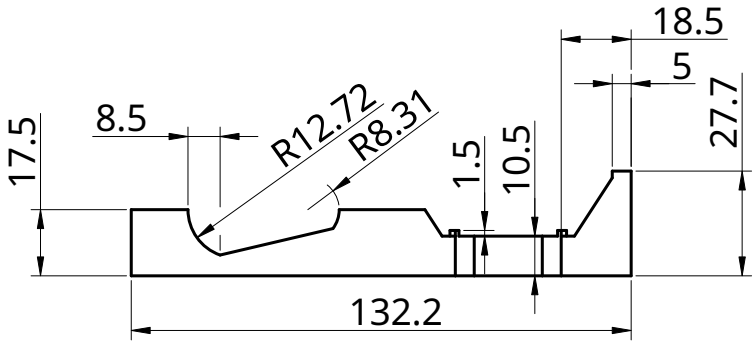

Part B

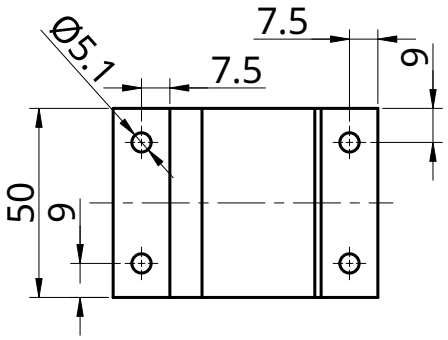

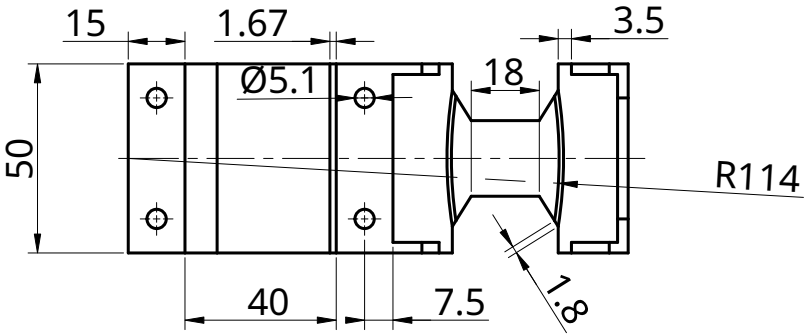

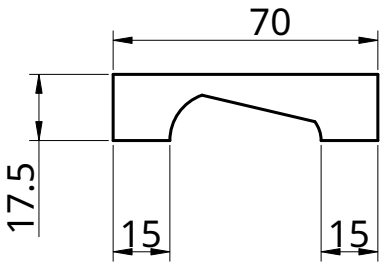

UNLESS OTHERWISE SPECIFIED, DIMENSIONS ARE IN MILLIMETERS		NAME	SIGNATURE	DATE
	DRAWN	ELOY VAZQUEZ		2025-05-30
	CHECKED			
	APPROVED			

FIRST ANGLE PROJECTION

MATERIAL

FINISH

TITLE

Seatpost mount
(two parts)

SIZE A4

DWG NO.

REV.

SCALE 1:2

WEIGHT

SHEET 1 of 1

A.3. Wheel mount

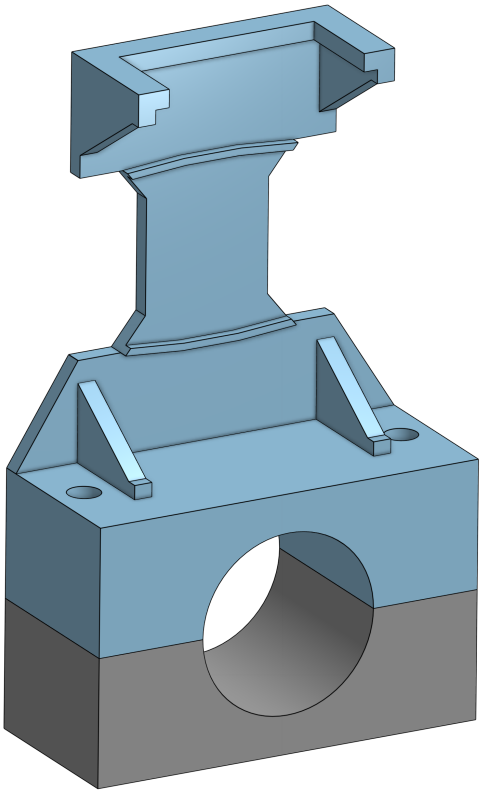

Figure A.3: Isometric view of the mount designed to hold the IMU on the wheel.

Part A

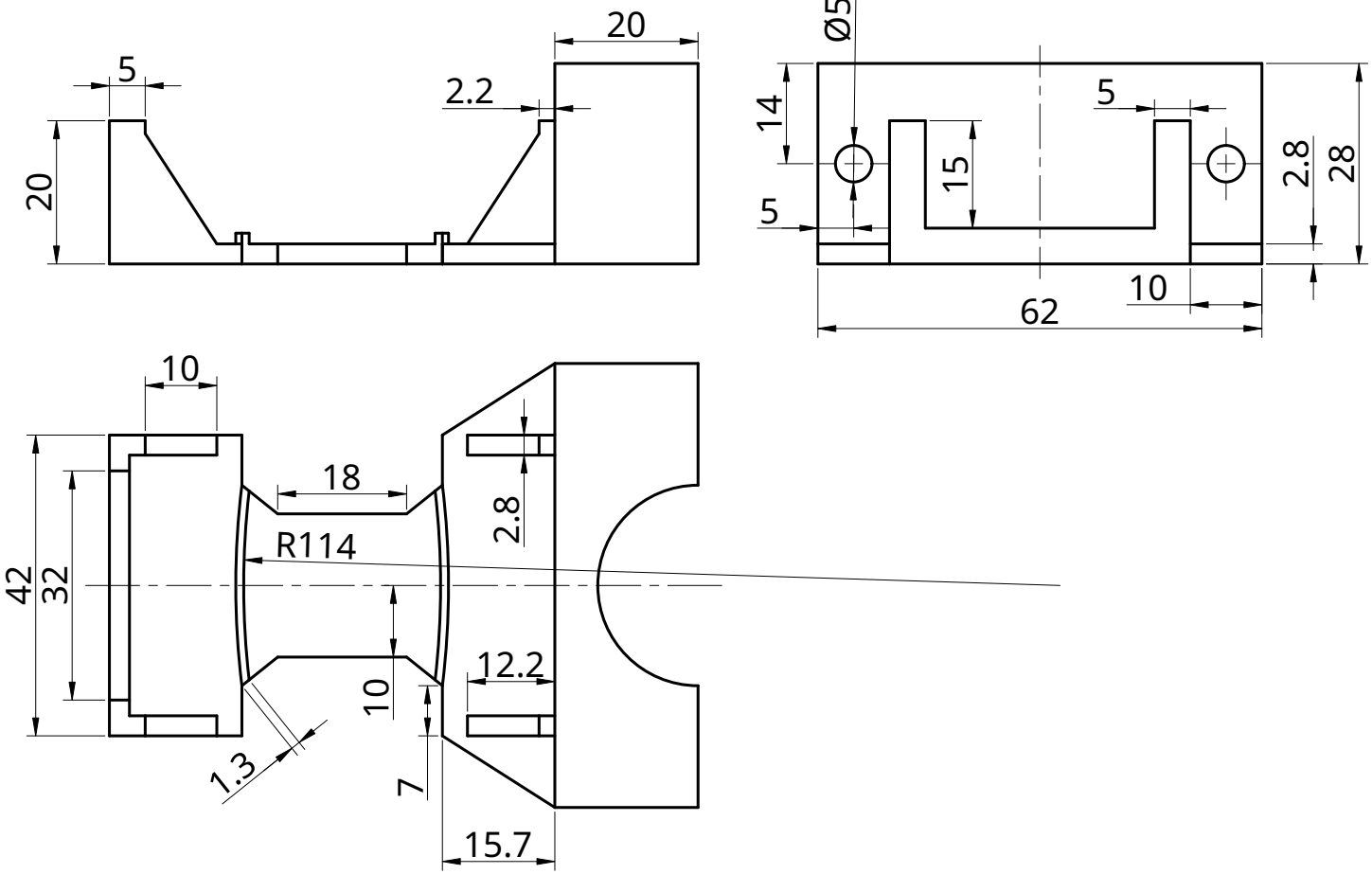

Part B

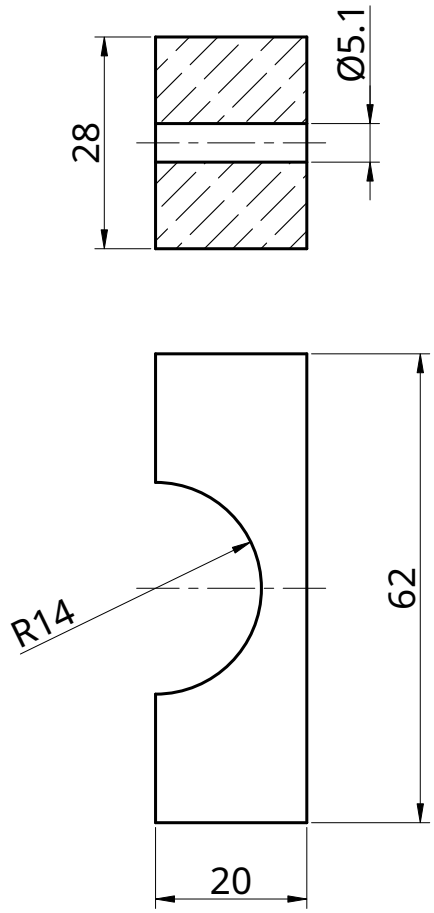

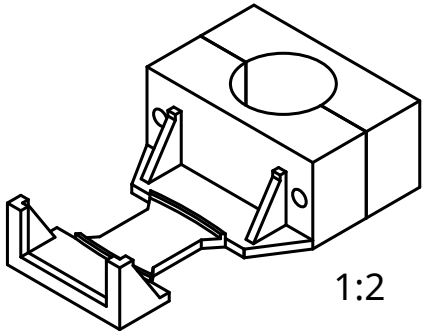

1:2

UNLESS OTHERWISE SPECIFIED, DIMENSIONS ARE IN MILLIMETERS		NAME	SIGNATURE	DATE
	DRAWN	ELOY VAZQUEZ		2025-05-30
	CHECKED			
	APPROVED			
FIRST ANGLE PROJECTION	MATERIAL		FINISH	

TITLE

Wheel hub mount
(two parts)

SIZE	DWG NO.	REV.
A4		

SCALE	WEIGHT	SHEET
1:1		1 of 1

B

Bicycle Parameters

Table B.1: Bicycle properties and equipment used.

Model	Giant TCR Andvanced 2012
Rims	Shimano Dura-Ace C24 622×15C (aluminum)
Tires	Vittoria Randonneur 700×28C
Bicycle weight	8.05 kg
Wheelbase	0.99 m
Wheel radius	0.34 m

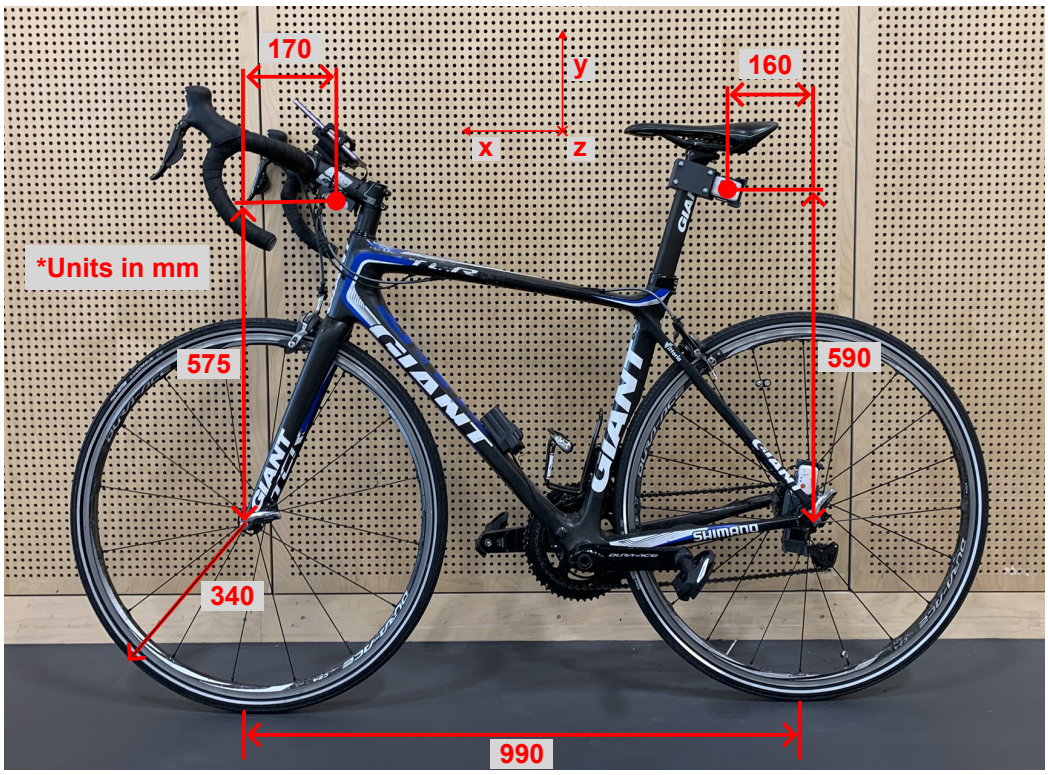

Figure B.1: Dimensions of the bicycle and the placement of the IMUs.

C

Road Characterization

As the objective of the experiment is to study the vibrations caused by the road surface, replicating these excitations in a control environment requires from a certain knowledge on the roads to replicate. Therefore, a method to recreate this road inputs is described. Starting from obtaining data from the roads of interest and then labeling them with an index that characterizes the features of interest for the vibrations on cycling.

C.1. Photogrammetry: road scanning

Up to now, the road maintenance and civil engineering industry has been doing great efforts to improve the roads infrastructure and condition. Lately, some techniques to assess the condition of the pavements have been used and researched. One of this is the use of photogrammetry as a tool to scan the roads. For this, Unmanned Aerial Vehicles (UAVs) has been used and proved their capability to assess the roughness of the pavement with a very high accuracy defining the International Roughness Index [55]. However, this index is based on larger wavelenghts, from 0.5m to 50m [41], dismissing very important features that are relevant for the bicycle beahaviour regarding the vibrations experienced [45]. However, recently Svatý et al 2025 [56], proved that the photogrammetry is a suitable and accurate tool for assessing the pavement surface, scanning up to the macrotexture, with wavelengths ranging from 0.5mm to 50mm. While the interesting range according to Tomiyama 2024 [45] is for the megatexture, ranging from 50mm to 0.5m wavelenghts.

Knowing this, the application of this technique, would allow for a accurate enough description of the profile for the application in cycling vibrations. Therefore, the procedure followed during this project is described, with detail on the software used and the equipment used to obtain the profiles database to a further classification according to its roughness.

Scaning procedure

For the scanning of the surface, the first step followed is the preparation of the area selected to photograph, this means having it clear, without any leaves, stones, or any kind of object that doesn't belong to the surface and that can affect the profile scanned. Must be noted that certain stains or distinguishable features on the pavement will help the software find the features needed to overlay the different photos and build the 3D scan.

A section of 1x1.5 meters was selected to photograph. This includes the maximum wavelenght of the interested range for the megatexture of 0.5m. This area was delimited on the corners by marking on the ground with chalk, having a different shape on each corner for easy feature recognision. Furthermore, a metric tape was placed along one of the long sides of the rectangle. This will serve for scaling the model created later to the real dimensions.

Once with the area prepared, a decent amount of pictures of the floor had to be taken from multiple angles. For this, the pattern followed was in circles around the center in different heights first, and then a sweep of pictures, similarly to what shown on Figure C.1. Lastly, a set of close look photos of the metric tape were taken to get a higher resolution of the numbers and lines engraved on the tape.

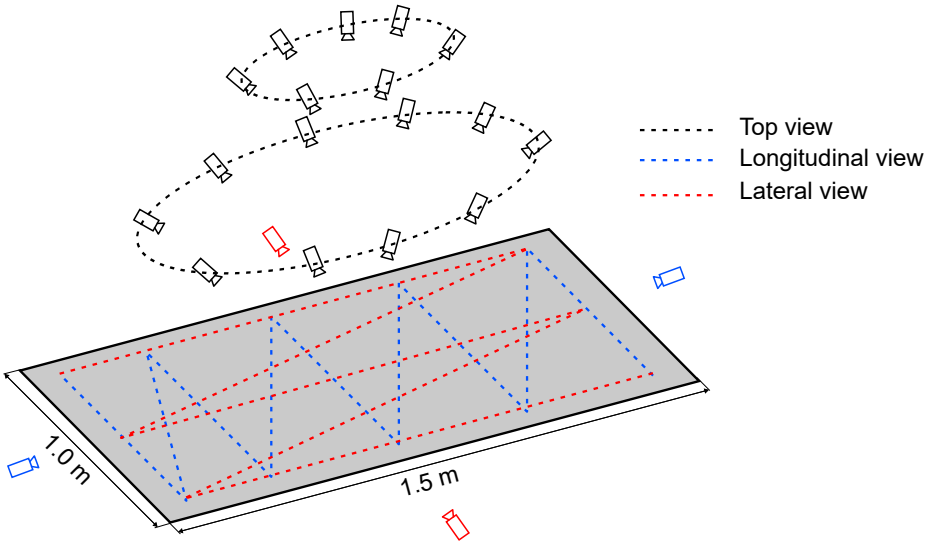

Figure C.1: Pattern used to take the pictures for the 3D scan.

Photogrammetry rendering

Once the photos are taken, they are introduced into the open-source software Meshroom (AliceVision [57]). Once that made, it was created a folder with the project and save there the '.mg' project. With the default settings, start the process.

Whenever is finished, as in Figure C.2, some adaptations to files have to be done. For that, in the folder created, it will appear a new folder 'MeshroomCache', following the directory 'MeshroomCache/Texturing' a folder with the reference of the texturing settings will appear and the files named with the '.exr' extension must be converted to '.png'. For this purpose, an online tool was used[1]. Once this file is converted, it has to be introduced the '.png' in the same directory, and the file '.mtl' should be modified to include the '.png' files instead of the '.exr'.

Mesh processing

After getting the 3D scan from the photogrammetry, the output of it, the 3D object has to be scaled, cropped to the area of interest, and improved the mesh. For this, in the folder created, under 'MeshroomCache/Texturing' a '.obj' file that can be imported as a mesh in a dedicated software for this adjustments. In this case, it was used MeshLab (Visual Computing Lab [58]).

After importing the mesh ('.obj' file), with the right textures, the first step is to scale the mesh. For this, the measuring tape used on the pictures must be recognized and search for numbers that with an accurate enough resolution for getting the mesh scale and compare to the real scale. The scaling factor would be d_{real}/d_{mesh}, being both expressed in millimeters. This scaling factor has to be introduced in the scaling tool, located under 'Filters/Normals, Curvatures and Orientation/Transform:Scale, Normalize'. The number has to be introduced in the X-Axis box and make sure the Uniform Scaling box is ticked. Under 'View/Reset_Trackball' the road can be seen again in the screen. After this, the texture can be disabled since is not needed anymore and only the mesh is needed.

Now to orient the profile and make it horizontal to the XY plane, the Z-painting tool, red brush, is used to paint the main area of interest to be horizontal. When this is selected, on 'Filters/Normals, Curvatures and Orientation/Transform: Rotate to Fit to a plane' tool is used. It might be that the result orientation is upside down, for that the tool 'Filters/Normals, Curvatures and Orientation/Transform: Rotate' is used indicating 180deg. After this the selection of the plane, made with the brush, can be deselected, with Ctrl+Shift+D.

Now with the tool 'Select Faces/Vertices inside polyline area' the area of interest in which the pictures were focused and details of the mesh can be appreciated, can be selected by selecting the vertices of the area. After this, the area has to be added 'Q' and invert the selection 'I'. Using 'Delete Selected

[1]Several options are available. The tool used in this project is `https://image.online-convert.com/convert/exr-to-png`, though simple Python scripts such as `https://github.com/pjessesco/exr_to_png` can also perform the conversion.

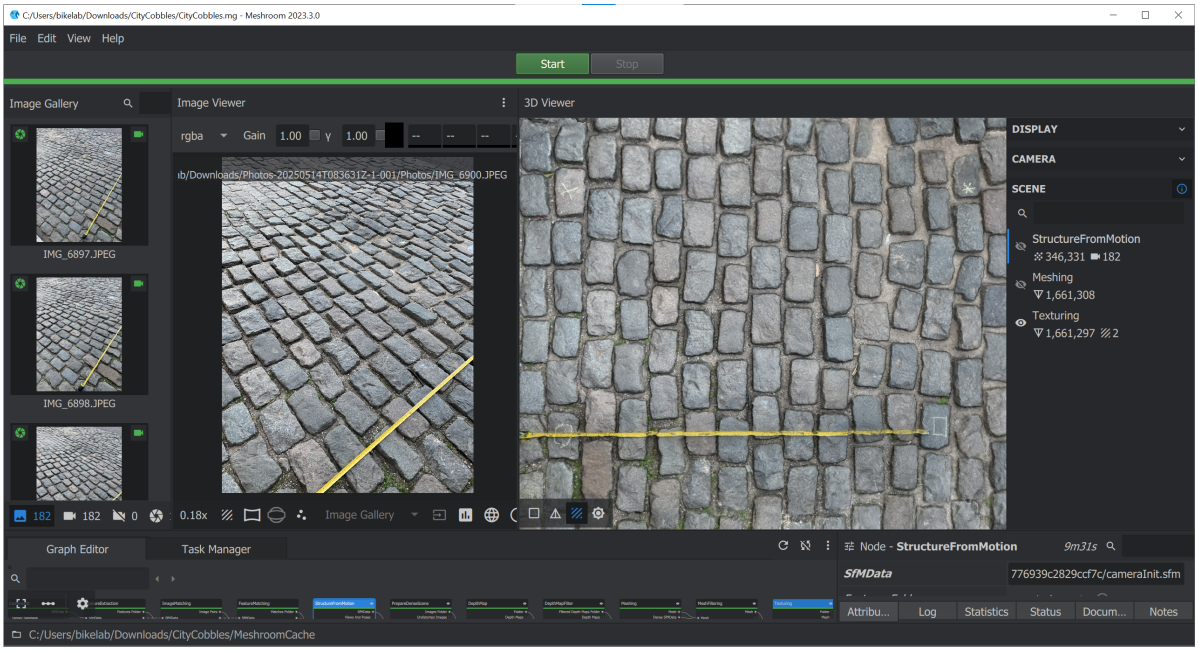

Figure C.2: Screenshot of the photogrammetry process to scan the road profile. Software: Meshroom [57].

Faces and Vertices', the interesting area would be remaining.

After this, there is only one thing left, filtering the mesh in search for incoherence and problematic points. For this, a list of filters that can be found in 'Filters/Cleaning and Repairing' are applied in the following order:

- Remove Isolated pieces (wrt Diameter),
- Remove Duplicated Faces,
- Remove Duplicated Vertices,
- Remove Unreferenced Vertices,
- Remove Zero Area Faces,
- Repair non Manifold Edges.

All of them with the default settings, works good enough. A example of how the final process looks like in the software is seen in Figure C.3.

The mesh is exported back as a '.obj' file with all boxes selected for the textures. Furthermore, the mesh has to be exported in '.xyz' format, which will be the one used in the script to get the road roughness index that characterizes the scanned road.

C.2. Roughness index calculation

To characterize the road surface, a roughness index-based method was employed. While the commonly used International Roughness Index (IRI) is based on a quarter-car model with standard 'Golden Car' parameters, it is designed for motor vehicles and includes signal filtering not suitable for lightweight, human-powered vehicles such as bicycles [44]. To address this, the Bicycle Roughness Index (BRI), proposed by Tomiyama [45], was adopted. The BRI modifies the quarter-car model to better reflect the dynamics and frequency response of a bicycle–rider system, capturing the relevant excitation wavelengths.

To obtain the BRI of a real surface, the 3D profile of the road was captured via photogrammetry and exported in '.xyz' format. This point cloud was then processed using a custom Python script that:

- Verified the horizontal orientation of the surface. If needed, the mesh was rotated using its plane normal to align it with the global vertical axis.

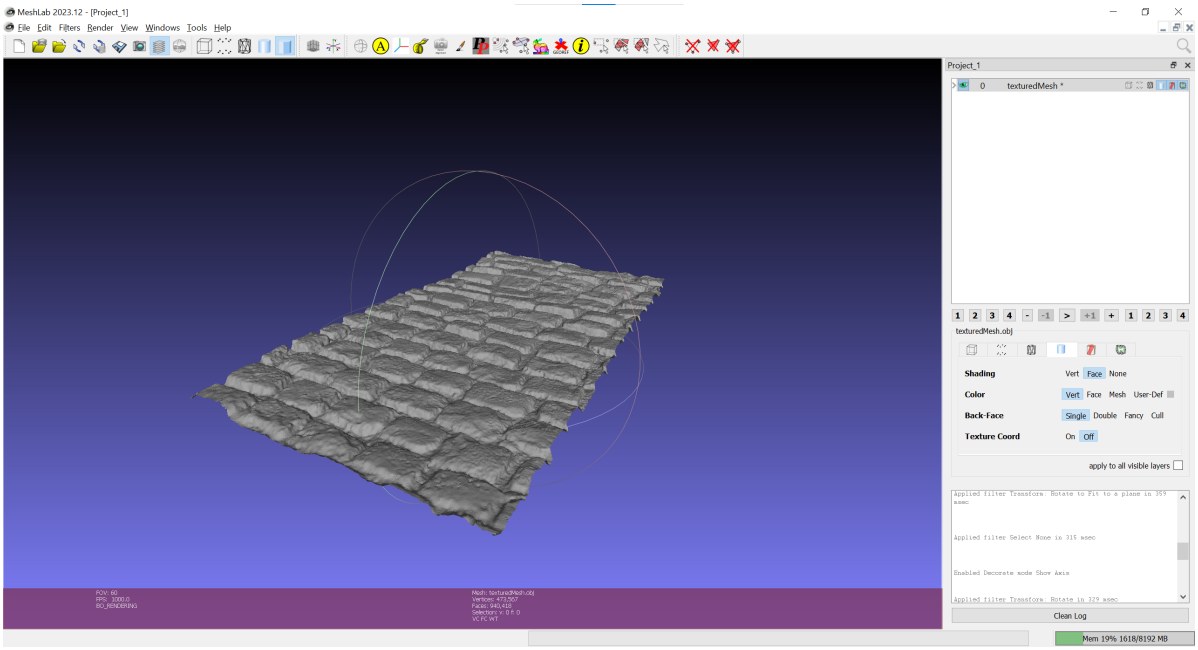

Figure C.3: Screenshot of the mesh editing process for getting the road profile. Software: Meshlab [58].

- Extracted 15 longitudinal profiles at evenly spaced approach angles across the scanned area.

The extracted profiles were derived from the point cloud, see Figure C.4, which lacks uniform spatial resolution. To standardize the data, each profile was resampled to have one point every 5 mm, based on the mesh's average resolution of approximately 2.4 mm. This ensures that features relevant to macrotexture and megatexture (50–500 mm wavelength) are preserved in the input. Although the IRI method applies a 25 cm moving average filter (removing wavelengths below 4 m^{-1}), the BRI model does not require such filtering. According to the gain plots shown in Figure C.5, a 5 mm sampling density (corresponding to 200 m^{-1}) captures all relevant information for BRI computation and could be relaxed to 25 mm (40 m^{-1}) without losing fidelity.

Each resampled longitudinal profile served as input to the BRI quarter-car model (described in Section 2.1.3). For each profile, the model was simulated at a defined testing speed, rather than the standard 15 km/h. This produced a 'Pseudo-BRI' specific to that velocity. The state vector outputs, specifically the sprung and unsprung masses displacements, z_s and z_u respectively, were used to compute relative displacement and accumulate it over time.

Since the model does not include the rolling dynamics of the wheel–ground interaction, the transient response is longer than in real-life scenarios. To ensure accurate BRI estimation and minimize the effect of these transients, each scanned longitudinal profile was artificially extended to a total length of 100 m before simulation. The final BRI for each surface was calculated as the average across all 15 profiles.

C.2.1. Artificial Profile Design Based on Pseudo-BRI Matching

Once the Pseudo-BRI of the reference cobblestone surface was calculated at each target speed (10–30 km/h), it served as a reference for the design of artificial profiles.

Artificial profiles were constructed using rectangular wooden planks of fixed height (20mm) and width (90mm), placed at varying spacings along the bicycle path. The spacing between the planks was optimized by simulating the quarter-car model response to each spacing configuration and computing the resulting Pseudo-BRI.

The configuration that most closely matched the reference cobblestone surface's Pseudo-BRI at each speed was selected. Special care was taken to avoid spacings that could generate undesirable resonances (e.g., near the 5 Hz resonance of the human body) or align with the bicycle wheelbase.

The final spacing configurations used during testing are reported in Table 2.2, and the complete set of spacing simulations considered is detailed in Appendix C.3.

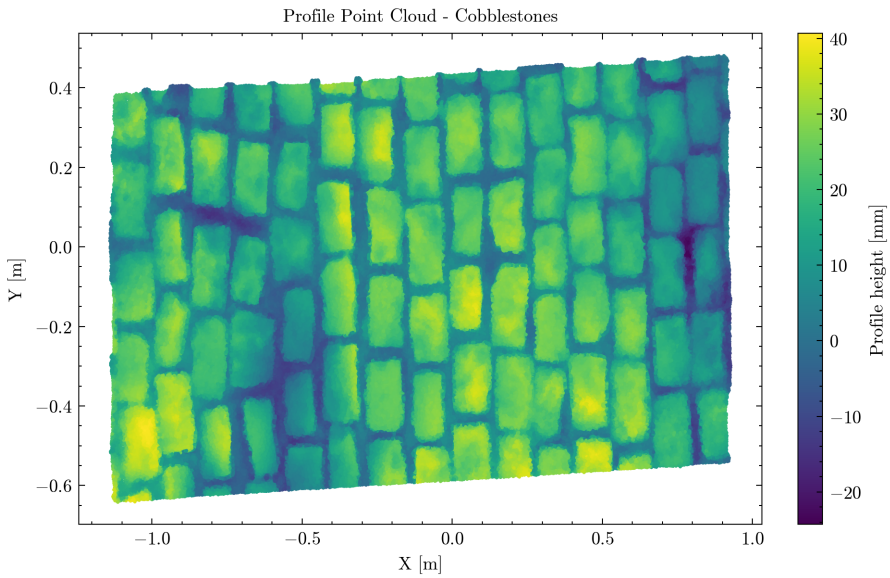

Figure C.4: Point cloud for the cobbles section.

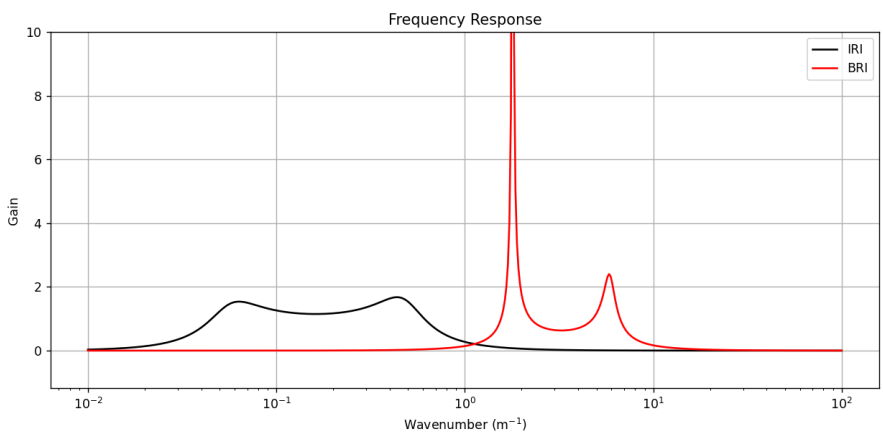

Figure C.5: Transfer funtion gains of each roughness model, reflecting the wavenumbers capable of capture.

C.3. Plank spacing configuration options

Speed (km/h)	Reference Pseudo-BRI	Spacing (m)	Simulated Pseudo-BRI
10	341.6	0.24	332.3
		0.73	341.7
15	257.1	0.15	250.0
		0.21	253.9
		0.37	254.2
		0.54	266.1
		1.69	255.5
20	196.9	0.27	196.6
		0.48	206.7
		0.73	203.1
		1.48	193.8
25	117.4	0.23	109.5
		0.35	109.2
		0.52	111.0
		0.53	124.1
		0.62	115.8
		0.83	111.3
		0.84	115.6
		0.85	118.8
		0.86	119.1
		0.87	118.1
		0.88	116.0
		0.89	114.3
		0.90	118.1
30	125.6	0.3	122.0
		0.39	120.7
		0.67	122.3
		0.68	127.1
		0.69	126.5
		0.70	121.8

Table C.1: Simulated Pseudo-BRI values for various artificial surface configurations and comparison with the reference Pseudo-BRI of the real cobblestone profile at each speed.

D

Road Database

D.1. Cobbles Section

The section here described, was the one that was simulated for the experiments described on this project. This section is located at Zuiderstraat 128-4, Delft, The Netherlands (GPS coordinates: 52.009564, 4.365134). To characterize the surface, 182 photographs were used to obtain a BRI of 257.1. The surface can be seen in Figure D.1.

Figure D.1: Section of road used to simulate on the experiments.

D.2. Brick road

As a comparison on the state of the road, a new brick road and an old one have been analysed. First, the new road with bricks of 10x20cm was scanned using 271 photos, resulting into a BRI of 38.0. This section was located at Mekelweg 2, 2628 CD Delft, The Netherlands (GPS coordinates: 52.000590, 4.371581), Photographs of the surface can be seen in Figure D.2.

Figure D.2: New brick roads section.

As a old brick road, the location chosen was at Mekelweg 2, 2628 CD Delft, The Netherlands (GPS coordinates: 52.001068, 4.372323). This profile with 7x20 cm bricks yielded with a set of 204 phots a BRI profile index of 46.1. Images of the surface can be seen in Figure D.3

Figure D.3: Old brick roads section.

Testing area

The TUDelft Mechanical Engineering faculty has a testing area at Leeghwaterstraat 39, 2628 CB Delft, The Netherlands. Here, two different types of road surfaces were also analyzed. A zone of this area is made out of bricks (coordinates: 51.999230, 4.370630). Using 129 photos, a BRI of 41.4 was identified. This surface can be seen in Figure D.4.

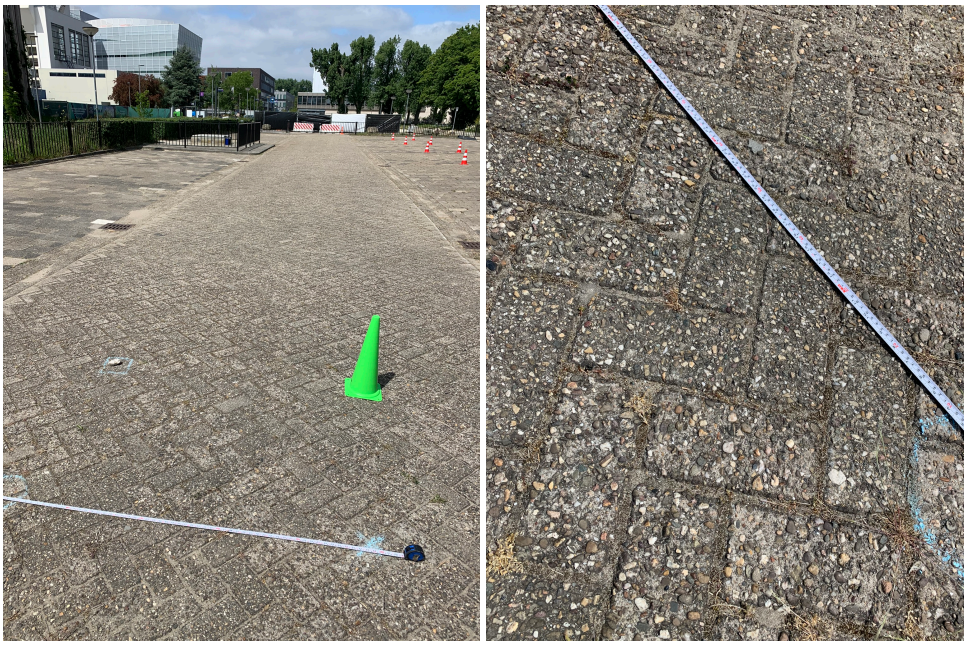

Figure D.4: Testing area, bricks section.

The other surface type on this testing area is made of 30x30 cm tiles (coordinates: 51.999262, 4.370686). The profile obtained used 174 photos, but a error in the mesh made not possible to compute the BRI. Therefore, if this surfaces is desired to be computed, the scan should be repeated. The surface can be seen in Figure D.5

Figure D.5: Testing area, tiles section.

Rumbles

As an extra example of a rough surface that is intended to be such is the rumble strips present between the cycling path and the footpath. This section was observed at Mekelweg 2, 2628 CD Delft, The Netherlands (coordinates: 52.001049, 4.372686). For scanning this roughness, 249 pictures were used, leading to a BRI of 75.8. This surface can be seen in Figure D.6.

Figure D.6: Cycling path rumble strips.

E

Preliminary Tests

For experimenting with the bicycle and taking conclusions it is vital to make sure some points are clear on the procedure and taking into account different matters that could influence the results. For this, the here called preliminary tests were carried out, to find out the implications of different matters to the results obtained or even to the testing set-up.

E.1. Resonance

To ensure reliable vibration measurements, it was necessary to verify that the accelerometer mounts did not introduce artifacts due to mechanical resonance. If the excitation frequencies of interest align with the natural frequencies of the mounting system, signal amplification may occur, distorting the results. To evaluate this, each accelerometer was installed on its respective bicycle component (stem or seatpost) using the designed mounts (see Appendix A), and the assemblies were removed from the bike. They were then rigidly clamped in a bench vise, as shown in Figure E.1. This setup allowed for isolation and characterization of any resonant behavior originating from the sensor mounting configurations.

Description of the test

The resonance test involved applying an impulse excitation to the accelerometer and its mounting assembly using a rubber hammer. This method excites all the frequencies of the system. The resulting ac-

(a) Seatpost sensor.

(b) Handlebar sensor.

Figure E.1: IMUs and mountings clamped for the resonance test.

celeration response was recorded to identify the natural (resonant) frequencies of the sensor-mounting configuration.

Each accelerometer remained fixed to the corresponding bicycle part (carbon fiber seatpost or forged aluminum stem), and the entire assembly was clamped firmly in a bench vise. Due to the inherent stiffness of these base components, particularly the aluminum stem and carbon post, they were assumed to have natural frequencies well above the range of interest. Therefore, any observed resonances in the recorded data were attributed to the accelerometer mountings themselves, i.e. the 3D-printed plastic brackets and the inertial measurement unit (IMU) couplings.

To improve accuracy and reliability, multiple impulses were produced for each mounting configuration, with impacts applied in various directions to excite different modes of vibration. The acceleration signals were processed using Fast Fourier Transform (FFT) analysis, and gravitational components (typically at 1 Hz) were removed via high-pass filtering to isolate dynamic response characteristics.

Results

When the vibration responses were analyzed in the frequency domain, the resulting spectra for each sensor axis, shown in Figures E.2a and E.2b, revealed distinct resonance peaks corresponding to the mounting configurations. The identified resonance frequencies for both the seatpost and handle-

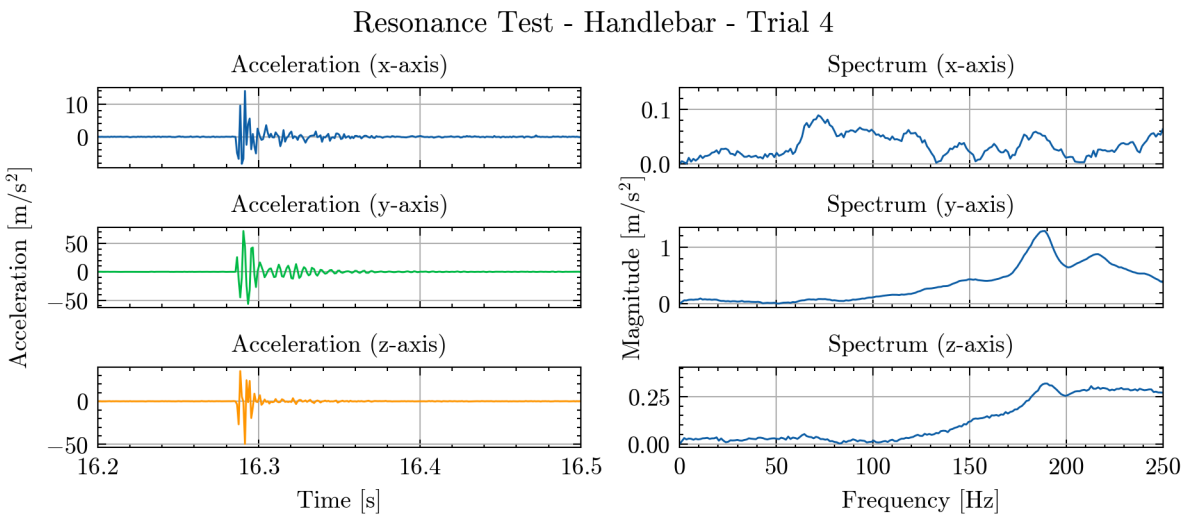

(a) Response of the handlebar's IMU.

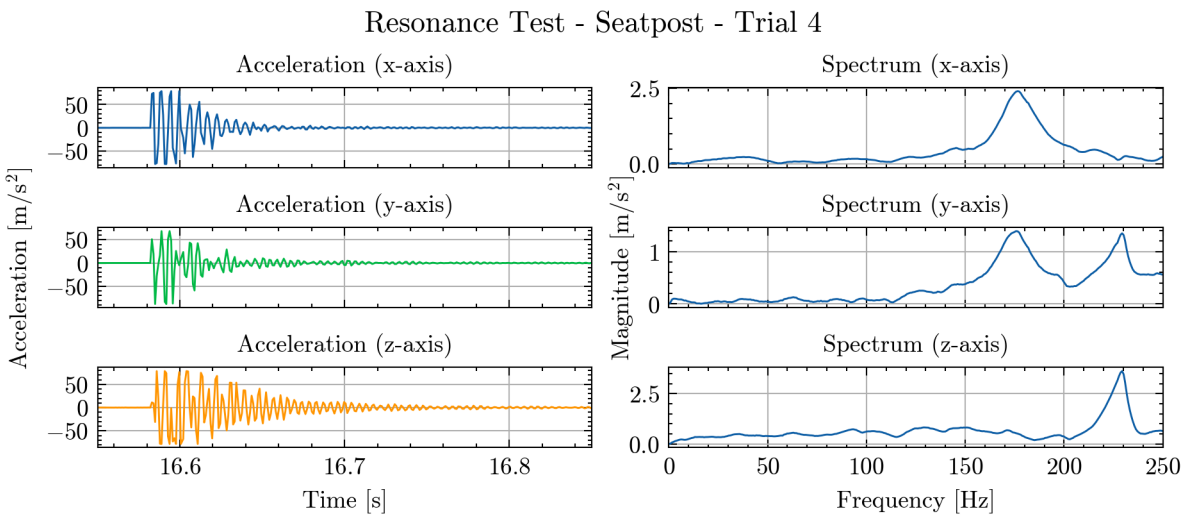

(b) Response of the seatpost's IMU.

Figure E.2: Frequency responses of the different mounts in the resonance test.

Table E.1: Resonance frequencies of the IMUs mountings (mean ± standard deviation). The lowest resonance for each component is shown in bold.

Component	x-axis [Hz]	y-axis [Hz]	z-axis [Hz]
Seatpost	**206.15** ± 47.94	218.88 ± 28.63	231.03 ± 2.34
Handlebar	341.37 ± 88.81	**199.00** ± 23.37	389.57 ± 107.75

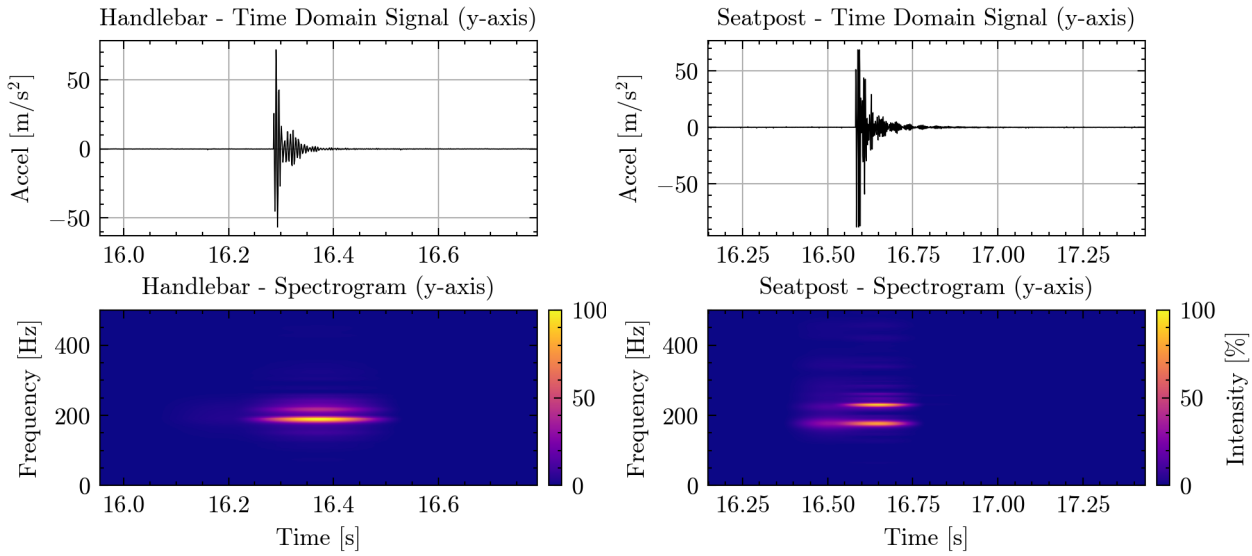

(a) Handlebar's IMU

(b) Seatpost's IMU

Figure E.3: Spectograms under an impulse on the main axis for trial 4 on each IMU's tests.

bar sensors are summarized in Table E.1. These values represent the mean and standard deviation across repeated impulse tests. For each component, the axis with the lowest resonance frequency, is highlighted in bold.

To provide a clearer representation of the resonance behavior over time, spectrograms were computed. These spectrograms, shown in Figure E.3, display the time-varying frequency content of the acceleration signals, with intensity representing the magnitude of each frequency component. Unlike the static spectrum, which shows the overall frequency content, the spectrogram enables visualization of how specific frequencies are excited immediately after the impulse and how they decay over time. This clearly illustrates how the impulse response, which appear as short-duration, display high-intensity bands centered around the identified resonance frequencies.

The resonance frequencies observed for the different axis are not a matter of concern when studying the vibration on the system, because of multiple reasons. Firstly, the power absorbed in the human body, which will be the major absorbed of energy in the system, peaks around 5 Hz [12, 31, 32], building surrounding this value, the frequencies of interest. Secondly, the frequencies of excitation as shown in 2.2 do not reach even 15 Hz. Lastly, the data will be filtered with a cut-off frequency of 120 Hz following the ISO regulations [49], and therefore, these higher frequencies will not be even reflected on the data to analyse.

E.2. Transient

A key requirement for the main experiment is that measurements must be taken during steady-state vibration conditions. The quantity of interest, power absorbed due to vibrations, depends on consistent and repeatable input and response characteristics. If measurements are taken during a transient phase, they may not reflect the true energy dissipation behavior of the system, leading to erroneous results.

The transient is defined as the period of time during which the system is changing from one stable state to another, before it reaches a new steady state. If the system is still transitioning when data is being collected, the resulting values for absorbed power or acceleration may be overestimated, underestimated, or simply inconsistent across runs. Therefore, the motivation for this preliminary test

Figure E.4: Set-up for the single shock transient test.

was to determine how long the system takes to settle into a steady-state response after an input change. Ensuring that all measurements are taken after this period or that is not long enough to affect the results. For this, two different concerns will be checked. Firstly, the transient due to a shock or single bump, to know how long does it take to the system to mitigate the vibrations caused by the impact. Secondly, a test is performed on the experimental set-up described in 2.1, but on a longer stretch of obstacles, 10 to be more specific, to see if a transient can be identified within this amount of disturbances.

E.2.1. Single shock

Description of the test

This test was designed to evaluate the transient vibration response of the bicycle-rider system following a sudden excitation, a shock event represented by riding over a bump. The goal was to assess how different test conditions affect the duration and nature of the transient response and ensure that the speed measurement at the end of the experimental stretch defined in 2.1 was taken with the system having ceased the vibration.

In vibration systems, the transient state under a sudden input change as a step or impulse, typically manifests as decaying oscillations together with changes in amplitude and phase before the system stabilizes. To quantify this, tests were conducted where a known input, a pulse excitation, was applied, and the system's time-domain response was monitored by means of the acceleration. The goal was to identify when the signal amplitude and frequency stabilized, allowing confident identification of the steady-state regime suitable for accurate kinetic energy measurement of the system.

The experimental setup involved the rider approaching a wooden bump placed on a flat path, as seen in Figure E.4, at a certain speed. To eliminate variability due to pedaling forces, the rider ceased pedaling on the first cone, three meters before the bump, and did not brake or made an evasive maneuver until the second cone, at another three meters from the bump.

The bump itself was a wooden plank with the edge rounded to reduce the risk of tire damage or rim impact at higher approaching speeds. Multiple test runs were conducted under varying conditions to study how different parameters, such as approach speed, bump size or rider behaviour affect the transient response. These are described below:

- Plank size: Three planks' heights were used: 12, 20 and 24 mm. The rider went through those planks at least 3 times in the same direction aiming at an entry speed of 30km/h.
- Speed dependence: With the 20mm plank, three speeds were tested to prove the dependence of the speed into the transient behaviour. For this, the rider passed at least 3 times over the bumps with three target entry speeds: 20, 30 and 35 km/h.
- Rider muscle behaviour: Since the system stiffness is playing an important role into the vibration energy transmission, it is expected to have a contribution into the transient behaviour on a

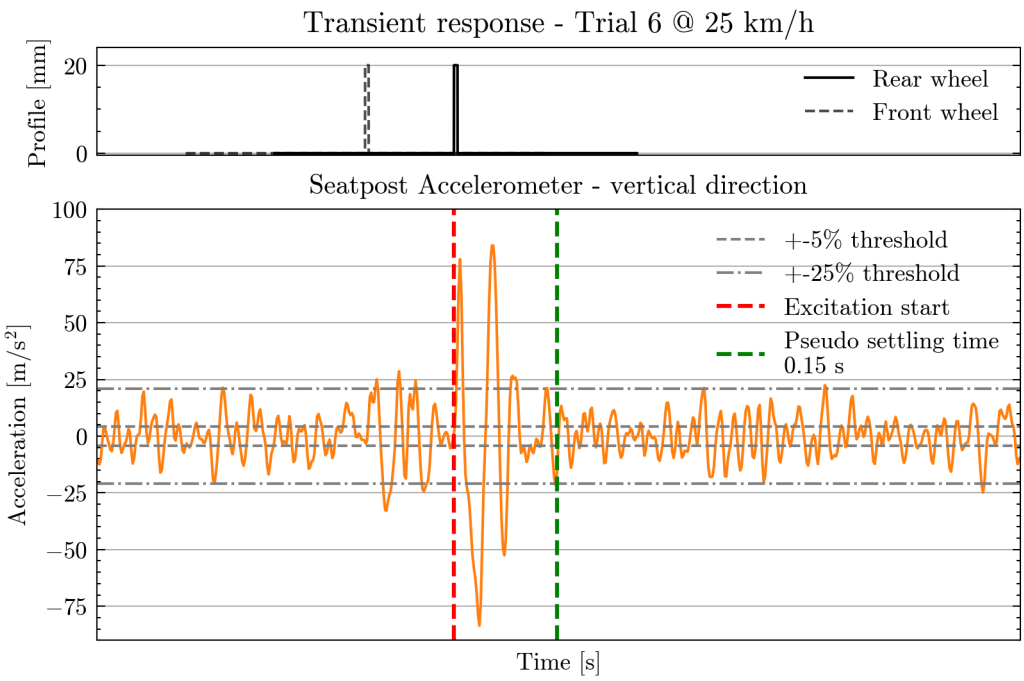

Figure E.5: Example of a transient behaviour.

shock. For this, the rider with a target speed of 30km/h over the 20mm plank, adopted 2 extreme behaviours: relaxed and stiff. With relax, the instructions are to lossen the body as much as possible, even the grip to the handle bar and allowing the bicycle to have more relative motion from the body. For the stiff attitude, the instruction is behaving as one with the bicycle, pretending to be as stiff as possible in the body and connected as rigidly as possible to the bike. These behaviours are compared to the previous test, where the rider behaved in a natural riding attitude.

All tests were performed with a rider mass of 100 kg and tire pressure set to 5 bar in both wheels.

Results

After all the runs over the plank, the windows showing the data before and after the bump are identified and the transient studied. The transient region is commonly characterized with the settling time. This is defined as the time required for the system to settle within a specified amplitude band, commonly around $\pm 5\%$ of the peak response magnitude, after a change in the input state [59]. Even though, this is usually obtained for the response of the system to a step input, in this case it would be obtained for an square pulse that the plank represent.

In every window, this transient time was attempted to be computed, however, due to the roughness of the pavement in which this test was performed, it was not possible to reach this $\pm 5\%$ stable value. This was neither achieved before or after the bump. Therefore, based a 'Pseudo-settling time' was defined for $\pm 25\%$ of the peak, since this value was the range in which the vibrations were oscillating before the bump. Both this settling times can be seen in E.5. This pseudo-settling time was computed for all the windows across conditions, for the vertical acceleration on the seatpost, as it was the signal with the largest perturbation. The results grouped by condition tested can be seen in E.6.

The differences between the tested conditions are relatively small and the errors are too large to conclude any relevant differences. Furthermore and more relevant outcome is that the transient is fast, around 0.1 s. Concluding that the transient behaviour of the system after a bump can be considered negligible if more than 0.1 s of margin are given. For the tested speeds on the experiment of the project, this would mean in the worst case scenario of 30 km/h, a distance needed to settle the vibrations effect of ± 0.85 m. Concluding that 3 meters after the last obstacle on the set-up described would allow for mitigate the vibrations due to the planks, and allowing then to assume that no vibration energy remains in the system and the velocity of the bicycle can be used to represent the whole kinetic energy of the bicycle-rider system.

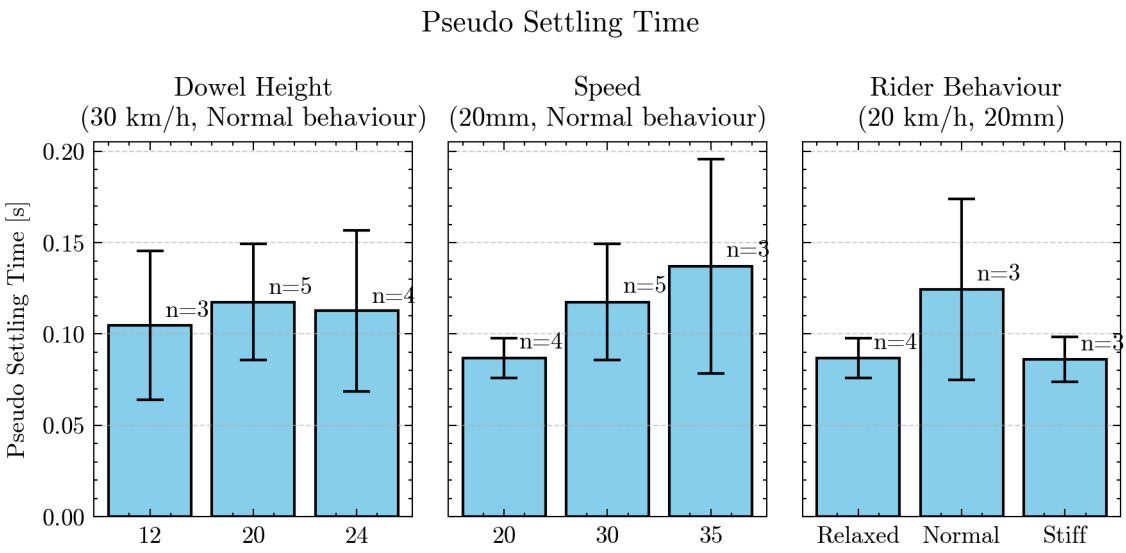

Figure E.6: Pseudo-settling times found in the transient experiment.

E.2.2. Transient over repetitive disturbances.

The same way a system responds to a sudden input change, it also responds to a repetitive input. To clarify this, it can be clearly exemplified by imagining a mass attached with a spring to the motion source. If the motion input is sinusoidal, it will take a certain amount of time or oscillations for the mass to follow the input motion. During this time, the transient is defined. Applied to the experimental set-up described in 2.1, the amount of planks placed on the stretch represents the oscillations on the example just mentioned. Therefore, to make sure the right amount of planks were placed without measuring the transient behaviour, the same test was done first with 10 planks. For this, the same road (cobbles with a BRI of 257.1), and planks with correct spacing (90x20 mm planks spaced 1.69 m) were choosen to ride at 15 km/h.

In the results, no evolution of the transient was seen over the bumps. An example of a trial is provided in Figure E.7, where it can be seen that almost from the first bump, the magnitudes oscillate in the same ranges, achieving the same peaks with every impulse caused by the plank.

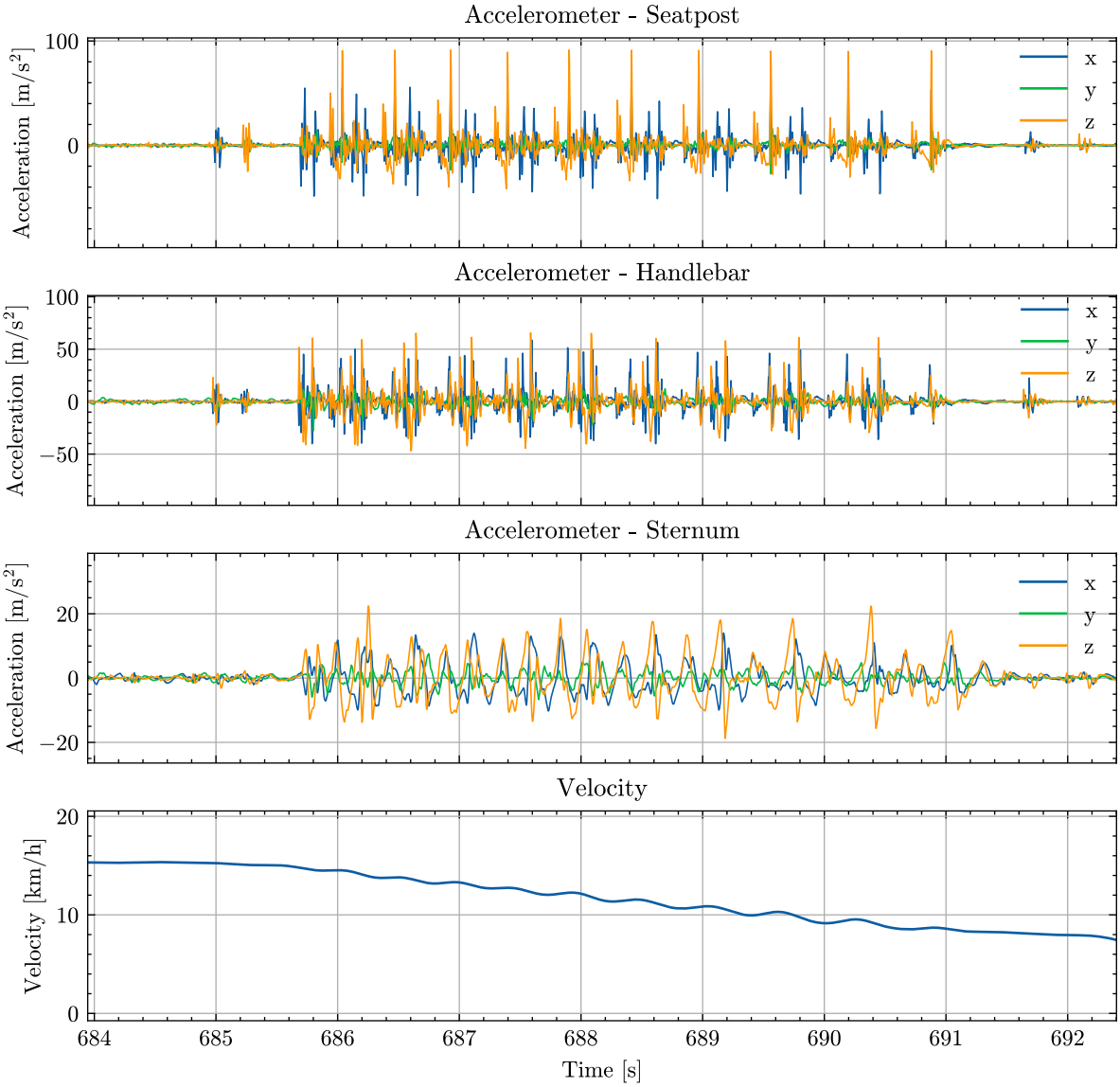

Figure E.7: Evolution of the vibrations over the stretch of bumps

F

Detailed results

On the tables below, a clarification on the nomenclature used:

- Behaviour: Three behaviours are tested relaxed, normal and stiff (RB, NB and SB respectively).
- Posture: It can be 'OffSaddle' for riding out of the saddle or 'Seated' for a normal seating position.
- Power Loss: referring to the power loss registered on the stretch, without isolating the vibration losses.
- Aero Loss: estimated power loss due to the aerodynamic drag.
- RR Loss: estimated power loss due to the rolling resistance.

On the tables made as summaries for each condition, the mean power loss or vibration loss is computed, together with the standard deviation of the mean (std) and the number of trials used for the averaging (count).

F.1. Reference session

Table F.1: Summary of reference trial losses

Tire pressure [bar]	Behaviour	Posture	Power Loss (mean) [W]	std [W]	count
3.50	NB	OffSaddle	63.62	33.52	9
3.50	NB	Seated	73.67	42.44	9
4.00	NB	OffSaddle	56.66	33.60	9
4.00	NB	Seated	72.87	42.84	9
4.50	NB	OffSaddle	49.40	24.38	8
4.50	NB	Seated	61.27	22.09	9
5.00	NB	Seated	53.08	16.59	9
5.50	NB	Seated	59.14	23.48	9

Table F.2: Reference trial losses per trial

Tire pressure [bar]	Behaviour	Posture	Average speed [km/h]	Starting speed [km/h]	Ending speed [km/h]	Speed loss [km/h]	Trial time [s]	Power Loss [W]
3.50	NB	OffSaddle	9.54	11.56	7.22	4.34	9.56	35.50
3.50	NB	OffSaddle	9.52	11.42	7.32	4.10	9.57	33.50
3.50	NB	OffSaddle	10.42	11.59	8.42	3.17	8.73	30.25
3.50	NB	OffSaddle	11.43	13.37	9.57	3.79	7.97	45.54
3.50	NB	OffSaddle	14.24	16.15	13.26	2.89	6.42	55.13
3.50	NB	OffSaddle	19.07	19.86	17.72	2.14	4.80	69.98
3.50	NB	OffSaddle	19.51	21.24	18.13	3.11	4.68	108.90
3.50	NB	OffSaddle	21.50	23.59	20.74	2.86	4.26	124.01
3.50	NB	OffSaddle	17.74	19.02	16.60	2.42	5.15	69.73
3.50	NB	Seated	9.10	11.44	6.82	4.62	10.08	34.86
3.50	NB	Seated	8.53	10.95	6.15	4.80	10.74	31.83
3.50	NB	Seated	10.46	12.43	8.42	4.01	8.77	39.76
3.50	NB	Seated	12.54	14.34	10.77	3.57	7.32	51.05
3.50	NB	Seated	13.62	15.46	12.01	3.45	6.73	58.79
3.50	NB	Seated	14.31	15.98	12.73	3.25	6.39	60.76
3.50	NB	Seated	21.43	22.99	19.79	3.20	4.27	133.72
3.50	NB	Seated	22.64	24.06	21.38	2.67	4.04	125.42
3.50	NB	Seated	22.08	23.48	20.85	2.63	3.84	126.80
4.00	NB	OffSaddle	8.86	10.80	6.41	4.39	10.25	30.73
4.00	NB	OffSaddle	8.64	10.73	6.28	4.45	10.52	30.00
4.00	NB	OffSaddle	8.99	10.47	6.82	3.65	10.12	26.02
4.00	NB	OffSaddle	12.10	14.29	9.96	4.33	7.52	58.17
4.00	NB	OffSaddle	13.43	14.21	12.01	2.20	6.79	35.40
4.00	NB	OffSaddle	16.73	17.59	16.13	1.45	5.45	37.55
4.00	NB	OffSaddle	19.24	20.47	18.03	2.44	4.75	82.64
4.00	NB	OffSaddle	20.19	22.12	18.91	3.21	4.51	121.94
4.00	NB	OffSaddle	18.94	20.43	17.79	2.64	4.81	87.52
4.00	NB	Seated	9.43	11.70	7.26	4.43	9.65	36.30
4.00	NB	Seated	8.74	11.01	6.50	4.51	10.45	31.49
4.00	NB	Seated	8.44	10.80	6.11	4.69	10.80	30.62
4.00	NB	Seated	14.66	16.35	12.98	3.36	6.23	65.97
4.00	NB	Seated	13.45	15.25	11.75	3.50	6.79	57.96
4.00	NB	Seated	13.82	15.55	12.25	3.31	6.61	57.91
4.00	NB	Seated	21.13	22.92	19.18	3.74	4.30	152.72
4.00	NB	Seated	19.85	21.54	18.43	3.10	4.60	112.35
4.00	NB	Seated	20.17	21.75	18.79	2.96	4.53	110.55
4.50	NB	OffSaddle	9.02	10.31	6.86	3.45	10.06	24.56
4.50	NB	OffSaddle	9.69	11.53	7.65	3.88	9.35	33.21
4.50	NB	OffSaddle	10.61	11.62	8.88	2.75	8.56	27.41
4.50	NB	OffSaddle	14.03	14.88	13.03	1.85	6.47	33.33
4.50	NB	OffSaddle	12.44	13.96	10.59	3.37	7.29	47.32
4.50	NB	OffSaddle	19.08	20.27	18.28	2.00	4.78	67.16
4.50	NB	OffSaddle	19.21	20.84	18.18	2.66	4.74	91.38
4.50	NB	OffSaddle	18.11	19.63	17.31	2.32	5.05	70.80
4.50	NB	Seated	10.61	12.64	8.65	3.99	8.58	41.24
4.50	NB	Seated	10.51	12.31	8.61	3.71	8.66	37.32

Tire pressure [bar]	Behaviour	Posture	Average speed [km/h]	Starting speed [km/h]	Ending speed [km/h]	Speed loss [km/h]	Trial time [s]	Power Loss [W]
4.50	NB	Seated	10.76	12.81	8.90	3.90	8.47	41.70
4.50	NB	Seated	12.57	14.50	11.02	3.48	7.24	51.18
4.50	NB	Seated	14.65	16.45	13.34	3.11	6.21	62.31
4.50	NB	Seated	13.37	15.04	11.95	3.08	6.82	50.87
4.50	NB	Seated	19.29	20.88	18.20	2.68	4.75	92.08
4.50	NB	Seated	18.58	20.22	17.38	2.84	4.91	90.69
4.50	NB	Seated	19.11	20.64	18.16	2.48	4.77	84.05
5.00	NB	Seated	8.97	11.22	6.75	4.48	10.16	33.02
5.00	NB	Seated	11.19	13.12	9.34	3.78	8.17	43.35
5.00	NB	Seated	7.73	10.09	5.28	4.80	11.72	26.27
5.00	NB	Seated	14.08	15.92	12.68	3.25	6.46	59.88
5.00	NB	Seated	13.46	15.27	11.87	3.40	6.76	56.89
5.00	NB	Seated	12.41	14.28	10.67	3.60	7.32	51.24
5.00	NB	Seated	19.37	20.67	18.61	2.06	4.73	71.22
5.00	NB	Seated	14.25	16.07	12.95	3.12	6.38	59.24
5.00	NB	Seated	18.82	20.45	18.15	2.30	4.84	76.61
5.50	NB	Seated	9.06	11.37	6.84	4.53	10.01	34.34
5.50	NB	Seated	8.74	10.88	6.52	4.37	10.36	30.57
5.50	NB	Seated	9.33	11.64	7.38	4.26	9.64	35.04
5.50	NB	Seated	13.30	15.14	11.94	3.20	6.82	52.96
5.50	NB	Seated	14.95	16.72	13.67	3.06	6.08	63.70
5.50	NB	Seated	13.73	15.51	12.33	3.18	6.61	55.81
5.50	NB	Seated	18.98	20.71	17.94	2.77	4.80	93.18
5.50	NB	Seated	19.31	21.08	18.69	2.39	4.73	83.69
5.50	NB	Seated	19.72	21.33	19.07	2.27	4.60	82.94

F.2. Vibration results

Table F.3: Summary of the vibration losses per condition.

Target speed [km/h]	Tire pressure [bar]	Behaviour	Posture	Estimated Aero Loss [W]	Estimated RR Loss [W]	Vibration Loss (mean) [W]	Vibration Loss (std) [W]	count
10	3.50	NB	OffSaddle	3.74	32.41	5.28	3.03	4
10	3.50	NB	Seated	5.52	32.41	45.62	5.87	4
10	3.50	RB	Seated	5.52	32.41	26.37	1.82	3
10	3.50	SB	Seated	5.52	32.41	37.56	5.56	3
10	4.00	NB	OffSaddle	3.74	33.60	10.62	6.53	3
10	4.00	NB	Seated	5.52	33.60	34.35	1.88	3
10	4.00	RB	Seated	5.52	33.60	27.32	0.74	3
10	4.00	SB	Seated	5.52	33.60	29.05	5.45	3
10	4.50	NB	OffSaddle	3.74	27.51	16.91	12.34	2
10	4.50	NB	Seated	5.52	27.51	38.04	4.92	2
10	4.50	RB	Seated	5.52	27.51	31.39	6.12	3
10	4.50	SB	Seated	5.52	27.51	40.93	9.61	3
10	5.00	NB	OffSaddle	3.74	26.15	14.42	3.39	3
10	5.00	NB	Seated	5.52	26.15	38.10	3.24	2
10	5.00	RB	Seated	5.52	26.15	29.90	0.66	2
10	5.00	SB	Seated	5.52	26.15	42.45	3.57	3
10	5.50	NB	OffSaddle	3.74	26.96	10.52	1.47	2
10	5.50	NB	Seated	5.52	26.96	43.90	2.69	2
10	5.50	RB	Seated	5.52	26.96	34.27	0.64	2
10	5.50	SB	Seated	5.52	26.96	51.62	NaN	1
15	3.50	NB	OffSaddle	12.63	48.61	25.26	15.68	3
15	3.50	NB	Seated	18.63	48.61	48.36	3.32	3
15	3.50	RB	Seated	18.63	48.61	35.31	1.60	3
15	3.50	SB	Seated	18.63	48.61	49.74	1.24	3
15	4.00	NB	OffSaddle	12.63	50.40	13.00	6.93	2
15	4.00	NB	Seated	18.63	50.40	49.12	8.45	3
15	4.00	RB	Seated	18.63	50.40	40.12	6.07	3
15	4.00	SB	Seated	18.63	50.40	48.26	2.23	3
15	4.50	NB	OffSaddle	12.63	41.27	27.09	18.98	2
15	4.50	NB	Seated	18.63	41.27	51.81	3.77	2
15	4.50	RB	Seated	18.63	41.27	40.81	8.48	2
15	4.50	SB	Seated	18.63	41.27	54.22	4.52	3
15	5.00	NB	OffSaddle	12.63	39.22	51.87	3.41	3
15	5.00	NB	Seated	18.63	39.22	56.57	6.20	4
15	5.00	RB	Seated	18.63	39.22	48.16	1.09	3
15	5.00	SB	Seated	18.63	39.22	52.40	6.56	3
15	5.50	NB	OffSaddle	12.63	40.44	47.84	19.90	3
15	5.50	NB	Seated	18.63	40.44	60.86	2.21	3
15	5.50	RB	Seated	18.63	40.44	43.45	2.29	3
15	5.50	SB	Seated	18.63	40.44	55.71	7.16	2
20	3.50	NB	OffSaddle	29.94	64.82	62.67	45.50	3
20	3.50	NB	Seated	44.15	64.82	79.09	9.42	3
20	3.50	RB	Seated	44.15	64.82	69.26	15.73	3
20	3.50	SB	Seated	44.15	64.82	81.68	6.37	4

Target speed [km/h]	Tire pressure [bar]	Behaviour	Posture	Estimated Aero Loss [W]	Estimated RR Loss [W]	Vibration Loss (mean) [W]	Vibration Loss (std) [W]	count
20	4.00	NB	OffSaddle	29.94	67.21	63.27	32.56	4
20	4.00	NB	Seated	44.15	67.21	83.54	6.06	3
20	4.00	RB	Seated	44.15	67.21	97.41	11.19	3
20	4.00	SB	Seated	44.15	67.21	94.57	11.92	6
20	4.50	NB	OffSaddle	29.94	55.03	74.94	5.97	3
20	4.50	NB	Seated	44.15	55.03	97.26	6.71	3
20	4.50	RB	Seated	44.15	55.03	94.75	2.91	3
20	4.50	SB	Seated	44.15	55.03	106.93	14.83	3
20	5.00	NB	OffSaddle	29.94	52.30	79.26	31.28	3
20	5.00	NB	Seated	44.15	52.30	104.45	3.06	2
20	5.00	RB	Seated	44.15	52.30	96.81	4.19	2
20	5.00	SB	Seated	44.15	52.30	110.77	3.64	3
20	5.50	NB	OffSaddle	29.94	53.91	98.66	27.56	5
20	5.50	NB	Seated	44.15	53.91	129.77	13.96	4
20	5.50	RB	Seated	44.15	53.91	111.17	27.83	4
20	5.50	SB	Seated	44.15	53.91	112.15	16.89	4
25	3.50	NB	OffSaddle	58.47	81.02	100.06	29.81	3
25	3.50	NB	Seated	86.23	81.02	164.83	4.05	4
25	3.50	RB	Seated	86.23	81.02	151.28	6.08	3
25	3.50	SB	Seated	86.23	81.02	109.42	8.54	3
25	4.00	NB	OffSaddle	58.47	84.01	128.20	88.61	2
25	4.00	NB	Seated	86.23	84.01	155.68	14.83	3
25	4.00	RB	Seated	86.23	84.01	180.13	40.24	3
25	4.00	SB	Seated	86.23	84.01	112.95	1.11	3
25	4.50	NB	OffSaddle	58.47	68.79	111.10	92.69	3
25	4.50	NB	Seated	86.23	68.79	193.36	17.40	3
25	4.50	RB	Seated	86.23	68.79	188.83	19.95	3
25	4.50	SB	Seated	86.23	68.79	148.92	19.75	3
25	5.00	NB	OffSaddle	58.47	65.37	131.74	55.36	3
25	5.00	NB	Seated	86.23	65.37	208.27	24.22	3
25	5.00	RB	Seated	86.23	65.37	189.01	14.07	3
25	5.00	SB	Seated	86.23	65.37	164.37	31.16	3
25	5.50	NB	OffSaddle	58.47	67.39	157.11	52.40	3
25	5.50	NB	Seated	86.23	67.39	203.75	12.08	3
25	5.50	RB	Seated	86.23	67.39	182.91	34.98	3
25	5.50	SB	Seated	86.23	67.39	148.55	10.83	3
30	3.50	NB	OffSaddle	101.04	97.22	99.91	NaN	1
30	3.50	NB	Seated	149.01	97.22	164.01	5.32	3
30	3.50	RB	Seated	149.01	97.22	140.96	67.60	3
30	3.50	SB	Seated	149.01	97.22	97.85	63.26	4
30	4.00	NB	Seated	149.01	100.81	190.20	24.55	4
30	4.50	NB	Seated	149.01	82.54	294.11	74.96	3
30	5.00	NB	Seated	149.01	78.44	305.41	26.21	2
30	5.50	NB	Seated	149.01	80.87	351.37	75.17	4

Table F.4: Results and vibration loss per trial.

Target speed [km/h]	Tire pressure [bar]	Behaviour	Posture	Average speed [km/h]	Starting speed [km/h]	Ending speed [km/h]	Speed loss [km/h]	Trial time [s]	Power Loss [W]	Aero Loss [W]	RR Loss [W]	Vibration Loss [W]
10	3.50	NB	OffSaddle	8.88	9.72	7.73	1.99	3.67	39.37	2.62	28.77	7.98
10	3.50	NB	OffSaddle	9.01	9.51	7.86	1.65	3.61	33.06	2.73	29.18	1.15
10	3.50	NB	OffSaddle	8.38	9.29	7.23	2.05	3.88	36.38	2.20	27.16	7.02
10	3.50	NB	OffSaddle	8.31	9.24	7.31	1.93	3.92	34.06	2.15	26.93	4.98
10	3.50	NB	Seated	8.02	10.07	6.11	3.96	4.06	65.79	2.85	26.00	36.93
10	3.50	NB	Seated	8.90	10.91	6.81	4.10	3.67	82.61	3.88	28.83	49.89
10	3.50	NB	Seated	8.93	10.87	6.90	3.97	3.65	80.66	3.93	28.94	47.79
10	3.50	NB	Seated	9.09	10.99	7.12	3.87	3.59	81.46	4.14	29.45	47.86
10	3.50	RB	Seated	8.42	9.99	6.82	3.17	3.88	57.17	3.29	27.27	26.61
10	3.50	RB	Seated	8.07	9.75	6.29	3.46	4.05	57.10	2.90	26.14	28.06
10	3.50	RB	Seated	7.90	9.52	6.20	3.32	4.13	52.76	2.72	25.59	24.45
10	3.50	SB	Seated	8.86	10.84	7.15	3.69	3.63	76.21	3.83	28.70	43.67
10	3.50	SB	Seated	8.63	10.46	6.96	3.50	3.76	67.69	3.54	27.95	36.19
10	3.50	SB	Seated	8.52	10.30	6.92	3.38	3.80	63.85	3.42	27.62	32.81
10	4.00	NB	OffSaddle	9.01	9.80	7.95	1.85	3.60	37.98	2.74	30.27	4.98
10	4.00	NB	OffSaddle	8.88	10.27	7.83	2.44	3.66	50.22	2.62	29.83	17.78
10	4.00	NB	OffSaddle	9.11	10.02	8.00	2.02	3.57	42.52	2.83	30.60	9.09
10	4.00	NB	Seated	8.26	10.14	6.45	3.69	3.93	64.85	3.11	27.76	33.97
10	4.00	NB	Seated	8.45	10.12	6.54	3.57	3.85	64.41	3.33	28.39	32.70
10	4.00	NB	Seated	8.40	10.25	6.48	3.77	3.87	67.90	3.27	28.23	36.39
10	4.00	RB	Seated	8.62	10.11	6.96	3.15	3.78	59.22	3.54	28.98	26.71
10	4.00	RB	Seated	7.97	9.72	6.16	3.56	4.09	57.71	2.79	26.78	28.14
10	4.00	RB	Seated	8.37	9.96	6.67	3.28	3.89	58.48	3.24	28.14	27.10
10	4.00	SB	Seated	8.16	9.94	6.51	3.43	3.99	59.05	2.99	27.40	28.65
10	4.00	SB	Seated	8.93	10.62	7.28	3.33	3.62	68.62	3.93	30.01	34.69
10	4.00	SB	Seated	7.67	9.41	5.96	3.44	4.24	52.08	2.49	25.78	23.81
10	4.50	NB	OffSaddle	8.98	9.24	6.84	2.40	4.51	35.62	2.71	24.72	8.19
10	4.50	NB	OffSaddle	8.19	9.62	6.70	2.93	3.96	50.22	2.05	22.53	25.64
10	4.50	NB	Seated	8.04	9.83	6.25	3.58	4.03	59.56	2.87	22.13	34.56
10	4.50	NB	Seated	8.18	10.17	6.30	3.87	3.96	67.06	3.02	22.51	41.53
10	4.50	RB	Seated	9.15	10.68	7.59	3.08	3.55	66.11	4.23	25.17	36.71
10	4.50	RB	Seated	8.79	10.32	7.25	3.06	3.70	60.68	3.74	24.18	32.76
10	4.50	RB	Seated	8.19	9.62	6.70	2.92	3.96	50.25	3.03	22.53	24.69
10	4.50	SB	Seated	8.65	10.61	6.79	3.82	3.75	73.84	3.57	23.80	46.47
10	4.50	SB	Seated	8.72	10.58	6.78	3.80	3.71	74.16	3.66	23.99	46.50
10	4.50	SB	Seated	7.60	9.46	5.93	3.53	4.27	53.17	2.42	20.91	29.83
10	5.00	NB	OffSaddle	8.74	9.67	7.83	1.83	3.70	36.14	2.50	22.85	10.79
10	5.00	NB	OffSaddle	9.97	10.79	8.92	1.87	3.25	47.30	3.71	26.07	17.51
10	5.00	NB	OffSaddle	10.10	10.83	9.08	1.74	3.20	45.23	3.86	26.42	14.95
10	5.00	NB	Seated	7.94	9.77	6.12	3.65	4.08	59.32	2.76	20.75	35.81
10	5.00	NB	Seated	8.21	10.10	6.37	3.73	3.95	64.93	3.06	21.48	40.39
10	5.00	RB	Seated	9.71	10.89	8.40	2.49	3.34	59.89	5.06	25.40	29.44
10	5.00	RB	Seated	8.32	9.86	6.75	3.11	3.89	55.29	3.18	21.75	30.37
10	5.00	SB	Seated	8.01	9.96	6.20	3.76	4.05	62.58	2.84	20.94	38.80
10	5.00	SB	Seated	8.39	10.27	6.54	3.73	3.86	67.81	3.26	21.93	42.61
10	5.00	SB	Seated	8.71	10.68	7.06	3.62	3.70	72.37	3.65	22.78	45.94

Target speed [km/h]	Tire pressure [bar]	Behaviour	Posture	Average speed [km/h]	Starting speed [km/h]	Ending speed [km/h]	Speed loss [km/h]	Trial time [s]	Power Loss [W]	Aero Loss [W]	RR Loss [W]	Vibration Loss [W]
10	5.50	NB	OffSaddle	9.87	10.30	8.87	1.43	2.87	39.69	3.60	26.61	9.48
10	5.50	NB	OffSaddle	8.62	9.26	7.23	2.03	3.75	37.21	2.40	23.25	11.55
10	5.50	NB	Seated	8.43	10.37	6.45	3.92	3.83	71.81	3.30	22.71	45.80
10	5.50	NB	Seated	8.26	10.19	6.37	3.82	3.91	67.37	3.11	22.26	42.00
10	5.50	RB	Seated	9.52	10.87	8.11	2.75	3.39	64.23	4.75	25.65	33.82
10	5.50	RB	Seated	8.82	10.40	7.31	3.09	3.67	62.28	3.78	23.77	34.73
10	5.50	SB	Seated	8.84	10.79	6.86	3.93	3.65	79.25	3.81	23.82	51.62
15	3.50	NB	OffSaddle	13.63	15.23	12.35	2.88	3.42	96.83	9.47	44.17	43.19
15	3.50	NB	OffSaddle	14.23	15.08	12.98	2.11	3.27	75.36	10.77	46.10	18.48
15	3.50	NB	OffSaddle	13.65	14.51	12.46	2.05	3.40	67.86	9.52	44.24	14.10
15	3.50	NB	Seated	14.37	15.92	12.81	3.11	3.24	115.12	16.37	46.56	52.18
15	3.50	NB	Seated	12.53	14.19	10.69	3.51	3.72	97.68	10.85	40.60	46.23
15	3.50	NB	Seated	13.67	15.21	12.06	3.15	3.41	105.07	14.10	44.30	46.67
15	3.50	RB	Seated	12.69	14.23	11.12	3.11	3.67	89.54	11.27	41.12	37.15
15	3.50	RB	Seated	11.97	13.51	10.27	3.24	3.89	82.63	9.45	38.78	34.40
15	3.50	RB	Seated	12.00	13.56	10.34	3.22	3.88	82.77	9.53	38.88	34.37
15	3.50	SB	Seated	14.57	16.07	13.11	2.96	3.20	112.58	17.06	47.21	48.32
15	3.50	SB	Seated	12.79	14.56	11.05	3.52	3.63	103.56	11.55	41.46	50.55
15	3.50	SB	Seated	12.75	14.52	10.99	3.53	3.64	103.15	11.45	41.33	50.36
15	4.00	NB	OffSaddle	13.60	14.28	12.34	1.95	3.41	63.24	9.42	45.71	8.10
15	4.00	NB	OffSaddle	13.04	14.09	11.78	2.31	3.56	70.01	8.29	43.81	17.91
15	4.00	NB	Seated	13.85	15.44	12.26	3.18	3.35	109.53	14.67	46.55	48.31
15	4.00	NB	Seated	13.08	15.08	11.41	3.67	3.54	114.28	12.36	43.96	57.96
15	4.00	NB	Seated	12.22	13.93	10.49	3.44	3.80	92.24	10.07	41.06	41.11
15	4.00	RB	Seated	13.84	15.39	12.23	3.16	3.36	108.28	14.64	46.52	47.12
15	4.00	RB	Seated	12.45	14.05	10.87	3.19	3.73	88.84	10.66	41.85	36.33
15	4.00	RB	Seated	12.88	14.38	11.28	3.11	3.61	91.99	11.79	43.28	36.92
15	4.00	SB	Seated	14.77	16.18	13.28	2.90	3.14	113.29	17.79	49.64	45.87
15	4.00	SB	Seated	14.51	15.95	12.91	3.03	3.20	114.24	16.84	48.74	48.65
15	4.00	SB	Seated	12.90	14.64	11.11	3.53	3.59	105.48	11.86	43.36	50.27
15	4.50	NB	OffSaddle	13.54	15.05	12.45	2.60	3.43	87.06	9.29	37.26	40.51
15	4.50	NB	OffSaddle	13.10	13.59	11.63	1.96	3.54	58.14	8.42	36.05	13.67
15	4.50	NB	Seated	13.23	14.82	11.50	3.31	3.51	103.64	12.77	36.39	54.48
15	4.50	NB	Seated	12.30	13.97	10.53	3.44	3.77	93.24	10.26	33.83	49.15
15	4.50	RB	Seated	13.05	14.56	11.44	3.12	3.56	94.96	12.26	35.90	46.81
15	4.50	RB	Seated	12.06	13.63	10.68	2.96	3.86	77.67	9.68	33.18	34.81
15	4.50	SB	Seated	14.20	15.61	12.72	2.89	3.27	104.37	15.79	39.06	49.52
15	4.50	SB	Seated	12.39	14.28	10.57	3.71	3.73	103.13	10.50	34.09	58.54
15	4.50	SB	Seated	12.80	14.49	11.05	3.44	3.61	101.41	11.58	35.22	54.61
15	5.00	NB	OffSaddle	14.27	15.59	12.80	2.79	3.24	102.06	10.87	37.31	53.88
15	5.00	NB	OffSaddle	13.90	15.32	12.45	2.88	3.33	100.18	10.04	36.34	53.80
15	5.00	NB	OffSaddle	14.02	15.47	12.82	2.66	3.30	94.93	10.32	36.67	47.93
15	5.00	NB	Seated	11.84	13.87	10.04	3.83	3.91	97.64	9.16	30.96	57.52
15	5.00	NB	Seated	12.71	14.60	10.99	3.62	3.64	106.06	11.34	33.24	61.48
15	5.00	NB	Seated	13.11	14.54	11.47	3.07	3.53	94.31	12.44	34.29	47.58
15	5.00	NB	Seated	13.76	15.39	12.17	3.22	3.37	110.02	14.37	35.97	59.68
15	5.00	RB	Seated	12.90	14.43	11.32	3.11	3.59	92.91	11.84	33.73	47.34
15	5.00	RB	Seated	13.03	14.47	11.32	3.15	3.54	95.69	12.22	34.08	49.40

Target speed [km/h]	Tire pressure [bar]	Behaviour	Posture	Average speed [km/h]	Starting speed [km/h]	Ending speed [km/h]	Speed loss [km/h]	Trial time [s]	Power Loss [W]	Aero Loss [W]	RR Loss [W]	Vibration Loss [W]
15	5.00	RB	Seated	13.23	14.68	11.65	3.03	3.50	95.10	12.77	34.58	47.74
15	5.00	SB	Seated	14.99	16.38	13.45	2.92	3.09	117.70	18.60	39.20	59.90
15	5.00	SB	Seated	12.62	14.23	10.96	3.27	3.66	93.59	11.09	32.99	49.51
15	5.00	SB	Seated	13.23	14.68	11.65	3.04	3.50	95.14	12.77	34.59	47.78
15	5.50	NB	OffSaddle	13.82	14.81	12.61	2.20	3.33	75.58	9.87	37.25	28.47
15	5.50	NB	OffSaddle	13.54	15.02	12.24	2.77	3.40	92.63	9.30	36.51	46.82
15	5.50	NB	OffSaddle	14.43	16.15	13.05	3.10	3.19	118.36	11.24	38.90	68.23
15	5.50	NB	Seated	13.24	14.99	11.46	3.53	3.48	111.64	12.82	35.70	63.13
15	5.50	NB	Seated	12.92	14.66	11.15	3.50	3.58	105.44	11.90	34.83	58.72
15	5.50	NB	Seated	13.26	14.98	11.54	3.44	3.48	109.35	12.87	35.75	60.73
15	5.50	RB	Seated	13.20	14.70	11.71	2.99	3.50	94.16	12.70	35.59	45.87
15	5.50	RB	Seated	12.27	13.87	10.68	3.19	3.77	86.44	10.19	33.07	43.19
15	5.50	RB	Seated	12.02	13.67	10.49	3.18	3.84	83.31	9.59	32.41	41.31
15	5.50	SB	Seated	15.02	16.47	13.53	2.95	3.07	119.98	18.71	40.50	60.78
15	5.50	SB	Seated	12.59	14.21	10.87	3.35	3.66	95.61	11.02	33.94	50.65
20	3.50	NB	OffSaddle	20.25	21.08	19.45	1.62	1.60	170.93	31.09	65.63	74.21
20	3.50	NB	OffSaddle	19.91	21.03	19.13	1.91	1.63	195.35	29.53	64.52	101.29
20	3.50	NB	OffSaddle	20.41	21.30	20.29	1.01	1.59	110.51	31.84	66.16	12.51
20	3.50	NB	Seated	18.87	19.83	17.85	1.99	1.73	180.38	37.05	61.14	82.19
20	3.50	NB	Seated	18.96	19.90	18.08	1.82	1.72	167.62	37.64	61.46	68.52
20	3.50	NB	Seated	18.89	19.89	17.86	2.03	1.72	185.01	37.21	61.22	86.57
20	3.50	RB	Seated	18.46	19.29	17.39	1.90	1.77	164.39	34.71	59.82	69.86
20	3.50	RB	Seated	17.23	18.17	15.92	2.25	1.90	168.75	28.23	55.84	84.68
20	3.50	RB	Seated	18.71	19.75	18.09	1.66	1.74	150.02	36.15	60.64	53.23
20	3.50	SB	Seated	20.30	21.28	19.40	1.88	1.61	198.50	46.15	65.78	86.57
20	3.50	SB	Seated	19.93	20.91	18.99	1.92	1.64	195.22	43.68	64.58	86.95
20	3.50	SB	Seated	20.56	21.43	19.68	1.75	1.59	188.17	47.96	66.63	73.58
20	3.50	SB	Seated	20.62	21.52	19.72	1.79	1.58	194.82	48.39	66.83	79.60
20	4.00	NB	OffSaddle	19.06	20.01	18.90	1.11	1.71	105.63	25.89	64.03	15.70
20	4.00	NB	OffSaddle	17.57	18.93	17.01	1.92	1.85	155.10	20.30	59.04	75.76
20	4.00	NB	OffSaddle	18.58	19.44	17.43	2.01	1.75	175.79	24.00	62.44	89.35
20	4.00	NB	OffSaddle	18.95	20.19	18.47	1.72	1.72	161.40	25.46	63.68	72.26
20	4.00	NB	Seated	19.26	20.21	18.22	1.99	1.69	188.19	39.41	64.71	84.08
20	4.00	NB	Seated	19.09	20.05	18.12	1.93	1.71	179.77	38.40	64.15	77.22
20	4.00	NB	Seated	19.26	20.29	18.25	2.04	1.69	193.46	39.43	64.72	89.31
20	4.00	RB	Seated	19.63	20.58	18.51	2.08	1.76	192.16	41.72	65.95	84.49
20	4.00	RB	Seated	20.24	21.23	19.01	2.22	1.71	217.59	45.75	68.01	103.83
20	4.00	RB	Seated	19.62	20.74	18.46	2.28	1.76	211.55	41.70	65.94	103.92
20	4.00	SB	Seated	19.18	20.10	18.09	2.01	1.70	188.37	38.93	64.44	85.00
20	4.00	SB	Seated	19.24	20.29	18.27	2.03	1.69	192.84	39.32	64.66	88.85
20	4.00	SB	Seated	20.74	21.64	19.78	1.85	1.57	203.77	49.24	69.70	84.83
20	4.00	SB	Seated	20.62	21.71	19.56	2.15	1.58	233.59	48.37	69.28	115.93
20	4.00	SB	Seated	19.20	20.34	18.19	2.15	1.69	203.77	39.09	64.53	100.15
20	4.00	SB	Seated	19.08	20.17	18.08	2.09	1.71	195.11	38.35	64.13	92.63
20	4.50	NB	OffSaddle	20.27	21.35	19.78	1.57	1.60	168.08	31.16	55.77	81.15
20	4.50	NB	OffSaddle	17.32	18.47	16.74	1.74	1.87	136.32	19.44	47.65	69.24
20	4.50	NB	OffSaddle	18.58	19.53	17.86	1.67	1.75	149.53	23.99	51.11	74.44
20	4.50	NB	Seated	18.25	19.33	17.25	2.08	1.78	177.76	33.54	50.21	94.01

Target speed [km/h]	Tire pressure [bar]	Behaviour	Posture	Average speed [km/h]	Starting speed [km/h]	Ending speed [km/h]	Speed loss [km/h]	Trial time [s]	Power Loss [W]	Aero Loss [W]	RR Loss [W]	Vibration Loss [W]
20	4.50	NB	Seated	18.49	19.53	17.50	2.03	1.76	178.56	34.89	50.87	92.79
20	4.50	NB	Seated	18.27	19.34	17.14	2.21	1.78	188.87	33.63	50.26	104.97
20	4.50	RB	Seated	18.31	19.34	17.27	2.07	1.78	177.79	33.88	50.38	93.54
20	4.50	RB	Seated	19.06	20.05	18.07	1.97	1.71	183.27	38.20	52.44	92.63
20	4.50	RB	Seated	17.62	18.71	16.49	2.22	1.84	176.75	30.20	48.48	98.07
20	4.50	SB	Seated	19.24	20.19	18.20	1.98	1.70	187.16	39.30	52.94	94.92
20	4.50	SB	Seated	18.84	19.91	17.81	2.10	1.73	191.09	36.91	51.84	102.35
20	4.50	SB	Seated	19.98	20.99	18.81	2.18	1.63	222.51	44.02	54.97	123.51
20	5.00	NB	OffSaddle	17.57	18.71	17.01	1.69	1.85	136.56	20.30	45.94	70.31
20	5.00	NB	OffSaddle	19.17	20.29	18.30	1.99	1.68	190.50	26.35	50.12	114.04
20	5.00	NB	OffSaddle	19.31	20.34	19.01	1.33	1.67	130.85	26.93	50.48	53.44
20	5.00	NB	Seated	17.95	19.06	16.82	2.24	1.81	185.49	31.93	46.94	106.62
20	5.00	NB	Seated	17.57	18.65	16.41	2.24	1.84	178.17	29.93	45.94	102.29
20	5.00	RB	Seated	17.69	18.70	16.58	2.12	1.83	170.62	30.53	46.24	93.85
20	5.00	RB	Seated	17.78	18.80	16.61	2.20	1.83	177.26	31.01	46.48	99.77
20	5.00	SB	Seated	18.16	19.25	17.02	2.23	1.78	189.25	33.07	47.49	108.69
20	5.00	SB	Seated	17.73	18.94	16.57	2.36	1.82	192.08	30.75	46.35	114.98
20	5.00	SB	Seated	17.78	18.92	16.63	2.29	1.82	186.19	31.04	46.50	108.65
20	5.50	NB	OffSaddle	18.59	19.65	17.93	1.72	1.73	155.49	24.06	50.13	81.30
20	5.50	NB	OffSaddle	17.26	18.26	16.61	1.65	1.87	127.80	19.24	46.52	62.04
20	5.50	NB	OffSaddle	18.51	19.81	17.79	2.02	1.75	181.17	23.72	49.89	107.56
20	5.50	NB	OffSaddle	19.92	21.36	19.28	2.08	1.63	216.76	29.59	53.71	133.46
20	5.50	NB	OffSaddle	19.17	20.57	18.64	1.93	1.69	187.02	26.37	51.69	108.96
20	5.50	NB	Seated	17.45	18.60	16.22	2.38	1.85	186.20	29.32	47.04	109.84
20	5.50	NB	Seated	18.78	20.05	17.52	2.53	1.73	229.67	36.56	50.63	142.48
20	5.50	NB	Seated	18.58	19.82	17.36	2.46	1.74	219.05	35.37	50.07	133.60
20	5.50	NB	Seated	18.60	19.83	17.38	2.45	1.74	218.80	35.52	50.14	133.14
20	5.50	RB	Seated	18.32	19.35	17.24	2.11	1.76	182.57	33.92	49.38	99.27
20	5.50	RB	Seated	17.09	18.07	16.02	2.05	1.89	154.25	27.56	46.08	80.62
20	5.50	RB	Seated	18.48	19.60	17.26	2.34	1.76	203.92	34.84	49.82	119.26
20	5.50	RB	Seated	20.25	21.47	19.15	2.32	1.60	245.96	45.82	54.59	145.55
20	5.50	SB	Seated	17.59	18.62	16.37	2.25	1.83	179.31	30.03	47.42	101.86
20	5.50	SB	Seated	17.55	18.71	16.32	2.39	1.85	189.05	29.84	47.32	111.89
20	5.50	SB	Seated	16.90	18.09	15.78	2.32	1.91	171.00	26.64	45.56	98.80
20	5.50	SB	Seated	19.16	20.38	17.98	2.40	1.69	226.57	38.84	51.66	136.07
25	3.50	NB	OffSaddle	23.53	24.74	23.40	1.34	1.30	206.45	48.72	76.24	81.48
25	3.50	NB	OffSaddle	23.35	25.06	23.38	1.68	1.31	257.73	47.62	75.66	134.45
25	3.50	NB	OffSaddle	25.18	26.70	25.44	1.25	1.21	225.57	59.73	81.60	84.25
25	3.50	NB	Seated	22.62	23.92	21.72	2.20	1.37	307.17	63.89	73.31	169.97
25	3.50	NB	Seated	24.28	25.46	23.47	1.99	1.27	318.52	79.00	78.69	160.84
25	3.50	NB	Seated	22.76	23.92	21.76	2.16	1.36	301.27	65.04	73.75	162.48
25	3.50	NB	Seated	23.86	25.09	23.03	2.06	1.30	318.25	74.93	77.31	166.01
25	3.50	RB	Seated	22.40	23.52	21.39	2.14	1.39	288.77	62.01	72.59	154.17
25	3.50	RB	Seated	23.97	25.13	23.22	1.91	1.29	297.98	76.00	77.68	144.29
25	3.50	RB	Seated	22.92	24.10	22.02	2.08	1.35	296.08	66.43	74.27	155.37
25	3.50	SB	Seated	24.15	25.06	23.43	1.63	1.29	255.78	77.77	78.28	99.73
25	3.50	SB	Seated	24.77	25.62	23.91	1.71	1.26	280.03	83.89	80.28	115.86
25	3.50	SB	Seated	23.97	24.84	23.11	1.73	1.30	266.31	75.98	77.67	112.66

Target speed [km/h]	Tire pressure [bar]	Behaviour	Posture	Average speed [km/h]	Starting speed [km/h]	Ending speed [km/h]	Speed loss [km/h]	Trial time [s]	Power Loss [W]	Aero Loss [W]	RR Loss [W]	Vibration Loss [W]
25	4.00	NB	OffSaddle	23.90	25.78	24.59	1.19	1.27	196.91	51.06	80.30	65.55
25	4.00	NB	OffSaddle	24.48	26.32	24.39	1.93	1.24	328.01	54.89	82.26	190.86
25	4.00	NB	Seated	23.43	24.54	22.59	1.95	1.33	288.29	71.00	78.74	138.55
25	4.00	NB	Seated	25.06	26.29	24.33	1.96	1.23	335.13	86.86	84.21	164.06
25	4.00	NB	Seated	24.14	25.32	23.27	2.05	1.28	323.22	77.66	81.13	164.43
25	4.00	RB	Seated	24.90	26.32	24.15	2.18	1.24	370.38	85.21	83.68	201.49
25	4.00	RB	Seated	24.09	25.36	23.54	1.82	1.27	291.85	77.18	80.96	133.72
25	4.00	RB	Seated	24.76	26.36	24.18	2.17	1.23	372.20	83.80	83.21	205.19
25	4.00	SB	Seated	25.10	25.99	24.32	1.68	1.24	283.48	87.22	84.33	111.93
25	4.00	SB	Seated	25.83	26.72	25.08	1.64	1.20	294.69	95.11	86.80	112.78
25	4.00	SB	Seated	25.69	26.58	24.92	1.66	1.21	294.03	93.57	86.32	114.14
25	4.50	NB	OffSaddle	22.59	24.11	22.33	1.78	1.34	256.45	43.13	62.15	151.17
25	4.50	NB	OffSaddle	23.01	24.56	23.82	0.74	1.31	114.01	45.59	63.31	5.11
25	4.50	NB	OffSaddle	23.01	24.61	22.70	1.91	1.32	285.87	45.56	63.30	177.01
25	4.50	NB	Seated	23.23	24.76	22.49	2.28	1.31	341.28	69.22	63.93	208.13
25	4.50	NB	Seated	24.51	25.85	23.76	2.09	1.25	346.42	81.23	67.43	197.76
25	4.50	NB	Seated	23.53	24.66	22.59	2.07	1.31	310.77	71.86	64.73	174.18
25	4.50	RB	Seated	23.44	24.80	22.66	2.14	1.30	325.37	71.11	64.51	189.75
25	4.50	RB	Seated	24.65	26.10	23.98	2.13	1.24	358.82	82.69	67.83	208.31
25	4.50	RB	Seated	24.17	25.27	23.29	1.98	1.28	312.90	77.95	66.51	168.43
25	4.50	SB	Seated	24.00	24.94	23.11	1.83	1.29	284.35	76.25	66.02	142.07
25	4.50	SB	Seated	25.67	26.68	24.80	1.89	1.21	335.22	93.40	70.64	171.18
25	4.50	SB	Seated	23.34	24.24	22.41	1.83	1.33	267.90	70.17	64.22	133.50
25	5.00	NB	OffSaddle	23.77	25.34	24.23	1.11	1.27	180.96	50.26	62.15	68.55
25	5.00	NB	OffSaddle	23.47	25.40	23.74	1.66	1.28	264.72	48.35	61.36	155.01
25	5.00	NB	OffSaddle	23.29	24.93	23.12	1.81	1.30	279.79	47.24	60.89	171.66
25	5.00	NB	Seated	22.81	24.05	21.82	2.22	1.35	314.67	65.46	59.63	189.57
25	5.00	NB	Seated	23.59	24.97	22.79	2.18	1.30	333.79	72.48	61.69	199.61
25	5.00	NB	Seated	25.32	26.79	24.60	2.19	1.20	391.45	89.61	66.21	235.63
25	5.00	RB	Seated	23.30	24.58	22.31	2.26	1.32	336.02	69.85	60.93	205.24
25	5.00	RB	Seated	23.24	24.53	22.45	2.08	1.31	310.31	69.29	60.77	180.25
25	5.00	RB	Seated	23.09	24.35	22.23	2.12	1.33	309.86	67.94	60.38	181.54
25	5.00	SB	Seated	25.19	26.25	24.36	1.89	1.23	324.54	88.26	65.88	170.40
25	5.00	SB	Seated	25.12	26.19	24.16	2.03	1.23	345.29	87.52	65.69	192.08
25	5.00	SB	Seated	24.06	25.03	23.30	1.73	1.29	270.40	76.85	62.91	130.64
25	5.50	NB	OffSaddle	23.03	24.74	22.58	2.16	1.32	324.05	45.69	62.07	216.29
25	5.50	NB	OffSaddle	22.69	24.26	22.59	1.66	1.34	243.34	43.69	61.15	138.50
25	5.50	NB	OffSaddle	23.35	24.77	23.31	1.46	1.29	227.10	47.61	62.93	116.56
25	5.50	NB	Seated	22.19	23.52	21.21	2.31	1.38	311.28	60.28	59.81	191.19
25	5.50	NB	Seated	24.09	25.59	23.38	2.22	1.27	357.41	77.19	64.95	215.27
25	5.50	NB	Seated	24.12	25.56	23.41	2.15	1.26	347.28	77.45	65.02	204.80
25	5.50	RB	Seated	23.58	25.00	22.81	2.19	1.29	337.76	72.32	63.56	201.88
25	5.50	RB	Seated	23.45	24.96	22.75	2.21	1.30	338.74	71.20	63.22	204.31
25	5.50	RB	Seated	22.50	23.57	21.63	1.93	1.37	266.07	62.87	60.66	142.54
25	5.50	SB	Seated	24.39	25.40	23.57	1.83	1.27	295.14	80.09	65.75	149.30
25	5.50	SB	Seated	24.25	25.22	23.46	1.76	1.27	281.44	78.70	65.37	137.36
25	5.50	SB	Seated	23.39	24.48	22.51	1.97	1.32	292.66	70.63	63.06	158.97
30	3.50	NB	OffSaddle	26.93	28.93	27.66	1.27	1.15	260.24	73.06	87.26	99.91

Target speed [km/h]	Tire pressure [bar]	Behaviour	Posture	Average speed [km/h]	Starting speed [km/h]	Ending speed [km/h]	Speed loss [km/h]	Trial time [s]	Power Loss [W]	Aero Loss [W]	RR Loss [W]	Vibration Loss [W]
30	3.50	NB	Seated	28.25	29.34	27.54	1.79	1.13	377.64	124.39	91.54	161.71
30	3.50	NB	Seated	27.90	28.99	27.18	1.81	1.14	370.46	119.83	90.41	160.22
30	3.50	NB	Seated	27.37	28.47	26.57	1.90	1.17	371.97	113.17	88.70	170.10
30	3.50	RB	Seated	28.43	29.65	27.71	1.94	1.12	413.61	126.79	92.13	194.69
30	3.50	RB	Seated	26.97	28.10	26.22	1.87	1.18	358.79	108.27	87.40	163.12
30	3.50	RB	Seated	27.89	29.07	27.74	1.33	1.15	275.23	119.77	90.40	65.07
30	3.50	SB	Seated	27.51	28.58	26.86	1.71	1.16	339.84	114.93	89.16	135.75
30	3.50	SB	Seated	27.82	28.88	27.20	1.69	1.15	343.35	118.88	90.17	134.29
30	3.50	SB	Seated	29.99	31.02	29.97	1.05	1.06	249.74	148.80	97.18	3.76
30	3.50	SB	Seated	28.05	29.05	27.45	1.60	1.14	330.22	121.74	90.89	117.59
30	4.00	NB	Seated	26.54	27.78	25.73	2.05	1.20	380.36	103.16	89.18	188.02
30	4.00	NB	Seated	28.63	29.82	27.72	2.09	1.11	451.11	129.49	96.20	225.41
30	4.00	NB	Seated	26.23	27.36	25.39	1.97	1.21	358.45	99.60	88.14	170.71
30	4.00	NB	Seated	29.12	30.20	28.35	1.85	1.10	410.84	136.33	97.87	176.65
30	4.50	NB	Seated	27.27	28.63	25.85	2.78	1.15	548.26	111.94	75.04	361.28
30	4.50	NB	Seated	27.75	29.13	26.68	2.45	1.13	502.12	117.97	76.36	307.80
30	4.50	NB	Seated	27.61	29.00	27.02	1.98	1.14	405.38	116.16	75.97	213.25
30	5.00	NB	Seated	26.80	28.19	25.77	2.43	1.18	463.22	106.25	70.08	286.88
30	5.00	NB	Seated	27.81	29.29	26.80	2.49	1.13	515.41	118.74	72.72	323.94
30	5.50	NB	Seated	25.74	27.28	24.92	2.36	1.22	422.68	94.12	69.39	259.17
30	5.50	NB	Seated	28.88	30.36	27.53	2.83	1.08	630.20	132.91	77.85	419.44
30	5.50	NB	Seated	27.63	29.04	26.51	2.53	1.15	512.38	116.45	74.49	321.43
30	5.50	NB	Seated	28.94	30.45	27.67	2.78	1.09	617.29	133.83	78.03	405.43

Table F.5: Contribution of each power loss.

Target speed [km/h]	Tire pressure [bar]	Behaviour	Posture	Vibration Loss (VL) [W]	VL contribution (%)	Aero Loss (AL) [W]	AL contribution (%)	RR Loss (RRL) [W]	RRL contribution (%)	Total Power Loss [W]
10	3.50	NB	OffSaddle	5.28	12.75	3.74	9.03	32.41	78.22	41.43
10	3.50	NB	Seated	45.62	54.60	5.52	6.61	32.41	38.79	83.55
10	3.50	RB	Seated	26.37	41.01	5.52	8.58	32.41	50.40	64.30
10	3.50	SB	Seated	37.56	49.76	5.52	7.31	32.41	42.93	75.48
10	4.00	NB	OffSaddle	10.62	22.13	3.74	7.80	33.60	70.06	47.96
10	4.00	NB	Seated	34.35	46.75	5.52	7.51	33.60	45.73	73.48
10	4.00	RB	Seated	27.32	41.11	5.52	8.31	33.60	50.58	66.44
10	4.00	SB	Seated	29.05	42.61	5.52	8.10	33.60	49.29	68.17
10	4.50	NB	OffSaddle	16.91	35.11	3.74	7.77	27.51	57.12	48.17
10	4.50	NB	Seated	38.04	53.52	5.52	7.76	27.51	38.71	71.08
10	4.50	RB	Seated	31.39	48.72	5.52	8.57	27.51	42.71	64.42

Target speed [km/h]	Tire pressure [bar]	Behaviour	Posture	Vibration Loss (VL) [W]	VL contribution (%)	Aero Loss (AL) [W]	AL contribution (%)	RR Loss (RRL) [W]	RRL contribution (%)	Total Power Loss [W]
10	4.50	SB	Seated	40.93	55.34	5.52	7.46	27.51	37.20	73.97
10	5.00	NB	OffSaddle	14.42	32.54	3.74	8.45	26.15	59.02	44.31
10	5.00	NB	Seated	38.10	54.61	5.52	7.91	26.15	37.48	69.77
10	5.00	RB	Seated	29.90	48.57	5.52	8.96	26.15	42.47	61.57
10	5.00	SB	Seated	42.45	57.28	5.52	7.45	26.15	35.28	74.12
10	5.50	NB	OffSaddle	10.52	25.51	3.74	9.08	26.96	65.41	41.21
10	5.50	NB	Seated	43.90	57.48	5.52	7.23	26.96	35.30	76.37
10	5.50	RB	Seated	34.27	51.35	5.52	8.27	26.96	40.39	66.75
10	5.50	SB	Seated	51.62	61.38	5.52	6.56	26.96	32.06	84.10
15	3.50	NB	OffSaddle	25.26	29.20	12.63	14.60	48.61	56.20	86.50
15	3.50	NB	Seated	48.36	41.84	18.63	16.11	48.61	42.05	115.60
15	3.50	RB	Seated	35.31	34.43	18.63	18.16	48.61	47.41	102.54
15	3.50	SB	Seated	49.74	42.52	18.63	15.92	48.61	41.55	116.98
15	4.00	NB	OffSaddle	13.00	17.10	12.63	16.61	50.40	66.29	76.04
15	4.00	NB	Seated	49.12	41.58	18.63	15.76	50.40	42.66	118.16
15	4.00	RB	Seated	40.12	36.76	18.63	17.06	50.40	46.18	109.15
15	4.00	SB	Seated	48.26	41.15	18.63	15.88	50.40	42.97	117.29
15	4.50	NB	OffSaddle	27.09	33.45	12.63	15.59	41.27	50.96	80.99
15	4.50	NB	Seated	51.81	46.38	18.63	16.67	41.27	36.94	111.71
15	4.50	RB	Seated	40.81	40.52	18.63	18.50	41.27	40.98	100.71
15	4.50	SB	Seated	54.22	47.51	18.63	16.32	41.27	36.17	114.12
15	5.00	NB	OffSaddle	51.87	50.01	12.63	12.18	39.22	37.81	103.72
15	5.00	NB	Seated	56.57	49.44	18.63	16.28	39.22	34.28	114.41
15	5.00	RB	Seated	48.16	45.43	18.63	17.57	39.22	37.00	106.01
15	5.00	SB	Seated	52.40	47.53	18.63	16.90	39.22	35.58	110.25
15	5.50	NB	OffSaddle	47.84	47.41	12.63	12.52	40.44	40.07	100.90
15	5.50	NB	Seated	60.86	50.75	18.63	15.53	40.44	33.72	119.92
15	5.50	RB	Seated	43.45	42.39	18.63	18.17	40.44	39.44	102.52
15	5.50	SB	Seated	55.71	48.54	18.63	16.23	40.44	35.23	114.78
20	3.50	NB	OffSaddle	62.67	39.81	29.94	19.02	64.82	41.17	157.42
20	3.50	NB	Seated	79.09	42.06	44.15	23.48	64.82	34.47	188.06
20	3.50	RB	Seated	69.26	38.86	44.15	24.77	64.82	36.37	178.22
20	3.50	SB	Seated	81.68	42.84	44.15	23.16	64.82	34.00	190.64
20	4.00	NB	OffSaddle	63.27	39.44	29.94	18.66	67.21	41.90	160.41
20	4.00	NB	Seated	83.54	42.86	44.15	22.65	67.21	34.48	194.90
20	4.00	RB	Seated	97.41	46.66	44.15	21.15	67.21	32.19	208.77
20	4.00	SB	Seated	94.57	45.92	44.15	21.44	67.21	32.64	205.92
20	4.50	NB	OffSaddle	74.94	46.87	29.94	18.72	55.03	34.41	159.91
20	4.50	NB	Seated	97.26	49.51	44.15	22.48	55.03	28.01	196.44
20	4.50	RB	Seated	94.75	48.86	44.15	22.77	55.03	28.38	193.93
20	4.50	SB	Seated	106.93	51.88	44.15	21.42	55.03	26.70	206.11
20	5.00	NB	OffSaddle	79.26	49.08	29.94	18.54	52.30	32.38	161.49
20	5.00	NB	Seated	104.45	51.99	44.15	21.98	52.30	26.03	200.90
20	5.00	RB	Seated	96.81	50.09	44.15	22.85	52.30	27.06	193.26
20	5.00	SB	Seated	110.77	53.46	44.15	21.31	52.30	25.24	207.22
20	5.50	NB	OffSaddle	98.66	54.06	29.94	16.40	53.91	29.54	182.52
20	5.50	NB	Seated	129.77	56.96	44.15	19.38	53.91	23.66	227.83

Target speed [km/h]	Tire pressure [bar]	Behaviour	Posture	Vibration Loss (VL) [W]	VL contribution (%)	Aero Loss (AL) [W]	AL contribution (%)	RR Loss (RRL) [W]	RRL contribution (%)	Total Power Loss [W]
20	5.50	RB	Seated	111.17	53.13	44.15	21.10	53.91	25.77	209.24
20	5.50	SB	Seated	112.15	53.35	44.15	21.00	53.91	25.65	210.22
25	3.50	NB	OffSaddle	100.06	41.77	58.47	24.41	81.02	33.82	239.55
25	3.50	NB	Seated	164.83	49.63	86.23	25.97	81.02	24.40	332.08
25	3.50	RB	Seated	151.28	47.49	86.23	27.07	81.02	25.44	318.53
25	3.50	SB	Seated	109.42	39.55	86.23	31.17	81.02	29.28	276.67
25	4.00	NB	OffSaddle	128.20	47.36	58.47	21.60	84.01	31.04	270.68
25	4.00	NB	Seated	155.68	47.77	86.23	26.46	84.01	25.78	325.92
25	4.00	RB	Seated	180.13	51.41	86.23	24.61	84.01	23.98	350.37
25	4.00	SB	Seated	112.95	39.88	86.23	30.45	84.01	29.66	283.19
25	4.50	NB	OffSaddle	111.10	46.61	58.47	24.53	68.79	28.86	238.35
25	4.50	NB	Seated	193.36	55.50	86.23	24.75	68.79	19.74	348.38
25	4.50	RB	Seated	188.83	54.92	86.23	25.08	68.79	20.00	343.85
25	4.50	SB	Seated	148.92	49.00	86.23	28.37	68.79	22.63	303.94
25	5.00	NB	OffSaddle	131.74	51.55	58.47	22.88	65.37	25.58	255.58
25	5.00	NB	Seated	208.27	57.87	86.23	23.96	65.37	18.16	359.87
25	5.00	RB	Seated	189.01	55.49	86.23	25.32	65.37	19.19	340.61
25	5.00	SB	Seated	164.37	52.02	86.23	27.29	65.37	20.69	315.97
25	5.50	NB	OffSaddle	157.11	55.52	58.47	20.66	67.39	23.82	282.98
25	5.50	NB	Seated	203.75	57.01	86.23	24.13	67.39	18.86	357.38
25	5.50	RB	Seated	182.91	54.35	86.23	25.62	67.39	20.03	336.54
25	5.50	SB	Seated	148.55	49.16	86.23	28.54	67.39	22.30	302.17
30	3.50	NB	OffSaddle	99.91	33.51	101.04	33.89	97.22	32.61	298.17
30	3.50	NB	Seated	164.01	39.98	149.01	36.32	97.22	23.70	410.24
30	3.50	RB	Seated	140.96	36.41	149.01	38.48	97.22	25.11	387.19
30	3.50	SB	Seated	97.85	28.44	149.01	43.31	97.22	28.26	344.08
30	4.00	NB	Seated	190.20	43.23	149.01	33.86	100.81	22.91	440.02
30	4.50	NB	Seated	294.11	55.95	149.01	28.35	82.54	15.70	525.66
30	5.00	NB	Seated	305.41	57.32	149.01	27.96	78.44	14.72	532.87
30	5.50	NB	Seated	351.37	60.45	149.01	25.64	80.87	13.91	581.25

F.2.1. Posture comparison

Table F.6: Comparison of vibration loss between postures.

Speed [km/h]	Pressure [bar]	VL Seated [W]	VL Offsaddle [W]	% Difference
10	3.50	45.62	5.28	88.42
10	4.00	34.35	10.62	69.10
10	4.50	38.04	16.91	55.55
10	5.00	38.10	14.42	62.16
10	5.50	43.90	10.52	76.05
15	3.50	48.36	25.26	47.77
15	4.00	49.12	13.00	73.53
15	4.50	51.81	27.09	47.71
15	5.00	56.57	51.87	8.30
15	5.50	60.86	47.84	21.40
20	3.50	79.09	62.67	20.76
20	4.00	83.54	63.27	24.27
20	4.50	97.26	74.94	22.94
20	5.00	104.45	79.26	24.12
20	5.50	129.77	98.66	23.97
25	3.50	164.83	100.06	39.29
25	4.00	155.68	128.20	17.65
25	4.50	193.36	111.10	42.54
25	5.00	208.27	131.74	36.75
25	5.50	203.75	157.11	22.89

G

Additional Graphs

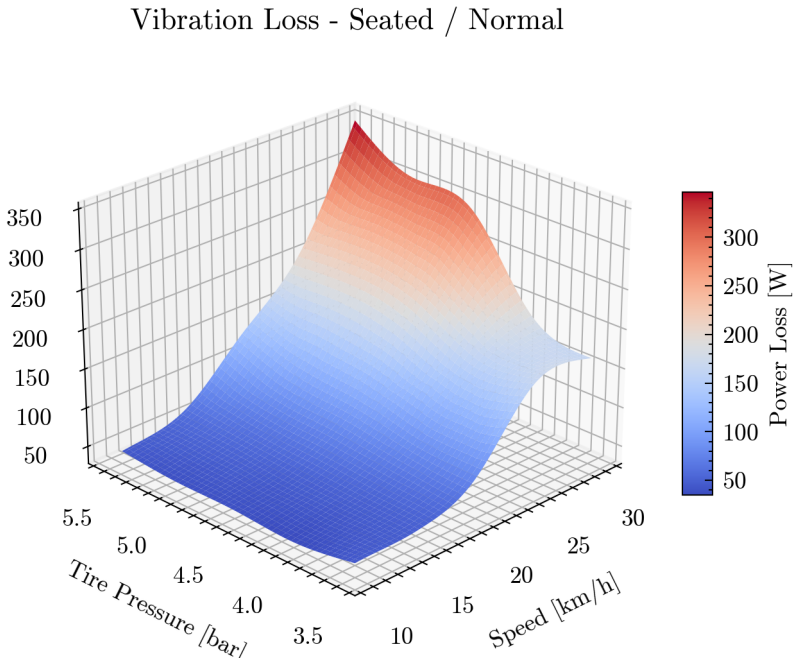

Figure G.1: 3D surface visualization, used to check for a smooth interpolation.

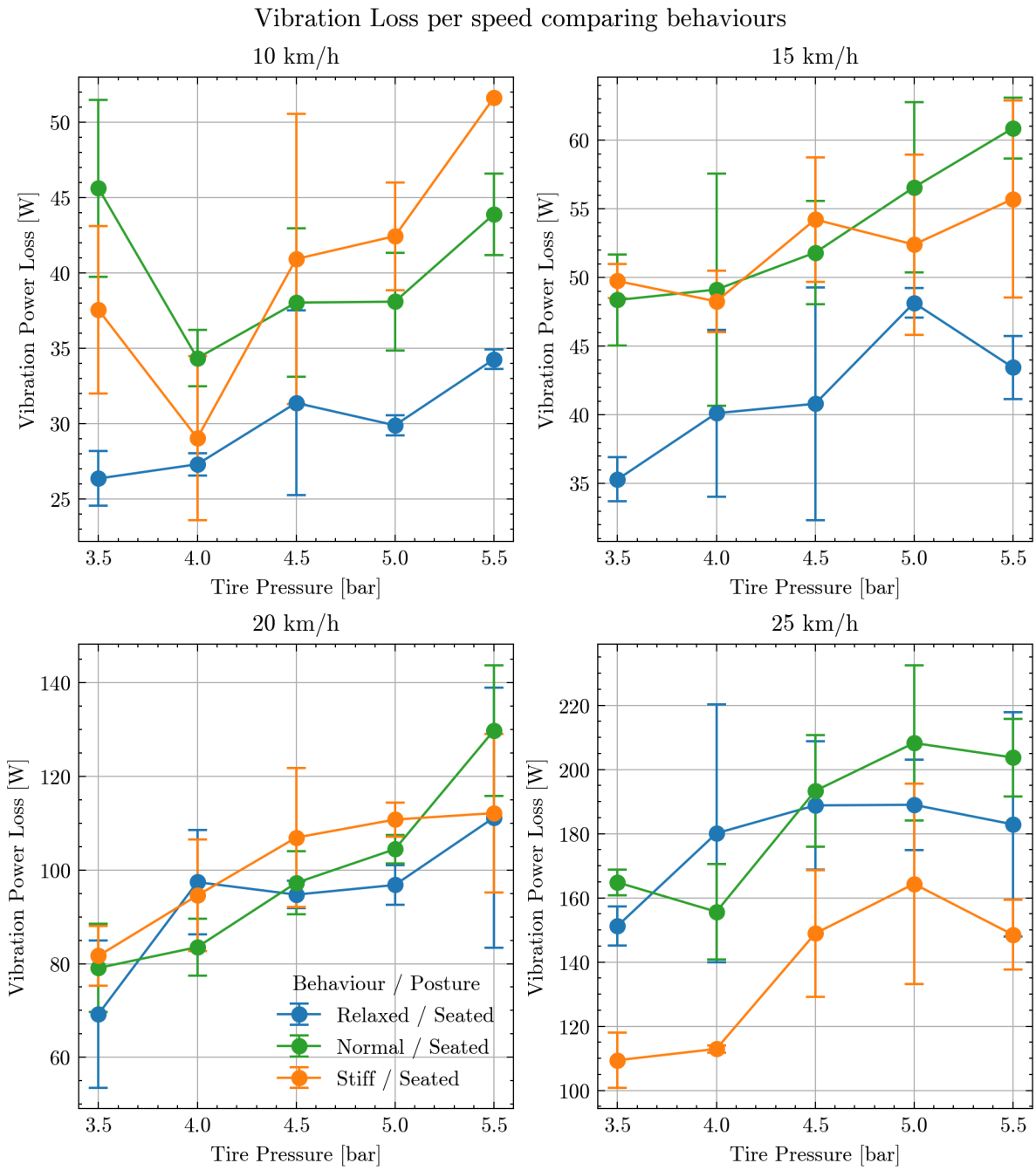

Figure G.2: Comparison of vibration losses across rider behaviours at various speeds.

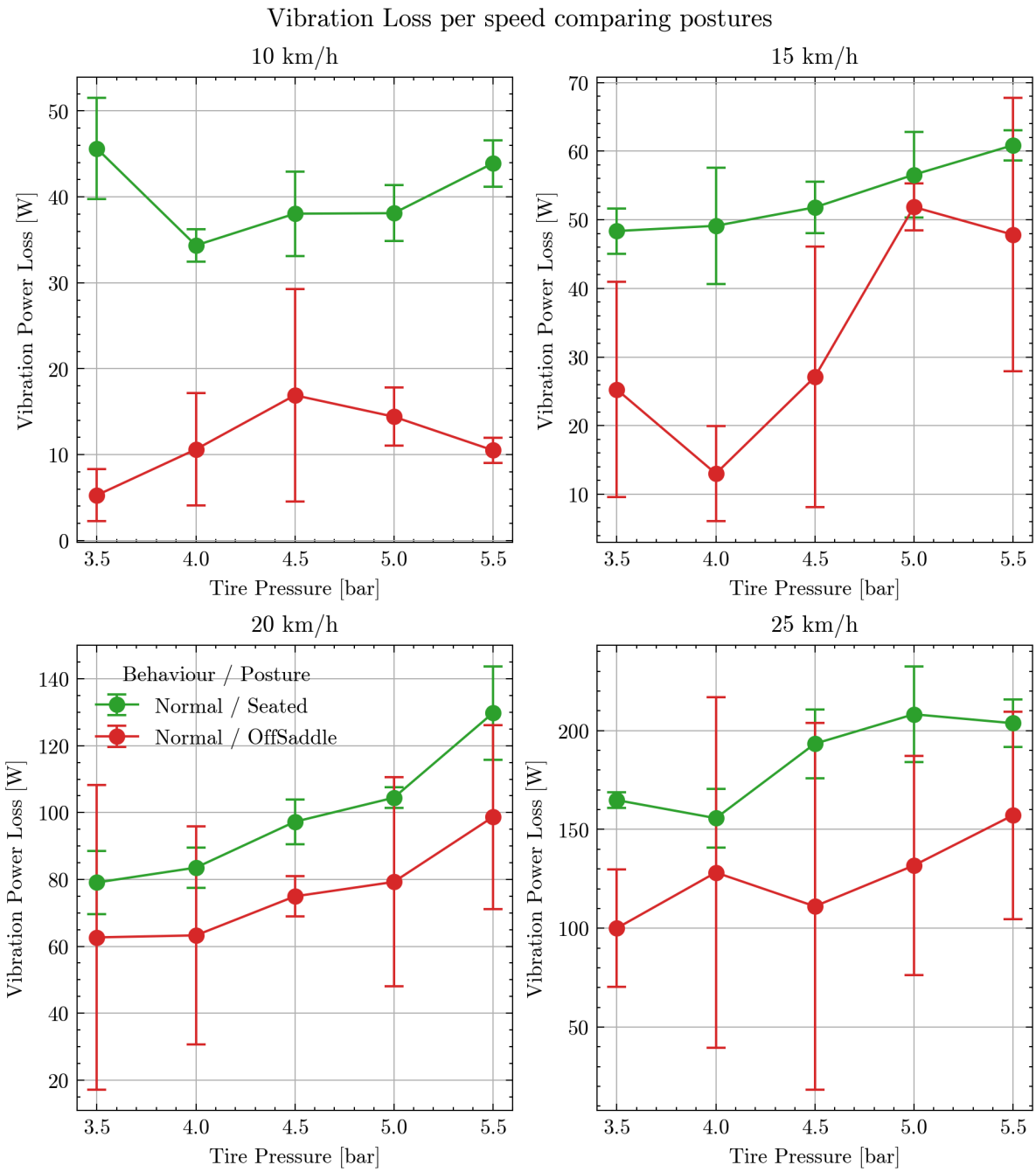

Figure G.3: Comparison of vibration losses across rider postures at various speeds.

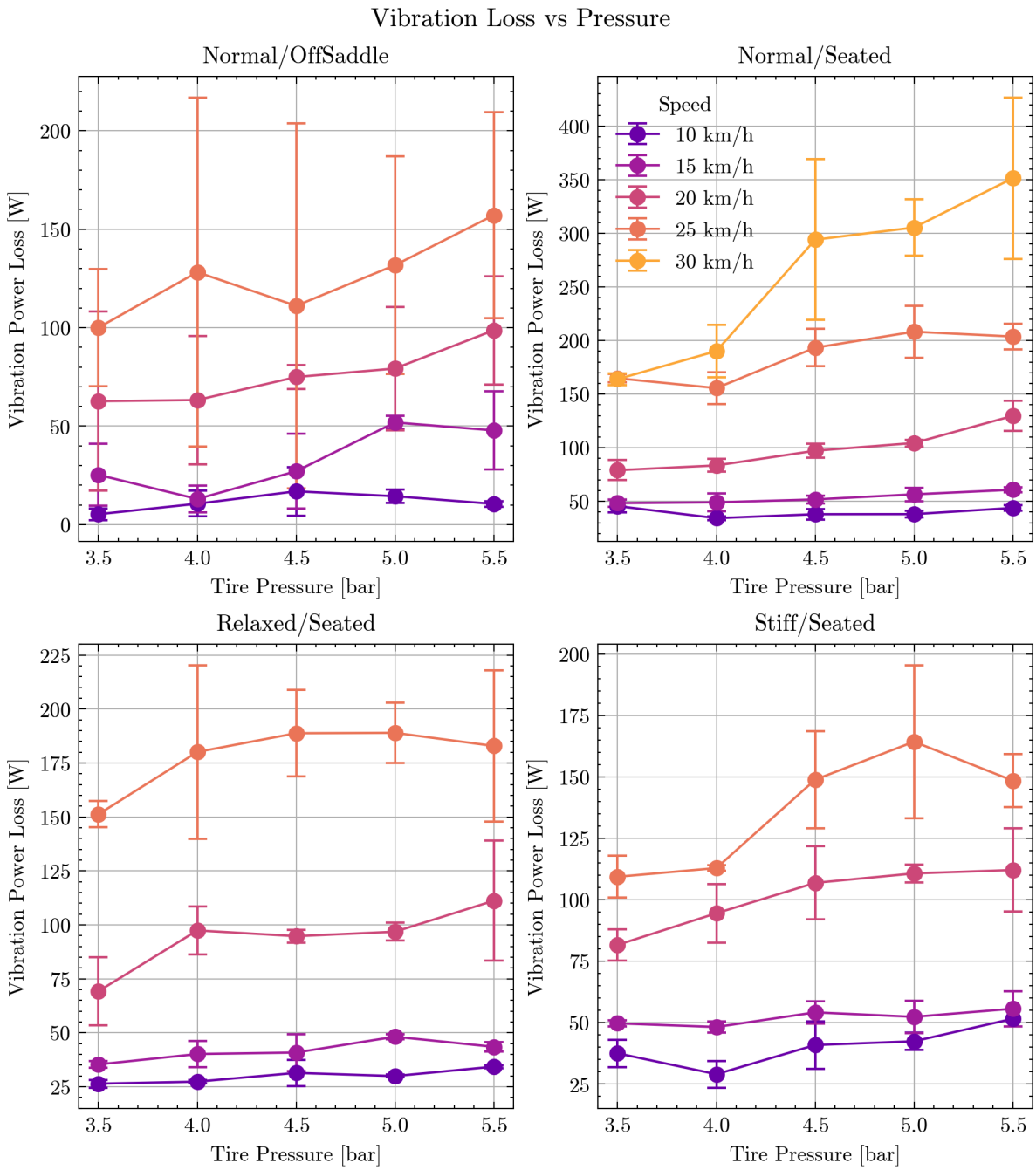

Figure G.4: Pressure dependance for each posture-behaviour pair comparing different speeds.

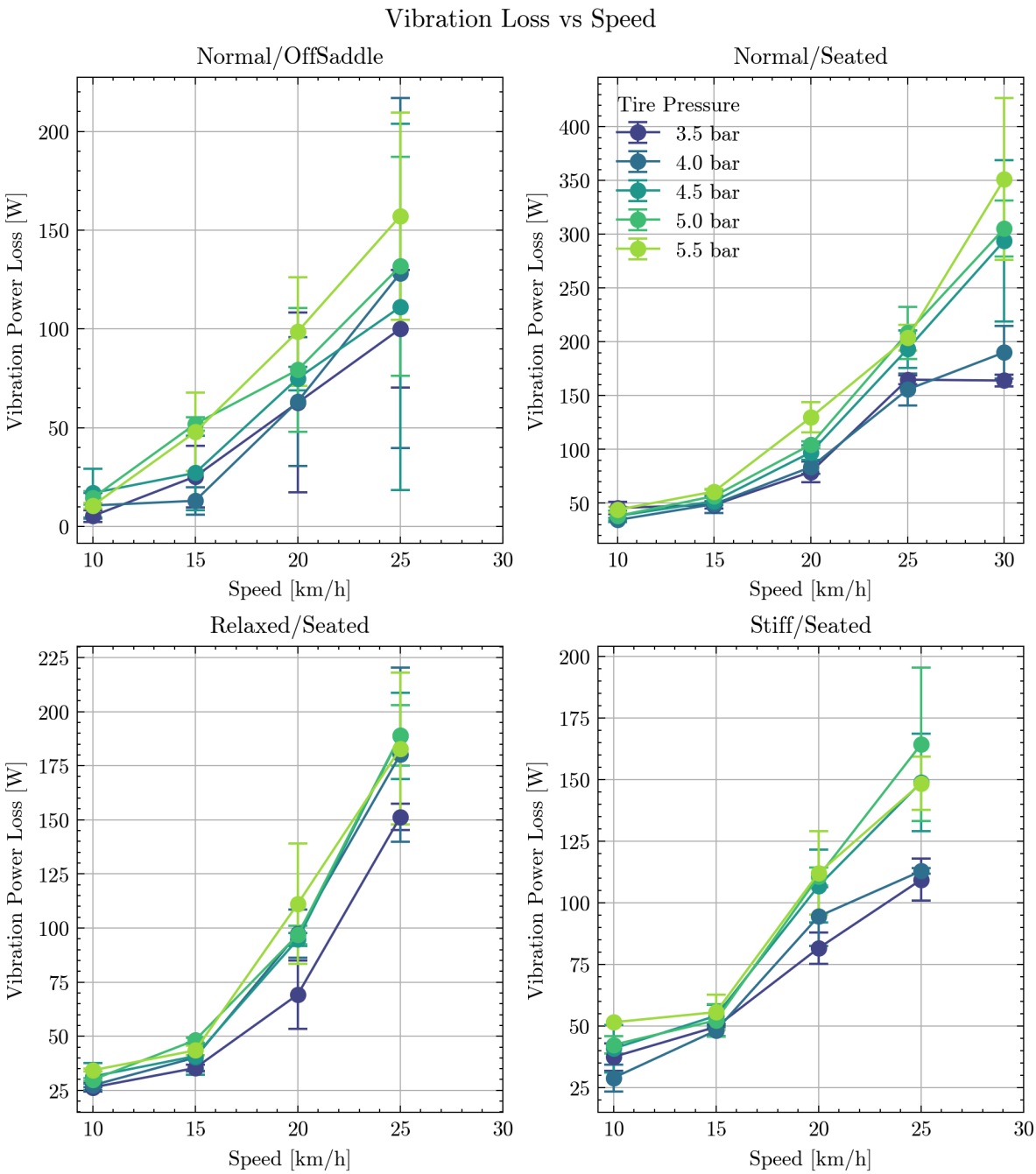

Figure G.5: Speed dependance for each posture-behaviour pair comparing different pressures.

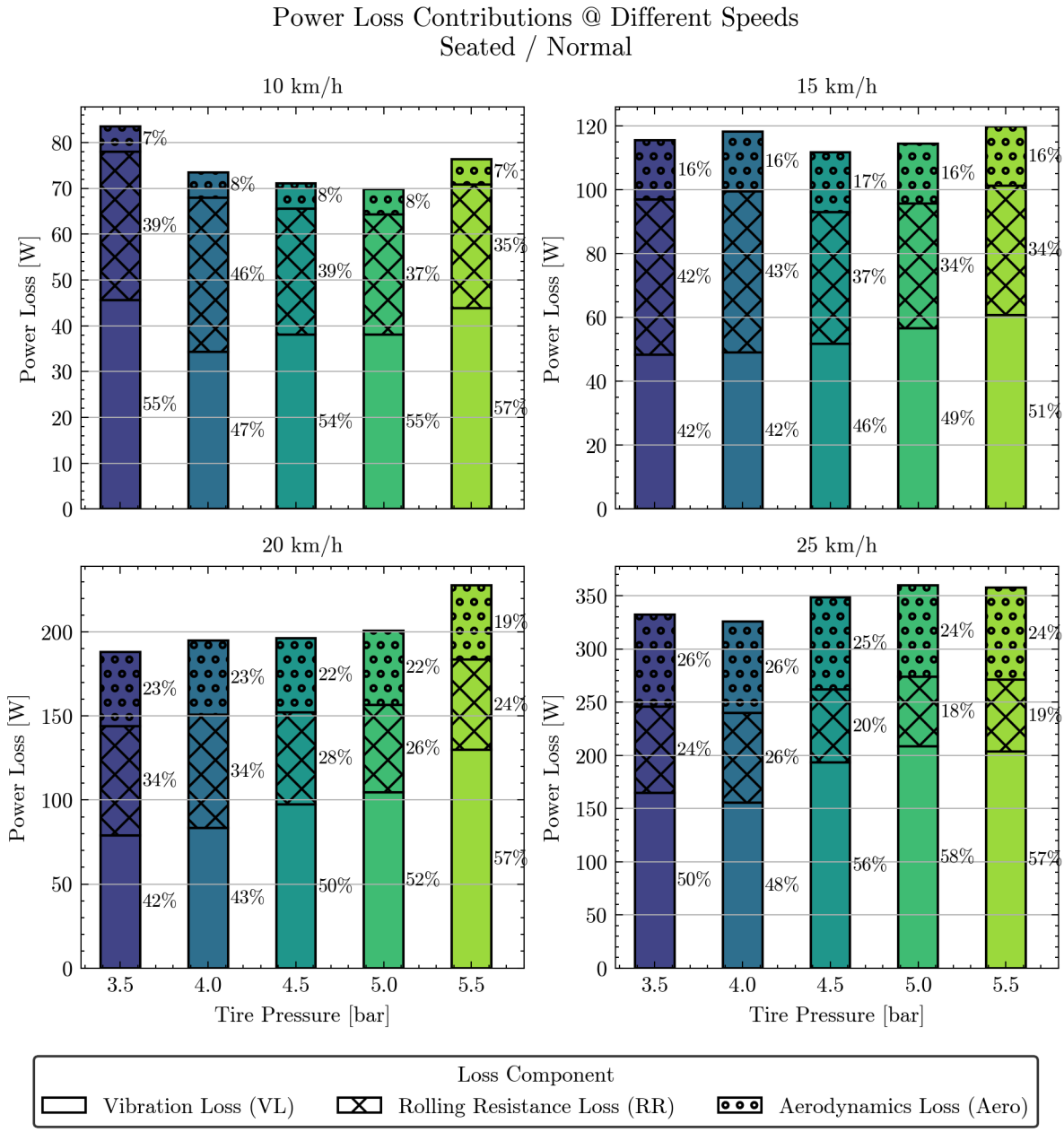

Figure G.6: Power loss components contribution per speed for seated posture and normal behaviour.

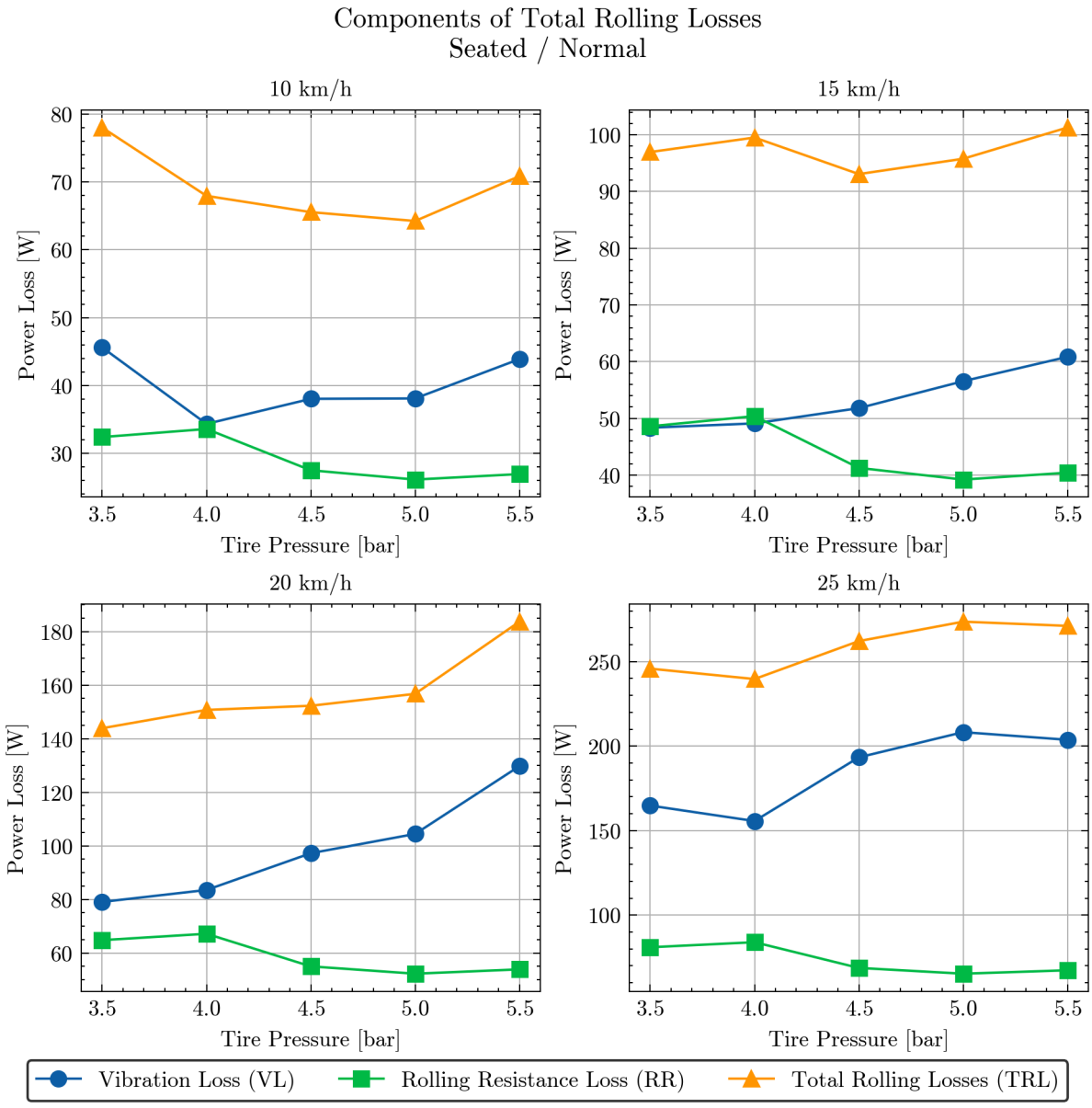

Figure G.7: Components of the Total Rolling Losses under the hypothesis of containing the vibration and rolling resistance losses, shown per speed.

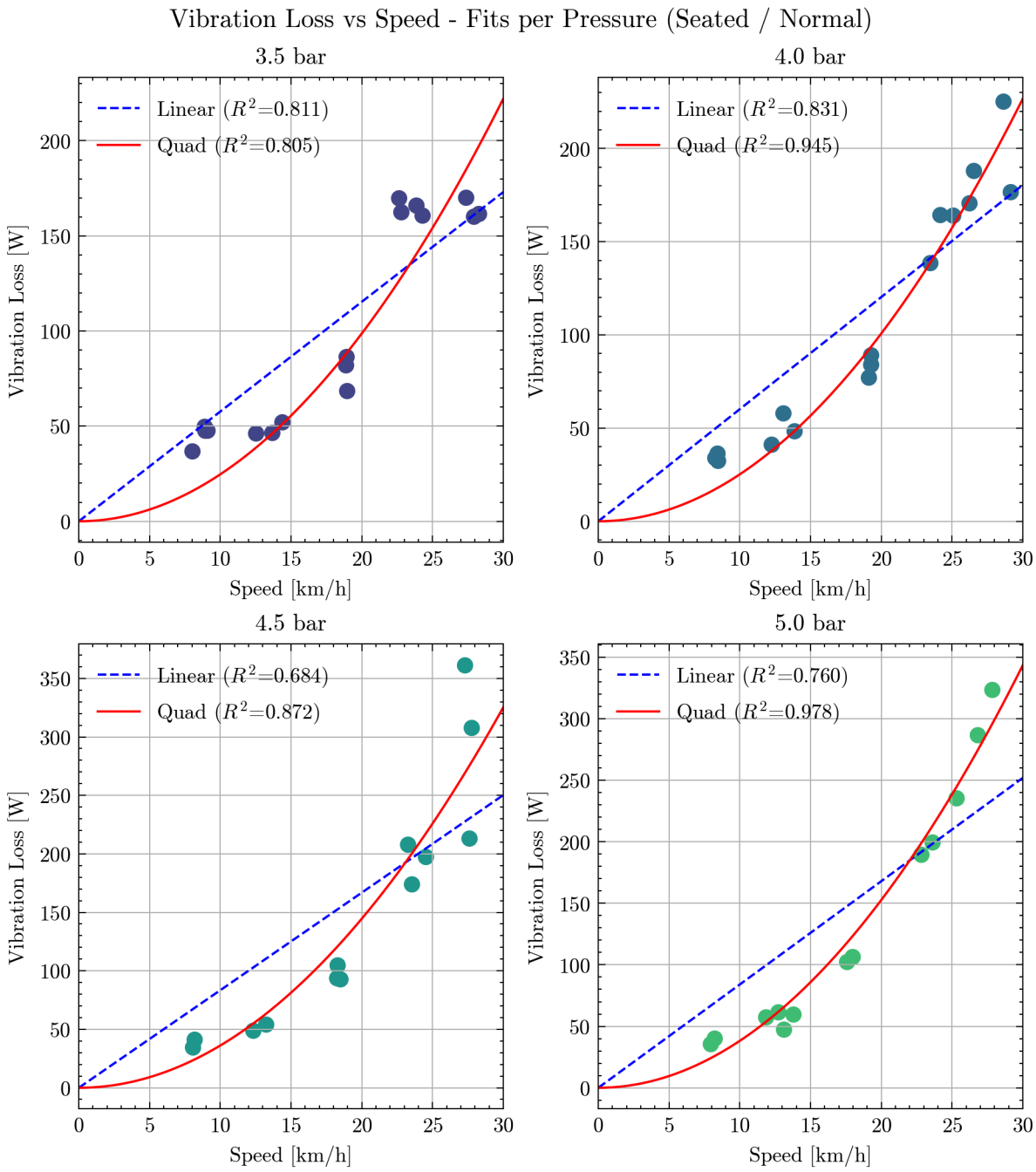

Figure G.8: Vibration loss vs speed curve fitting for every pressure for the seated posture.

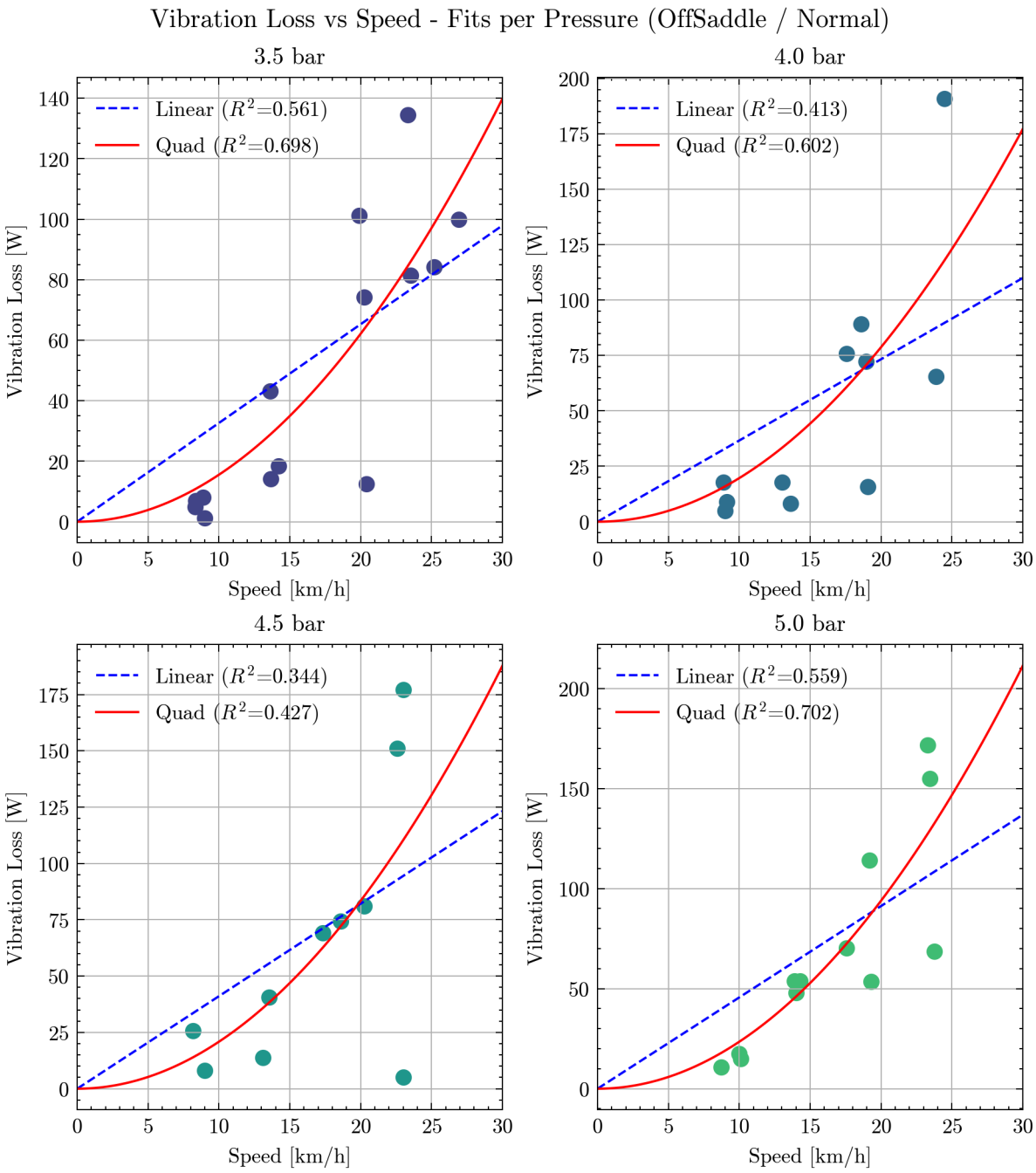

Figure G.9: Vibration loss vs speed curve fitting for every pressure for the off the saddle posture.

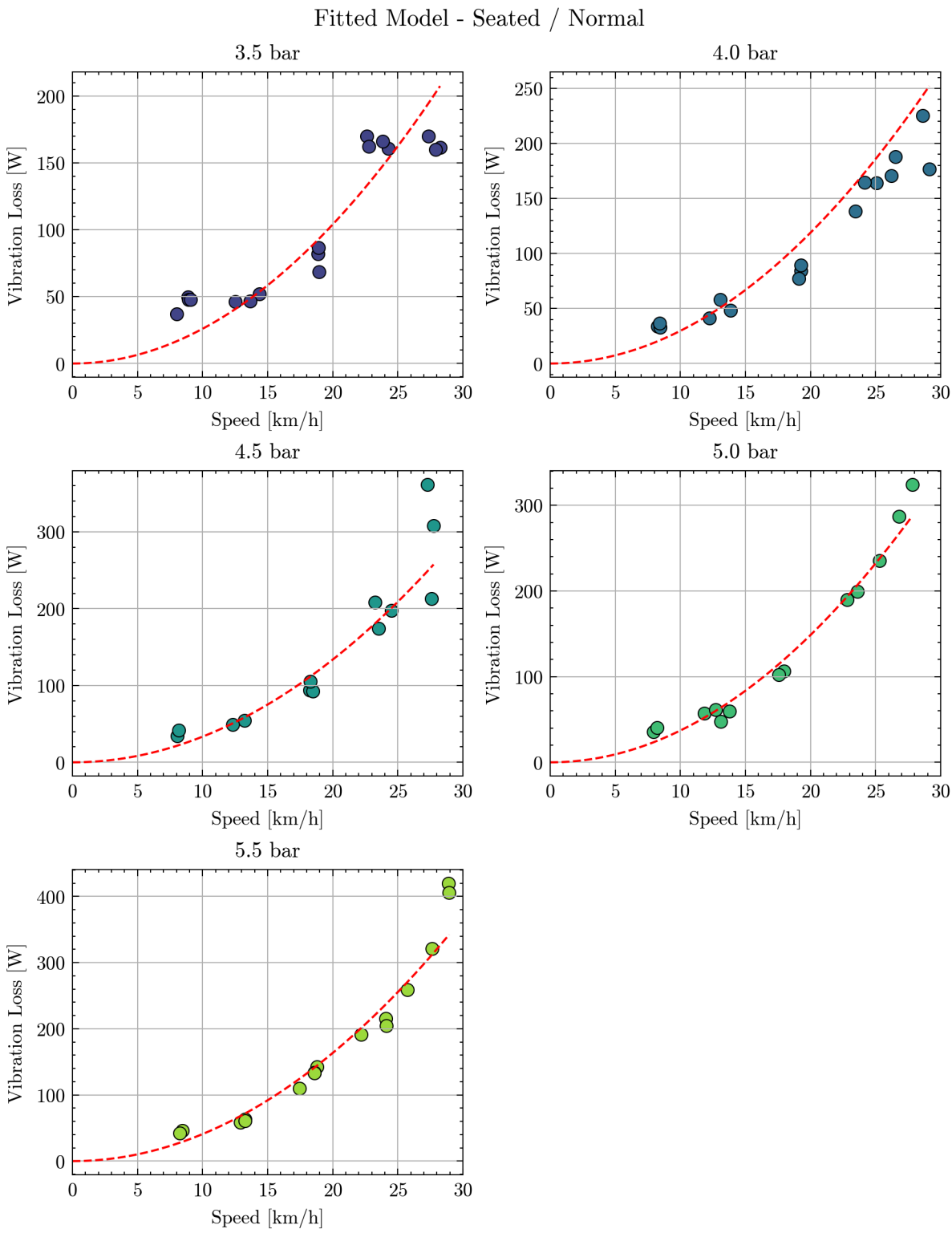

Figure G.10: Fitted model of vibration losses for trials at every pressure tested under normal behaviour and seated posture.

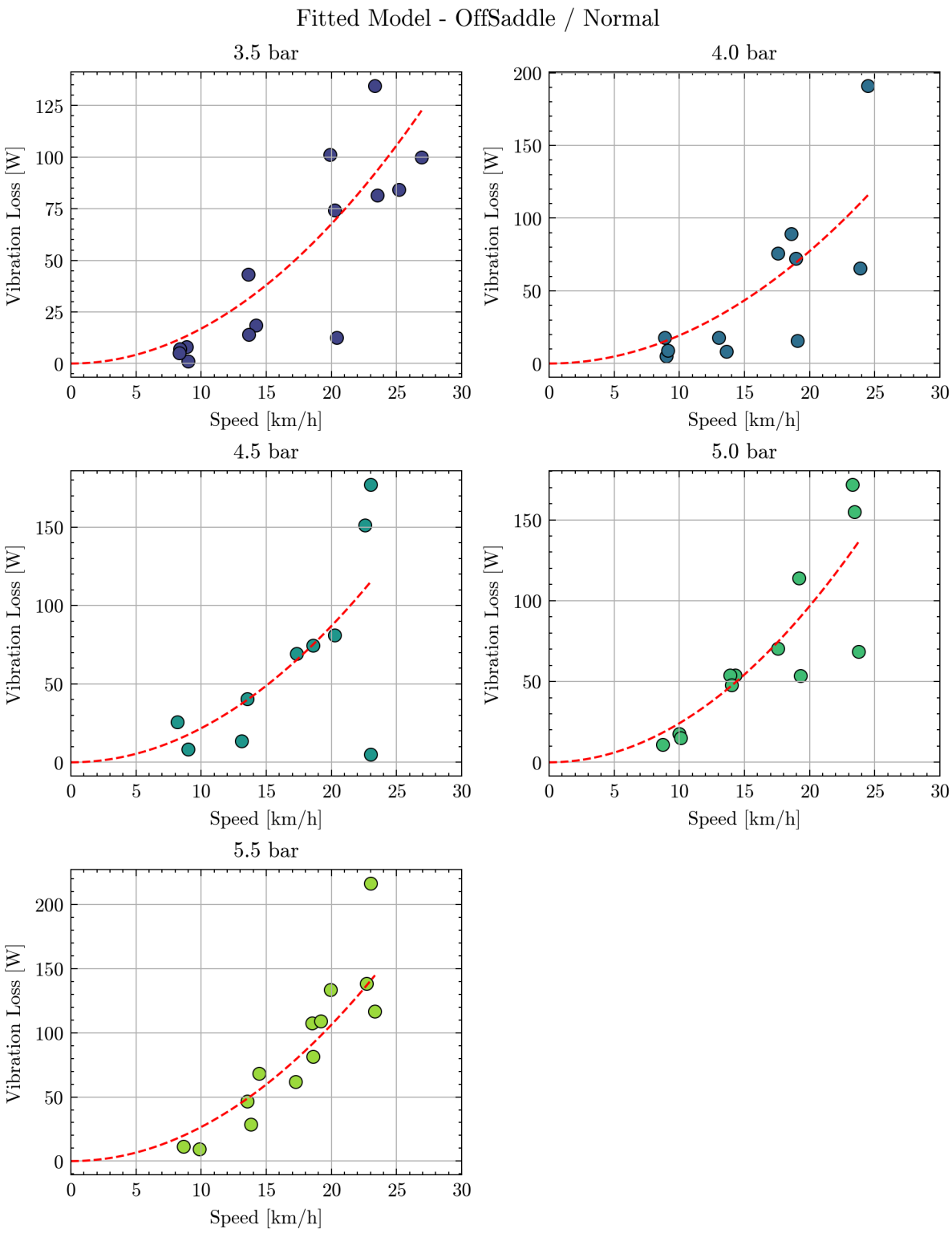

Figure G.11: Fitted model of vibration losses for trials at every pressure tested under normal behaviour and off the saddle posture.